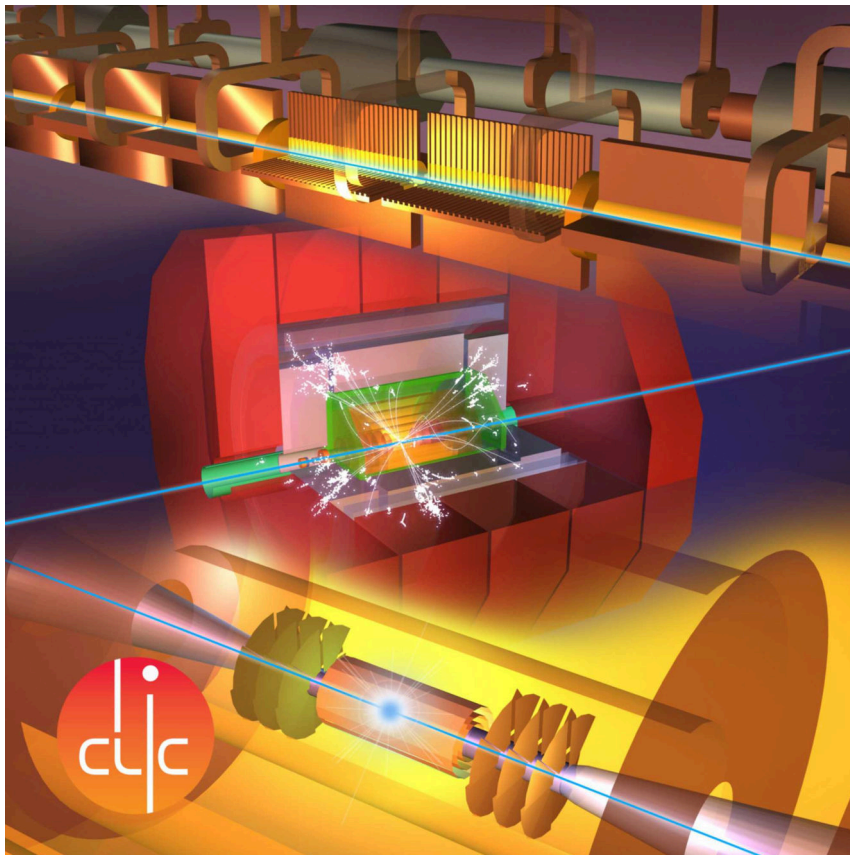


ORGANISATION EUROPÉENNE POUR LA RECHERCHE NUCLÉAIRE
CERN EUROPEAN ORGANIZATION FOR NUCLEAR RESEARCH



THE COMPACT LINEAR COLLIDER (CLIC) 2018 SUMMARY REPORT

GENEVA
2018

CERN Yellow Reports: Monographs
Published by CERN, CH-1211 Geneva 23, Switzerland

ISBN 978-92-9083-506-6 (paperback)

ISBN 978-92-9083-507-3 (PDF)

ISSN 2519-8068 (Print)


ISSN 2519-8076 (Online)

DOI <https://doi.org/10.23731/CYRM-2018-002>

Accepted for publication by the CERN Report Editorial Board (CREB) on 10 December 2018

Available online at <http://publishing.cern.ch/> and <http://cds.cern.ch/>

Copyright © CERN, 2018

 Creative Commons Attribution 4.0

Knowledge transfer is an integral part of CERN's mission.

CERN publishes this volume Open Access under the Creative Commons Attribution 4.0 license (<http://creativecommons.org/licenses/by/4.0/>) in order to permit its wide dissemination and use.

The submission of a contribution to a CERN Yellow Report series shall be deemed to constitute the contributor's agreement to this copyright and license statement. Contributors are requested to obtain any clearances that may be necessary for this purpose.

This volume is indexed in: CERN Document Server (CDS), INSPIRE.

This volume should be cited as:

The Compact Linear Collider (CLIC) – 2018 Summary Report, edited by P.N. Burrows, N. Catalan Lasheras, L. Linssen, M. Petrič, A. Robson, D. Schulte, E. Sicking, S. Stapnes, CERN Yellow Reports: Monographs, Vol. 2/2018, CERN-2018-005-M (CERN, Geneva, 2018).
<https://doi.org/10.23731/CYRM-2018-002>

Abstract

The Compact Linear Collider (CLIC) is a TeV-scale high-luminosity linear e^+e^- collider under development at CERN. Following the CLIC conceptual design published in 2012, this report provides an overview of the CLIC project, its current status, and future developments. It presents the CLIC physics potential and reports on design, technology, and implementation aspects of the accelerator and the detector. For an optimal exploitation of its physics potential, CLIC is foreseen to be built and operated in stages, at centre-of-mass energies of 380 GeV, 1.5 TeV and 3 TeV, respectively, for a site length ranging from 11 km to 50 km. CLIC uses a two-beam acceleration scheme, in which normal-conducting high-gradient 12 GHz accelerating structures are powered via a high-current drive beam. For the first stage, an alternative with X-band klystron powering is also considered. CLIC accelerator optimisation, technical developments and system tests have resulted in significant progress in recent years. Moreover, this has led to an increased energy efficiency (power around 170 MW) for the 380 GeV stage, together with a reduced cost estimate at the level of 6 billion CHF. The detector concept, which matches the physics performance requirements and the CLIC experimental conditions, has been refined using improved software tools for simulation and reconstruction. Significant progress has been made on detector technology developments for the tracking and calorimetry systems. A wide range of CLIC physics studies has been conducted, both through full detector simulations with overlay of beam-induced backgrounds, and through parametric studies, together providing a broad overview of the CLIC physics potential. Each of the three energy stages adds cornerstones of the full CLIC physics programme, such as Higgs width and couplings, top-quark properties, Higgs self-coupling, direct searches, and many precision electroweak measurements. The interpretation of the combined results gives crucial and accurate insight into new physics, largely complementary to LHC and HL-LHC. The construction of the first CLIC energy stage could start by 2026. First beams would be available by 2035, marking the beginning of a broad CLIC physics programme spanning 25–30 years.

Corresponding editors

Philip N. Burrows (University of Oxford), Nuria Catalan Lasheras (CERN),
Lucie Linssen (CERN), Marko Petrič (CERN),
Aidan Robson (University of Glasgow), Daniel Schulte (CERN),
Eva Sicking (CERN), Steinar Stapnes (CERN)

The CLIC and CLICdp collaborations

T.K. Charles, P.J. Giansiracusa, T.G. Lucas, R.P. Rassool, M. Volpi¹
University of Melbourne, Melbourne, Australia

C. Balazs
Monash University, Melbourne, Australia

K. Afanaciev, V. Makarenko
Belarusian State University, Minsk, Belarus

A. Patapenka, I. Zhuk
Joint Institute for Power and Nuclear Research - Sosny, Minsk, Belarus

C. Collette
Université libre de Bruxelles, Brussels, Belgium

M.J. Boland
University of Saskatchewan, Saskatoon, Canada

A.C. Abusleme Hoffman, M.A. Diaz, F. Garay
Pontificia Universidad Católica de Chile, Santiago, Chile

Y. Chi, X. He, G. Pei, S. Pei, G. Shu, X. Wang, J. Zhang, F. Zhao, Z. Zhou
Institute of High Energy Physics, Beijing, China

H. Chen, Y. Gao, W. Huang, Y.P. Kuang, B. Li, Y. Li, X. Meng, J. Shao, J. Shi, C. Tang,
P. Wang, X. Wu, H. Zha
Tsinghua University, Beijing, China

L. Ma, Y. Han
Shandong University, Jinan, China

W. Fang, Q. Gu, D. Huang, X. Huang, J. Tan, Z. Wang, Z. Zhao
Shanghai Institute of Applied Physics, Chinese Academy of Sciences, Shanghai, China

U.I. Uggerhøj, T.N. Wistisen
Aarhus University, Aarhus, Denmark

A. Aabloo, R. Aare, K. Kuppert, S. Vigonski, V. Zadin
University of Tartu, Tartu, Estonia

M. Aicheler, E. Baibuz, E. Brücker, F. Djurabekova², P. Eerola², F. Garcia, E. Haeggström²,
K. Huitu², V. Jansson², I. Kassamakov², J. Kimari², A. Kyritsakis, S. Lehti, A. Meriläinen²,
R. Montonen², K. Nordlund², K. Österberg², A. Saressalo, J. Väinölä, M. Veske
Helsinki Institute of Physics, University of Helsinki, Helsinki, Finland

W. Farabolini, A. Mollard, F. Peauger³, J. Plouin
CEA, Gif-sur-Yvette, France

P. Bambade, I. Chaikovska, R. Chehab, N. Delerue, M. Davier, A. Faus-Golfe, A. Irlles,
W. Kaabi, F. LeDiberder, R. Pöschl, D. Zerwas
*Laboratoire de l'Accélérateur Linéaire, Université de Paris-Sud XI, IN2P3/CNRS, Orsay,
France*

B. Aimard, G. Balik, J.-J. Blaising, L. Brunetti, M. Chefdeville, A. Dominjon, C. Drancourt,
N. Geoffroy, J. Jacquemier, A. Jeremie, Y. Karyotakis, J.M. Nappa, M. Serluca, S. Vilalte,
G. Vouters

LAPP, Université de Savoie, IN2P3/CNRS, Annecy, France

A. Bernhard, E. Bründermann, S. Casalbuoni, S. Hillenbrand, J. Gethmann, A. Grau,
E. Huttel, A.-S. Müller, P. Peiffer⁴, I. Perić, D. Saez de Jauregui
Karlsruhe Institute of Technology (KIT), Karlsruhe, Germany

L. Emberger, C. Graf, F. Simon, M. Szalay, N. van der Kolk⁵
Max-Planck-Institut für Physik, Munich, Germany

S. Brass, W. Kilian

Department of Physics, University of Siegen, Siegen, Germany

T. Alexopoulos, T. Apostolopoulos⁶, E.N. Gazis, N. Gazis, V. Kostopoulos⁷, S. Kourkoulis
National Technical University of Athens, Athens, Greece

B. Heilig

*Department of Basic Geophysical Research, Mining and Geological Survey of Hungary,
Tihany, Hungary*

J. Lichtenberger

Space Research Laboratory, Eötvös Loránd University, Budapest, Hungary

P. Shrivastava

Raja Ramanna Centre for Advanced Technology, Department of Atomic Energy, Indore, India

M.K. Dayyani, H. Ghasem¹, S.S. Hajari, H. Shaker¹

*The School of Particles and Accelerators, Institute for Research in Fundamental Sciences,
Tehran, Iran*

Y. Ashkenazy, I. Popov, E. Engelberg, A. Yashar

Racah Institute of Physics, Hebrew University of Jerusalem, Jerusalem, Israel

H. Abramowicz, Y. Benhammou, O. Borysov, M. Borysova, A. Levy, I. Levy
*Raymond & Beverly Sackler School of Physics & Astronomy, Tel Aviv University, Tel Aviv,
Israel*

D. Alesini, M. Bellaveglia, B. Buonomo, A. Cardelli, M. Diomedea, M. Ferrario, A. Gallo,
A. Ghigo, A. Giribono, L. Piersanti, A. Stella, C. Vaccarezza
INFN e Laboratori Nazionali di Frascati, Frascati, Italy

J. de Blas

Università di Padova and INFN, Padova, Italy

R. Franceschini

Università degli Studi Roma Tre and INFN, Roma, Italy

G. D'Auria, S. Di Mitri

Elettra Sincrotrone Trieste, Trieste, Italy

T. Abe, A. Aryshev, M. Fukuda, K. Furukawa, H. Hayano, Y. Higashi, T. Higo, K. Kubo,
S. Kuroda, S. Matsumoto, S. Michizono, T. Naito, T. Okugi, T. Shidara, T. Tauchi,
N. Terunuma, J. Urakawa, A. Yamamoto¹

High Energy Accelerator Research Organization, KEK, Tsukuba, Japan

R. Raboanary

University of Antananarivo, Antananarivo, Madagascar

O.J. Luiten, X.F.D. Stragier

Eindhoven University of Technology, Eindhoven, Netherlands

R. Hart, H. van der Graaf

Nikhef, Amsterdam, Netherlands

G. Eigen

Department of Physics and Technology, University of Bergen, Bergen, Norway

E. Adli¹, C.A. Lindstrøm, R. Lillestøl, L. Malina¹, J. Pflingstner, K.N. Sjobak¹

University of Oslo, Oslo, Norway

A. Ahmad, H. Hoorani, W.A. Khan

National Centre for Physics, Islamabad, Pakistan

S. Bugiel, R. Bugiel, M. Firlej, T.A. Fiutowski, M. Idzik, J. Moroń, K.P. Świątek

AGH University of Science and Technology, Krakow, Poland

P. Brückman de Renstrom, B. Krupa, M. Kucharczyk, T. Lesiak, B. Pawlik, P. Sopicki,

B. Turbiarz, T. Wojtoń, L.K. Zawiejski

Institute of Nuclear Physics, Polish Academy of Sciences, Krakow, Poland

J. Kalinowski, K. Nowak, A.F. Żarnecki

Faculty of Physics, University of Warsaw, Warsaw, Poland

E. Fîru, V. Ghenescu, A.T. Neagu, T. Preda, I.S. Zgura

Institute of Space Science, Bucharest, Romania

A. Aloev, N. Azaryan, I. Boyko, J. Budagov, M. Chizhov, M. Filippova, V. Glagolev,

A. Gongadze, S. Grigoryan, D. Gudkov, V. Karjavine, M. Lyablin, Yu. Nefedov, A. Olyunin¹,

A. Rymbekova, A. Samochkine, A. Sapronov, G. Shelkov, G. Shirkov, V. Soldatov,

E. Solodko¹, G. Trubnikov, I. Tyapkin, V. Uzhinsky, A. Vorozhtov, A. Zhemchugov

Joint Institute for Nuclear Research, Dubna, Russia

E. Levichev, N. Mezentsev, P. Piminov, D. Shatilov, P. Vobly, K. Zolotarev

Budker Institute of Nuclear Physics, Novosibirsk, Russia

I. Božović Jelisavčić, G. Kačarević, G. Milutinović Dumbelović, M. Pandurović,

M. Radulović, J. Stevanović, N. Vukasinović

Vinča Institute of Nuclear Sciences, University of Belgrade, Belgrade, Serbia

D.-H. Lee

School of Space Research, Kyung Hee University, Yongin, Gyeonggi, South Korea

N. Ayala, G. Benedetti, T. Guenzel, U. Iriso, Z. Marti, F. Perez, M. Pont
CELLS-ALBA, Barcelona, Spain

J. Trenado
University of Barcelona, Barcelona, Spain

A. Ruiz-Jimeno, I. Vila
IFCA, CSIC-Universidad de Cantabria, Santander, Spain

J. Calero, M. Dominguez, L. Garcia-Tabares, D. Gavela, D. Lopez, F. Toral
Centro de Investigaciones Energéticas, Medioambientales y Tecnológicas (CIEMAT), Madrid, Spain

C. Blanch Gutierrez, M. Boronat, D. Esperante¹, E. Fullana, J. Fuster, I. García, B. Gimeno, P. Gomis Lopez, D. González, M. Perelló, E. Ros, M.A. Villarejo, A. Vnuchenko, M. Vos
Instituto de Física Corpuscular (CSIC-UV), Valencia, Spain

Ch. Borgmann, R. Brenner, T. Ekelöf, M. Jacewicz, M. Olvegård, R. Ruber, V. Ziemann
Uppsala University, Uppsala, Sweden

D. Aguglia, J. Alabau Gonzalvo, M. Alcaide Leon, N. Alipour Tehrani, M. Anastasopoulos, A. Andersson, F. Andrianala⁸, F. Antoniou, A. Apyan, D. Arominski⁹, K. Artoos, S. Assly, S. Atieh, C. Baccigalupi, R. Ballabriga Sune, D. Banon Caballero, M.J. Barnes, J. Barranco Garcia, A. Bartalesi, J. Bauche, C. Bayar, C. Belver-Aguilar, A. Benot Morell¹⁰, M. Bernardini, D.R. Bett, S. Bettoni¹¹, M. Bettencourt, B. Bielawski, O. Blanco Garcia, N. Blaskovic Kraljevic, B. Bolzon¹², X.A. Bonnin, D. Bozzini, E. Branger, E. Brondolin, O. Brunner, M. Buckland¹³, H. Bursali, H. Burkhardt, D. Caiazza, S. Calatroni, M. Campbell, N. Catalan Lasheras*, B. Cassany, E. Castro, R.H. Cavaleiro Soares, M. Cerqueira Bastos, A. Cherif, E. Chevally, V. Cilento¹⁴, R. Corsini, R. Costa¹⁵, B. Cure, S. Curt, A. Dal Gobbo, D. Dannheim, E. Daskalaki, L. Deacon, A. Degiovanni, G. De Michele, L. De Oliveira, V. Del Pozo Romano, J.P. Delahaye, D. Delikaris, P.G. Dias de Almeida¹⁶, T. Dobers, S. Doebert, I. Doytchinov, M. Draper, F. Duarte Ramos, M. Duquenne, N. Egidios Plaja, K. Elsener, J. Esberg, M. Esposito, L. Evans, V. Fedosseev, P. Ferracin, A. Fiergolski, K. Foraz, A. Fowler, F. Friebel, J-F. Fuchs, A. Gaddi, D. Gamba, L. Garcia Fajardo¹⁷, H. Garcia Morales, C. Garion, M. Gasior, L. Gatignon, J-C. Gayde, A. Gerbershagen, H. Gerwig, G. Giambelli, A. Gilardi, A.N. Goldblatt, S. Gonzalez Anton, C. Grefe¹⁸, A. Grudiev, H. Guerin, F.G. Guillot-Vignot, M.L. Gutt-Mostowy, M. Hein Lutz, C. Hessler, J.K. Holma, E.B. Holzer, M. Hourican, D. Hynds¹⁹, E. Ikarios, Y. Inttjore Levinsen, S. Janssens, A. Jeff, E. Jensen, M. Jonker, S.W. Kamugasa, M. Kastriotou, J.M.K. Kemppinen, V. Khan, R.B. Kieffer, W. Klempt, N. Kokkinis, I. Kossyvakis, Z. Kostka, A. Korsback, E. Koukovini Platia, J.W. Kovermann, C-I. Kozsar, I. Kremastiotis²⁰, J. Kröger²¹, S. Kulis, A. Latina, F. Leaux, P. Lebrun, T. Lefevre, E. Leogrande, L. Linssen*, X. Liu, X. Llopart Cudie, S. Magnoni, C. Maidana, A.A. Maier, H. Mainaud Durand, S. Mallows, E. Manosperti, C. Marelli, E. Marin Lacoma, S. Marsh, R. Martin, I. Martini, M. Martyanov, S. Mazzoni, G. Mcmonagle, L.M. Mether, C. Meynier, M. Modena, A. Moilanen, R. Mondello, P.B. Moniz Cabral, N. Mouriz Irazabal, M. Munker, T. Muranaka, J. Nadenau, J.G. Navarro, J.L. Navarro Quirante, E. Nebo Del Busto, N. Nikiforou²², P. Ninin, M. Nonis, D. Nisbet, F.X. Nuiry, A. Nürnberg²³, J. Ögren, J. Osborne, A.C. Ouniche, R. Pan²⁴, S. Papadopoulou, Y. Papaphilippou, G. Paraskaki, A. Pastushenko¹⁰, A. Passarelli, M. Patecki,

L. Pazdera, D. Pellegrini, K. Pepitone, E. Perez Codina, A. Perez Fontenla, T.H.B. Persson, M. Petrić^{25*}, S. Pitman, F. Pitters²⁶, S. Pittet, F. Plassard, D. Popescu, T. Quast²⁷, R. Rajamak, S. Redford¹¹, L. Remandet, Y. Renier²⁴, S.F. Rey, O. Rey Orozco, G. Riddone, E. Rodriguez Castro, P. Roloff, C. Rossi, F. Rossi, V. Rude, I. Ruehl, G. Rumolo, A. Sailer, J. Sandomierski, E. Santin, C. Sanz, J. Sauza Bedolla, U. Schnoor, H. Schmickler, D. Schulte*, E. Senes, C. Serpico, G. Severino, N. Shipman, E. Sicking*, R. Simoniello²⁸, P.K. Skowronski, P. Sobrino Mompean, L. Soby, P. Sollander, A. Solodko, M.P. Sosin, S. Spannagel, S. Sroka, S. Stapnes*, G. Sterbini, G. Stern, R. Ström, M.J. Stuart, I. Syratchev, K. Szypula, F. Tecker, P.A. Thonet, P. Thrane, L. Timeo, M. Tiirakari, R. Tomas Garcia, C.I. Tomoiaga, P. Valerio²⁹, T. Vaňát, A.L. Vamvakas, J. Van Hoorne, O. Viazlo, M. Vicente Barreto Pinto³⁰, N. Vitoratou, V. Vlachakis, M.A. Weber, R. Wegner, M. Wendt, M. Widorski, O.E. Williams, M. Williams³¹, B. Woolley, W. Wuensch, A. Wulzer, J. Uythoven, A. Xydou, R. Yang, A. Zelios, Y. Zhao³², P. Zisopoulos
CERN, Geneva, Switzerland

M. Benoit, D M S Sultan
Département de Physique Nucléaire et Corpusculaire (DPNC), Université de Genève, Genève, Switzerland

F. Riva¹
Département de Physique Théorique, Université de Genève, Genève, Switzerland

M. Bopp, H.H. Braun, P. Craievich, M. Dehler, T. Garvey, M. Pedrozzi, J.Y. Raguin, L. Rivkin³³, R. Zennaro
Paul Scherrer Institut, Villigen, Switzerland

S. Guillaume, M. Rothacher
ETH Zurich, Institute of Geodesy and Photogrammetry, Zurich, Switzerland

A. Aksoy, Z. Nergiz³⁴, Ö. Yavas
Ankara University, Ankara, Turkey

H. Denizli, U. Keskin, K. Y. Oyulmaz, A. Senol
Department of Physics, Abant İzzet Baysal University, Bolu, Turkey

A.K. Ciftci
Izmir University of Economics, Izmir, Turkey

V. Baturin, O. Karpenko, R. Kholodov, O. Lebed, S. Lebedynskiy, S. Mordyk, I. Musienko, Ia. Profatilova, V. Storizhko
Institute of Applied Physics, National Academy of Sciences of Ukraine, Sumy, Ukraine

R.R. Bosley, T. Price, M.F. Watson, N.K. Watson, A.G. Winter
University of Birmingham, Birmingham, United Kingdom

J. Goldstein
University of Bristol, Bristol, United Kingdom

S. Green, J.S. Marshall³⁵, M.A. Thomson, B. Xu, T. You³⁶
Cavendish Laboratory, University of Cambridge, Cambridge, United Kingdom

W.A. Gillespie
University of Dundee, Dundee, United Kingdom

M. Spannowsky
Department of Physics, Durham University, Durham, United Kingdom

C. Beggan
British Geological Survey, Edinburgh, United Kingdom

V. Martin, Y. Zhang
University of Edinburgh, Edinburgh, United Kingdom

D. Protopopescu, A. Robson^{1*}
University of Glasgow, Glasgow, United Kingdom

R.J. Apsimon³⁷, I. Bailey³⁸, G.C. Burt³⁷, A.C. Dexter³⁷, A.V. Edwards³⁷, V. Hill³⁸,
S. Jamison, W.L. Millar³⁷, K. Papke³⁷
Lancaster University, Lancaster, United Kingdom

G. Casse, J. Vossebeld
University of Liverpool, Liverpool, United Kingdom

T. Aumeyr, M. Bergamaschi¹, L. Bobb³⁸, A. Bosco, S. Boogert, G. Boorman, F. Cullinan,
S. Gibson, P. Karataev, K. Kruchinin, K. Lekomtsev, A. Lyapin, L. Nevay, W. Shields,
J. Snuverink, J. Towler, E. Yamakawa
*The John Adams Institute for Accelerator Science, Royal Holloway, University of London,
Egham, United Kingdom*

V. Boisvert, S. West
Royal Holloway, University of London, Egham, United Kingdom

R. Jones, N. Joshi
University of Manchester, Manchester, United Kingdom

D. Bett, R.M. Bodenstein¹, T. Bromwich, P.N. Burrows^{1*}, G.B. Christian³⁸, C. Gohil¹,
P. Korysko¹, J. Paszkiewicz¹, C. Perry, R. Ramjiawan, J. Roberts
John Adams Institute, Department of Physics, University of Oxford, Oxford, United Kingdom

T. Coates, F. Salvatore
University of Sussex, Brighton, United Kingdom

A. Bainbridge³⁷, J.A. Clarke³⁷, N. Krumpa B.J.A. Shepherd³⁷, D. Walsh³
STFC Daresbury Laboratory, Warrington, United Kingdom

S. Chekanov, M. Demarteau, W. Gai, W. Liu, J. Metcalfe, J. Power, J. Repond, H. Weerts,
L. Xia, J. Zhang
Argonne National Laboratory, Argonne, USA

J. Zupan
Department of Physics, University of Cincinnati, Cincinnati, OH, USA

J.D. Wells, Z. Zhang
Physics Department, University of Michigan, Ann Arbor, MI, USA

C. Adolphsen, T. Barklow, V. Dolgashev, M. Franzi, N. Graf, J. Hewett, M. Kemp,
O. Kononenko, T. Markiewicz, K. Moffeit, J. Neilson, Y. Nosochkov, M. Oriunno, N. Phinney,
T. Rizzo, S. Tantawi, J. Wang, B. Weatherford, G. White, M. Woodley
SLAC National Accelerator Laboratory, Menlo Park, USA

¹Also at CERN, Geneva, Switzerland

²Also at Department of Physics, University of Helsinki, Helsinki, Finland

³Now at CERN, Geneva, Switzerland

⁴Now at Johannes-Gutenberg University, Mainz, Germany

⁵Now at Nikhef / Utrecht University, Amsterdam / Utrecht, The Netherlands

⁶Also at Department of Informatics, Athens University of Business and Economics, Athens, Greece

⁷Also at University of Patras, Patras, Greece

⁸Also at University of Antananarivo, Antananarivo, Madagascar

⁹Also at Warsaw University of Technology, Warsaw, Poland

¹⁰Also at IFIC, Valencia, Spain

¹¹Now at Paul Scherrer Institute, Villigen, Switzerland

¹²Now at CEA, Gif-sur-Yvette, France

¹³Also at University of Liverpool, United Kingdom

¹⁴Also at LAL, Orsay, France

¹⁵Also at Uppsala University, Uppsala, Sweden

¹⁶Also at IFCA, CSIC-Universidad de Cantabria, Santander, Spain

¹⁷Now at LBNL, Berkeley CA, USA

¹⁸Now at University of Bonn, Bonn, Germany

¹⁹Now at Nikhef, Amsterdam, The Netherlands

²⁰Also at KIT, Karlsruhe, Germany

²¹Also at Ruprecht-Karls-Universität Heidelberg, Germany

²²Now at University of Texas, Austin, USA

²³Now at Karlsruhe Institute of Technology, Karlsruhe, Germany

²⁴Now at DESY, Zeuthen, Germany

²⁵Also at J. Stefan Institute, Ljubljana, Slovenia

²⁶Also at Vienna University of Technology, Vienna, Austria

²⁷Also at RWTH Aachen University, Aachen, Germany

²⁸Now at Johannes Gutenberg Universität, Mainz, Germany

²⁹Now at Département de Physique Nucléaire et Corpusculaire (DPNC), Université de Genève, Geneva, Switzerland

³⁰Also at Département de Physique Nucléaire et Corpusculaire (DPNC), Université de Genève, Geneva, Switzerland

³¹Also at University of Glasgow, Glasgow, United Kingdom

³²Also at Shandong University, Jinan, China

³³Also at EPFL, Lausanne, Switzerland

³⁴Also at Omer Halis Demir University, Nigde, Turkey

³⁵Now at University of Warwick, Coventry, United Kingdom

³⁶Also at DAMTP, University of Cambridge, Cambridge, United Kingdom

³⁷Also at The Cockcroft Institute, Daresbury, United Kingdom

³⁸Now at Diamond Light Source, Harwell, United Kingdom
*Editors (CLIC-Summary-Report-2018@cern.ch)

Contents

1	Introduction	1
2	CLIC physics overview	3
2.1	CLIC physics exploration at three energy stages	3
2.2	Higgs physics potential	4
2.3	Top-quark physics potential	8
2.4	Direct and indirect searches for BSM physics	11
2.5	Overall CLIC physics reach	17
3	CLIC accelerator design, technologies and performance	21
3.1	Introduction	21
3.2	CLIC design and performance at 380 GeV	21
3.2.1	Design overview	21
3.2.2	Main-beam design considerations and choices	23
3.2.3	Performance of the drive-beam concept	23
3.2.4	Luminosity performance	24
3.2.5	Operation and availability	25
3.2.6	Energy flexibility	26
3.2.7	Beam experiments	27
3.3	A klystron-based CLIC at 380 GeV	28
3.3.1	Design choice	28
3.3.2	Design implications	28
3.4	Extension to higher energy stages	29
3.4.1	Baseline design upgrade	30
3.4.2	Upgrade from the klystron-based option	32
3.5	Accelerator technologies	32
3.5.1	Main linac accelerating structures	33
3.5.2	RF power generation and distribution	34
3.5.3	Alignment and stabilisation	36
3.5.4	Beam instrumentation	38
3.5.5	Vacuum system	39
3.5.6	Magnets	39
3.5.7	Klystron-based main linac RF unit and module design	42
4	CLIC detector design, technologies and performance	43
4.1	Experimental conditions at CLIC	43
4.2	Physics-driven detector requirements	45
4.3	CLIC detector concept	46
4.4	Detector technologies	47
4.4.1	Vertex and tracking technologies	48
4.4.2	Electromagnetic and hadronic calorimeters	51
4.4.3	Very forward calorimeters	52
4.5	Detector performance	53

5	CLIC project implementation	61
5.1	The CLIC stages and construction	61
5.1.1	Civil engineering and infrastructure	61
5.1.2	Annual and integrated luminosities	64
5.2	Construction and operation schedules	64
5.2.1	380 GeV drive-beam schedule	65
5.2.2	380 GeV klystron-driven schedule	66
5.2.3	Schedules for the stages at higher energies and the complete project	66
5.2.4	Concluding remarks on the schedule	67
5.3	Cost estimate	67
5.3.1	Scope and method	67
5.3.2	Value estimates and cost drivers	68
5.3.3	Labour estimates	70
5.3.4	Value estimate and cost drivers of the CLIC detector	70
5.3.5	Operation costs	71
5.4	Power and energy consumption	72
5.4.1	Energy consumption	73
5.4.2	Power reduction studies and future prospects	73
6	Future opportunities	75
6.1	Physics motivation	75
6.2	Opportunities for extension based on future technologies	77
6.2.1	General concept	77
6.2.2	Dielectric accelerating structures	77
6.2.3	Plasma-based acceleration	78
6.2.4	Luminosity enabling technologies	79
7	CLIC objectives for the period 2020–2025	81
7.1	Accelerator complex	81
7.1.1	Accelerator programme overview	82
7.1.2	Programme implementation, technology demonstrators and collaboration	82
7.2	Detector and physics	83
8	Summary	85

1 Introduction

The Compact Linear Collider (CLIC) is a multi-TeV high-luminosity linear e^+e^- collider under development by the CLIC accelerator collaboration [1]. CLIC uses a novel two-beam acceleration technique, with normal-conducting accelerating structures operating in the range of 70–100 MV/m. Detailed studies of the CLIC physics potential, design of a detector for CLIC, and R&D on detector technologies are performed by the CLIC detector and physics (CLICdp) collaboration [1]. The CLIC Conceptual Design Report (CDR) was published in 2012 [2–4]. The main focus of the CDR was to demonstrate the feasibility of the CLIC accelerator at high energy (3 TeV) and to confirm that high-precision physics measurements can be performed, despite the luminosity spectrum and the presence of particles from beam-induced background.

Following the completion of the CDR, detailed studies on Higgs and top-quark physics, with particular focus on the first energy stage of CLIC, concluded that the optimal centre-of-mass energy for the first stage is 380 GeV. As a result, a comprehensive optimisation study of the CLIC accelerator complex was performed, by scanning the full parameter space for the accelerating structures, and by using the CLIC performance, cost and energy consumption as a gauge for operation at 380 GeV and 3 TeV. The results led to optimised accelerator design parameters for the proposed CLIC staging scenario, with operation at 380 GeV, 1.5 TeV and 3 TeV, as reported in [5].

This report summarises progress and results of the CLIC studies at the time of submitting input to the update of the European Strategy for Particle Physics, in December 2018. The report describes recent achievements in accelerator design, technology development, system tests and beam tests. Large-scale CLIC-specific beam tests have taken place, for example, at the CLIC Test Facility CTF3 at CERN [6], at the Accelerator Test Facility ATF2 at KEK [7, 8], at the FACET facility at SLAC [9] and at the FERMI facility in Trieste [10]. Crucial experience also emanates from the expanding field of Free Electron Laser (FEL) linacs and recent-generation light sources. Together they provide the demonstration that all implications of the CLIC design parameters are well understood and reproduced in beam tests. Therefore the CLIC performance goals are realistic. An alternative CLIC scenario for the first stage, where the accelerating structures are powered by X-band klystrons, is also under study. The implementation of CLIC near CERN has been investigated. Principally focusing on the 380 GeV stage, this includes civil engineering aspects, electrical networks, cooling and ventilation, installation scheduling, transport, and safety aspects. All CLIC studies have put emphasis on optimising cost and energy efficiency, and the resulting power and cost estimates are reported.

Since the completion of the CDR, the CLIC detector was further optimised through a broad range of simulation studies, resulting in the CLICdet detector design [11, 12]. In order to enlarge the angular acceptance of the detector, the final focusing quadrupoles are now placed outside the detector in the accelerator tunnel. The software suite for simulation and event reconstruction was modernised and tuned for use with CLICdet. Detector technology developments have focused on the most challenging aspects of the experiment, namely the light-weight silicon vertex and tracker system and the highly-granular calorimeters. The detector R&D activities have resulted in technology demonstrators, showing that the required performance is already achievable or will be achieved in the next phase, compatible with the CLIC timescale [13].

The physics potential at the three CLIC energy stages has been explored in much detail. The first stage of CLIC provides collisions at $\sqrt{s} = 380$ GeV. This gives access to Higgs boson measurements through Higgsstrahlung and WW-fusion [14], thereby providing accurate model-independent measurements of the Higgs couplings and the Higgs width. Precision top-quark physics [15] is also addressed at this energy, and a fraction of the running time will be devoted to a threshold scan of top-quark pair production around 350 GeV.

The second stage, with collisions foreseen at 1.5 TeV, opens the energy frontier, allowing for the

discovery of new physics phenomena [4, 16]. The double Higgsstrahlung process $e^+e^- \rightarrow ZHH$ can be observed and additional Higgs and top-quark properties are within reach, such as the Higgs self-coupling and rare Higgs branching ratios. The third stage at 3 TeV further enlarges the CLIC physics potential, e.g. allowing discovery of new electroweak particles or dark matter candidates, which may be more easily observed at CLIC than at the HL-LHC. The 3 TeV stage also provides the best sensitivity to new physics processes at much higher energy scales, via indirect searches.

Section 2 of this report gives an overview of physics measurements at CLIC, demonstrating how they improve our knowledge of the Standard Model and how CLIC results have an impact on understanding the nature and scale of new physics Beyond the Standard Model (BSM). Section 3 provides an overview of the CLIC accelerator design and performance at 380 GeV for both the two-beam baseline design and the klystron-based option. This section also describes the path to the higher energies, 1.5 TeV and 3 TeV, and gives an overview of the key CLIC technology developments. Referring to beam experiments and hardware tests, Section 3 also describes key achievements providing evidence that the CLIC performance goals can be met.

In Section 4 the CLIC detector and its performance results through simulation and event reconstruction are described. The progress made and the status of the detector technology developments are summarised. Section 5 describes the present plans for the implementation of CLIC, with emphasis on the 380 GeV stage. It reports on civil engineering and schedule aspects, and provides estimates of the energy consumption and of the cost for construction and operation. Physics motivation and options to expand the energy reach of CLIC using future technologies are discussed in Section 6. The CLIC objectives for the period 2020–2025 are outlined in Section 7. Section 8 provides a short summary of this report.

2 CLIC physics overview

2.1 CLIC physics exploration at three energy stages

CLIC’s physics programme will substantially improve our knowledge and probe the open questions arising from the LHC and other particle physics facilities, and from related astronomical observations. As CLIC gives access to a very wide range of energies, it can reach unprecedented precision in the properties and interactions of the Higgs boson, top quark, and electroweak gauge bosons. It has the potential to make discoveries of new states that are inaccessible at other facilities, including the possible discovery of dark matter, and could potentially give some experimental insight to cosmological questions such as the stability or instability of the vacuum and the origin of the baryon asymmetry. The science program ranges from the ‘guaranteed physics’ of precision studies of the Standard Model (SM), which through effective field theory interpretations give access beyond the capacity of other facilities to new physics at high scales, to ‘prospect physics’ of directly producing new states or observing new interactions.

Detector and experimental environment A single optimised CLIC detector, CLICdet [11], has been refined from the two CLIC detector concepts CLIC_SiD and CLIC_ILD that were adapted from the International Linear Collider (ILC) concepts as described in the CLIC CDR [3]. All three detector designs are compatible with the experimental conditions at CLIC and satisfy the performance requirements driven by the physics objectives, which are described in Sections 4.1 and 4.3. Common software tools for CLIC_SiD and CLIC_ILD perform full simulation [17, 18], digitisation and reconstruction [19, 20], particle flow reconstruction [21–24], and vertexing and heavy flavour tagging [25]. The corresponding, and partially overlapping, software tools for CLICdet are described in Section 4.5. Full simulations of the CLIC_ILD and CLIC_SiD detector concepts have been used for the physics projections in the areas of Higgs and top-quark physics reported in this section. Physics background processes, as well as the CLIC experimental conditions and luminosity spectrum have systematically been taken into account. The dark matter search using the mono-photon signature (see Section 2.4) is the first full simulation study using CLICdet. Recent phenomenological studies to explore the BSM potential of CLIC often use parameterised detector performance derived from full simulations, for example through the fast simulation package Delphes [26, 27].

Staging and polarisation The total integrated luminosities for each energy stage are summarised in Table 1. Each stage takes seven or eight years and stages are separated by around two years, resulting in a total programme of 25–30 years.

Table 1: Baseline CLIC energy stages and integrated luminosities for each stage in the updated scenario [28].

Stage	\sqrt{s} [TeV]	\mathcal{L}_{int} [ab^{-1}]
1	0.38 (and 0.35)	1.0
2	1.5	2.5
3	3.0	5.0

The staged approach allows optimal exploitation of the CLIC physics capabilities. For the initial stage, a centre-of-mass energy of $\sqrt{s} = 380 \text{ GeV}$ gives access to SM Higgs physics and top-quark physics, and provides direct and indirect sensitivity to BSM effects. A top-quark pair-production threshold scan around 350 GeV is also foreseen. The second stage at 1.5 TeV opens more Higgs production channels including $t\bar{t}H$, double-Higgs production, and rare decays, and allows further direct sensitivity to many BSM models. The ultimate stage at 3 TeV gives the best sensitivity to many new physics scenarios and

to the Higgs self-coupling. The energies of the second and third stages are benchmarks, and can be optimised in light of new physics information. For many of the studies reported here, an earlier energy staging baseline of $\sqrt{s} = 350\text{ GeV}$, 1.4 TeV , and 3 TeV was assumed; it was as a consequence of these and other studies that the present initial stage energy of $\sqrt{s} = 380\text{ GeV}$ was adopted in order to optimise the physics reach of CLIC.

The CLIC baseline specifies $\pm 80\%$ electron polarisation, and no positron polarisation. At the initial energy stage, equal amounts of -80% and $+80\%$ polarisation running are foreseen. For the two higher-energy stages, a compromise is required between the strong enhancement in single and double-Higgs production through WW-fusion that comes by running with -80% electron polarisation, and the full reach to BSM effects, which requires some running with $+80\%$ electron polarisation. The baseline is to share the running time for -80% and $+80\%$ electron polarisation in the ratio 80:20.

The following sections discuss the Higgs physics, top-quark physics, and BSM physics reach of CLIC across the three energy stages.

2.2 Higgs physics potential

A detailed understanding of the Higgs sector is one of the highest priorities in particle physics. While the discovery of a Higgs boson confirms the electroweak symmetry breaking mechanism, the nature of the particle is still to be determined: whether it is the fundamental scalar of the SM, or a more complex object, or part of an extended Higgs sector. The Higgs interactions could provide access to BSM physics that couples to the SM only through the Higgs boson.

Around 160 000 Higgs bosons will be produced at the initial CLIC energy stage, and millions will be produced at $\sqrt{s} = 3\text{ TeV}$. All collider events will be read out, without online event filters, and high acceptance and event selection efficiencies will result in very large datasets available for analysis. The large datasets and the large energy range will allow a comprehensive Higgs programme with unique reach. The staging of the collider is crucial to the Higgs physics programme, with some measurements accessible only at the initial energy, while other measurements are enabled or improved by the high-energy running.

Different BSM scenarios result in different patterns of modifications to the Higgs couplings from their SM values; for new physics at the TeV scale this is typically at the percent level and so measurement of the couplings with similar or better precision is necessary. The CLIC Higgs reach has been comprehensively investigated using full simulation studies [14]. Some updated studies and the sensitivities resulting from the updated luminosity staging scenario are summarised in this section. BSM Higgs scenarios are further explored in [Section 2.4](#).

Higgs production Cross sections for the main Higgs production processes are shown in [Figure 1](#). At the initial CLIC energy stage the dominant Higgs production mechanism is the Higgsstrahlung process, $e^+e^- \rightarrow ZH$. These events can be selected based only on the decay products of the Z boson, enabling measurements of the total production cross section and hence the Higgs branching ratios and width. This allows a model-independent determination of the Higgs couplings, without any assumptions about BSM invisible decays of the Higgs boson; a feature that is unique to lepton colliders. Higgs production at the initial energy stage also has a significant contribution from the WW-fusion process, $e^+e^- \rightarrow H\nu_e\bar{\nu}_e$, and the combined study of the Higgsstrahlung and WW-fusion processes improves the precision of the Higgs couplings and width measurements. Around $\sqrt{s} = 1.5\text{ TeV}$ and at $\sqrt{s} = 3\text{ TeV}$ Higgs production is dominated by WW-fusion; at these energies also the ZZ-fusion process, $e^+e^- \rightarrow H e^+e^-$, becomes significant, and $t\bar{t}H$ and direct double-Higgs production become accessible.

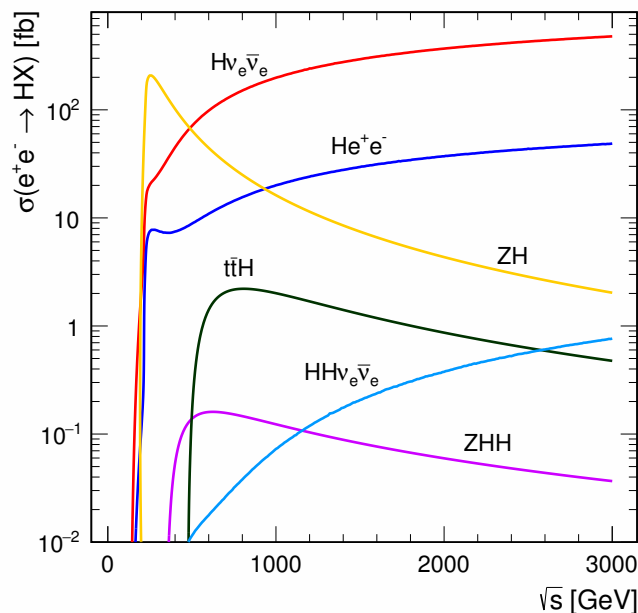


Figure 1: Production cross section as a function of centre-of-mass energy for the main Higgs production processes at an e^+e^- collider. The values shown correspond to unpolarised beams with initial-state radiation and do not include the effect of beamstrahlung. (image credit: CLICdp)

Invisible Higgs decays The recoil mass distribution from $e^+e^- \rightarrow ZH$ events can be used to search for BSM decay modes of the Higgs boson into ‘invisible’ final states [29]. For 1 ab^{-1} at $\sqrt{s} = 350 \text{ GeV}$ the upper limit on the invisible Higgs branching ratio, obtained from Higgsstrahlung events with hadronic Z boson decays, is $\text{BR}(H \rightarrow \text{invis.}) < 0.69\%$ at 90% C.L.

Higgs couplings Measurements of Higgs production cross sections times branching fractions to many final states can be combined to extract the Higgs couplings and widths. Precisions extracted from a model-independent global fit, described in [14], are given in Figure 2 and Table 2. The fit assumes the current baseline scenario of operation with -80% ($+80\%$) electron beam polarisation for 80% (20%) of the collected luminosity at the second and third energy stages. Each energy stage contributes significantly to the Higgs programme; the initial stage provides σ_{HZ} and couplings to most fermions and bosons, while the higher-energy stages improve them and add the top-quark and muon couplings. The initial stage is required, to allow the model-independent coupling fits to be performed at all energy stages. Precisions extracted from a model-dependent global fit, also described in [14], where it is assumed that there are no non-Standard-Model Higgs decays, are given in Figure 3 and Table 3. This fit also assumes the current beam polarisation scenario. Already after the initial energy stage, in many cases the CLIC precision is significantly better than for the HL-LHC [30], and improves further with the higher-energy running.

Parameter	Relative precision		
	350 GeV 1 ab ⁻¹	+ 1.4 TeV + 2.5 ab ⁻¹	+ 3 TeV + 5 ab ⁻¹
g_{HZZ}	0.6%	0.6%	0.6%
g_{HWW}	1.0%	0.6%	0.6%
g_{Hbb}	2.1%	0.7%	0.7%
g_{Hcc}	4.4%	1.9%	1.4%
$g_{\text{H}\tau\tau}$	3.1%	1.4%	1.0%
$g_{\text{H}\mu\mu}$	—	12.1%	5.7%
g_{Htt}	—	3.0%	3.0%
g_{Hgg}^\dagger	2.6%	1.4%	1.0%
$g_{\text{H}\gamma\gamma}^\dagger$	—	4.8%	2.3%
$g_{\text{HZ}\gamma}^\dagger$	—	13.3%	6.7%
Γ_{H}	4.7%	2.6%	2.5%

Table 2

CLIC results of the model-independent fit to the Higgs couplings. For g_{Htt} , the 3 TeV case has not yet been studied. The three effective couplings g_{Hgg}^\dagger , $g_{\text{H}\gamma\gamma}^\dagger$ and $g_{\text{HZ}\gamma}^\dagger$ are also included in the fit. Operation with -80% ($+80\%$) electron beam polarisation is assumed for 80% (20%) of the collected luminosity above 1 TeV, corresponding to the baseline scenario. (image credit: CLICdp)

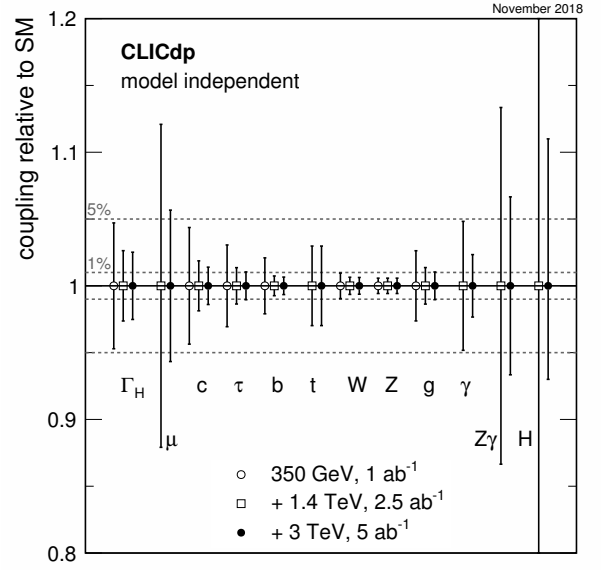


Figure 2

Parameter	Relative precision		
	350 GeV 1 ab ⁻¹	+ 1.4 TeV + 2.5 ab ⁻¹	+ 3 TeV + 5 ab ⁻¹
κ_{HZZ}	0.4%	0.3%	0.2%
κ_{HWW}	0.8%	0.2%	0.1%
κ_{Hbb}	1.3%	0.3%	0.2%
κ_{Hcc}	4.1%	1.8%	1.3%
$\kappa_{\text{H}\tau\tau}$	2.7%	1.2%	0.9%
$\kappa_{\text{H}\mu\mu}$	—	12.1%	5.6%
κ_{Htt}	—	2.9%	2.9%
κ_{Hgg}	2.1%	1.2%	0.9%
$\kappa_{\text{H}\gamma\gamma}$	—	4.8%	2.3%
$\kappa_{\text{HZ}\gamma}$	—	13.3%	6.6%

Table 3

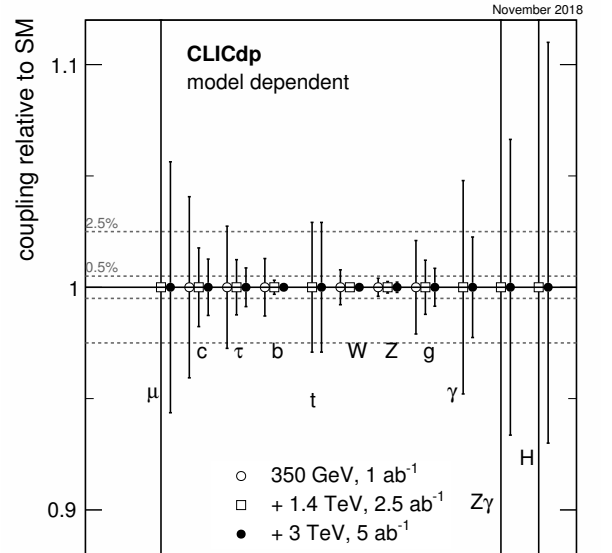


Figure 3

CLIC results of the model-dependent fit to the Higgs coupling, without theoretical uncertainties. For κ_{Htt} , the 3 TeV case has not yet been studied. Operation with -80% ($+80\%$) electron beam polarisation is assumed for 80% (20%) of the collected luminosity above 1 TeV, corresponding to the baseline scenario. (image credit: CLICdp)

Higgs self-coupling Centre-of-mass energies of 1.4 TeV or 1.5 TeV and 3 TeV give access to double-Higgs production processes, which are sensitive to the trilinear Higgs coupling λ at tree level. The second energy stage allows a 5σ -observation of the double Higgsstrahlung process $e^+e^- \rightarrow ZHH$ and provides evidence for the W boson fusion process $e^+e^- \rightarrow HH\nu_e\bar{\nu}_e$ with a significance of 3.6σ assuming the SM value of λ . At $\sqrt{s} = 3$ TeV the vector-boson fusion process $e^+e^- \rightarrow HH\nu_e\bar{\nu}_e$ is the leading double-Higgs production process and its cross section can be measured with a precision $\Delta\sigma/\sigma = 7.4\%$ at $\sqrt{s} = 3$ TeV. The cross section dependence on λ is not monotonic, so that using only the cross section information to extract λ , or equivalently the variation $\Delta\kappa_\lambda$ from the Standard Model value $\kappa_\lambda = 1$, leads to an ambiguity as shown in the Figure 4(a). This can be resolved by adding the differential information including the invariant mass $M(HH)$ in $e^+e^- \rightarrow HH\nu_e\bar{\nu}_e$ at $\sqrt{s} = 3$ TeV, and the cross section measurement of the double Higgsstrahlung process ZHH at $\sqrt{s} = 1.4$ TeV. This removes the ambiguity and increases the sensitivity as shown in Figure 4(b). The $e^+e^- \rightarrow HH\nu_e\bar{\nu}_e$ process also contains the quartic vertex HHWW.

The final sensitivity that can be reached on the trilinear self-coupling λ is $[-7\%, +11\%]$ [31].

The analysis can also be used to set two-dimensional constraints on λ and κ_{HHWW} .

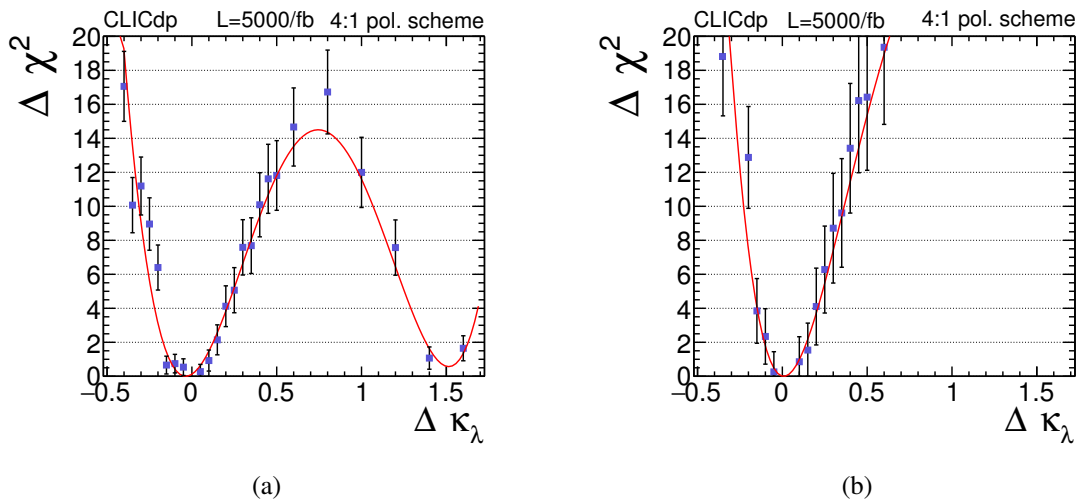


Figure 4: Nominal $\Delta\chi^2$ distributions from template fitting with different values of the Higgs self-coupling λ , shown for the variation $\Delta\kappa_\lambda$ from the SM value of $\kappa_\lambda = 1$ and using (a) only cross section information for the $HH\nu_e\bar{\nu}_e$ process at 3 TeV; (b) additionally using the differential distribution $M(HH)$ in $HH\nu_e\bar{\nu}_e$ at 3 TeV and the cross section measurement of ZHH at 1.4 TeV. In this case the ambiguity is removed and the sensitivity is increased. (image credit: CLICdp)

Composite Higgs Constraints from the CLIC Higgs measurements, along with measurements of Drell-Yan production ($e^+e^- \rightarrow f\bar{f}$) and WW production, can be interpreted in concrete classes of BSM scenarios; for example, scenarios where the known particles are in fact composite bound states. Composite Higgs frameworks could address the electroweak naturalness problem. In these frameworks the Higgs boson is a pseudo-Nambu-Goldstone boson of an underlying strongly-interacting composite sector. The 5σ discovery reach in the plane of the mass scale m_* and coupling strength parameter g_* that characterise the Higgs composite sector is shown in Figure 5 [16]. CLIC will discover Higgs compositeness if the compositeness scale is below 8 TeV. Scales up to 40 TeV can be discovered, in particularly favourable conditions, for large composite sector couplings $g_* \simeq 8$. For comparison, the model-independent projected HL-LHC exclusion reach is only around 3 TeV, and for $g_* \simeq 8$ the maximum HL-LHC reach is around 7 TeV [16].

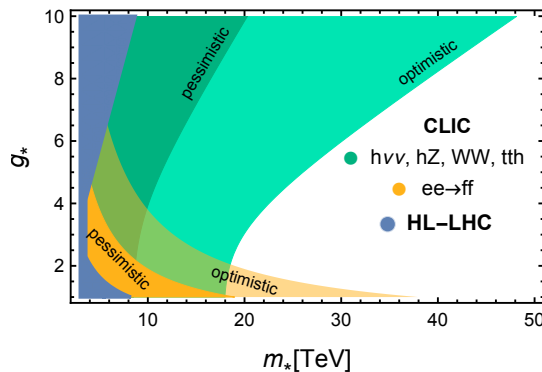


Figure 5: Higgs compositeness: ‘Optimistic’ (light colour) and ‘pessimistic’ (dark colour) 5σ discovery regions for Higgs compositeness derived from a combined fit to Higgs and WW production (green) and Drell-Yan processes (orange); and the HL-LHC 95% C.L. exclusion reach. From [16].

2.3 Top-quark physics potential

The top quark is the heaviest known fundamental particle and occupies an important role in many BSM theories; it therefore provides unique opportunities to test the SM and probe signatures of BSM effects. So far, top quarks have been produced only in hadron collisions, whereas studying their properties in electron-positron collisions will provide a new set of complementary and improved-precision measurements. Cross sections for the main top-quark pair production processes are shown in Figure 6. Each stage of CLIC provides sensitivity to different aspects of top-quark production and properties: at the initial stage this includes top-quark mass measurements and cross section and asymmetry measurements, while higher-energy stages additionally allow studies including direct access to the top Yukawa coupling and CP properties in the $t\bar{t}H$ coupling. The 3 TeV stage is most favourable for study of top-quark pair production via vector boson fusion. A broad set of measurements has been investigated for CLIC [15]; they are summarised in the following sections.

Top-quark mass Several complementary methods allow precise determinations of the top-quark mass at CLIC: a threshold scan; measurements of the cross section for radiative events; and direct reconstruction. Direct reconstruction of the top-quark decay products yields a statistical precision of around 30 MeV; a systematic accuracy that matches the statistical accuracy would require control of the jet energy scale at the level of 0.02%, and the theoretical interpretation of the measurement introduces a large systematic uncertainty. Fitting templates to cross sections as a function of centre-of-mass energy has the advantage that the extracted mass is well defined theoretically, which significantly reduces the overall uncertainty. This can be done for radiative events above threshold, as a function of the effective $t\bar{t}$ centre-of-mass energy $\sqrt{s'}$ after radiation of an energetic initial state photon from the incoming electron or positron beam, $e^+e^- \rightarrow t\bar{t}\gamma$. This method leads to a total uncertainty on the top-quark mass of around 140 MeV with an integrated luminosity of 1 ab^{-1} . However, the most precise top-quark mass determination comes from an energy scan around the top-quark pair-production threshold. The study assumes a scan collecting 10 fb^{-1} at each of ten points in \sqrt{s} , separated by 1 GeV. A highly pure sample of top-quark events can be selected and used to measure the cross section at each point. The top-quark mass is extracted using a template fit to the measured cross sections as a function of \sqrt{s} as shown in Figure 7. The flexibility of the CLIC accelerator design is illustrated by potential optimisation of the luminosity spectrum for the threshold scan as described in Section 3.2.6, and shown by the two bunch charge options in Figure 7. The cross section and the position and shape of the turn-on curve are strongly dependent on the precise value of the top-quark mass and width, Yukawa coupling, and strong coupling α_s . The

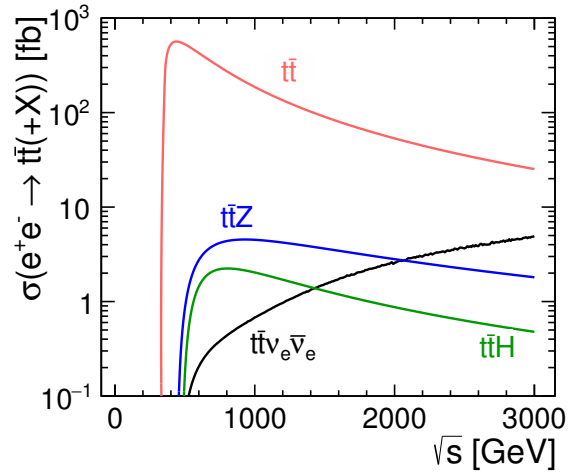


Figure 6: Production cross section as a function of centre-of-mass energy for the main top-quark pair production processes at an e^+e^- collider. Leading-order values for unpolarised beams with initial-state radiation are shown, not including the effect of beamstrahlung. (image credit: CLICdp)

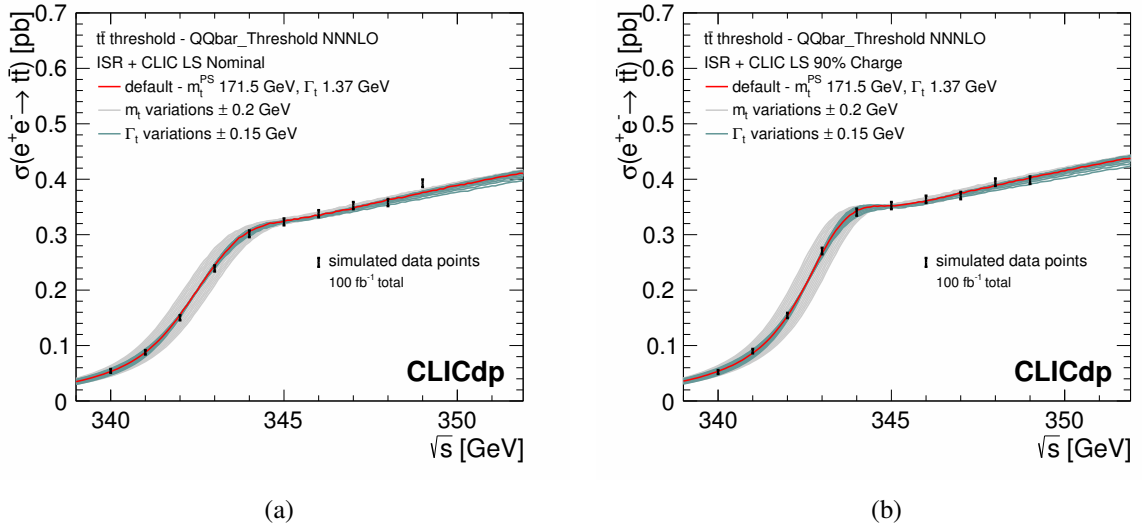


Figure 7: Illustration of a top-quark threshold scan at CLIC with a total integrated luminosity of 100 fb^{-1} , for two scenarios for the luminosity spectrum (LS): (a) nominal, and (b) ‘reduced charge’. The bands around the central cross section curve show the dependence of the cross section on the top-quark mass and width, illustrating the sensitivity of the threshold scan. The error bars on the simulated data points show the statistical uncertainties of the cross section measurement, taking into account signal efficiencies and background levels. From [15].

template line shapes can be computed at NNNLO QCD, taking into account NLO Higgs and electroweak effects. The statistical uncertainty is 20 MeV for the reduced bunch charge option and 22 MeV for the nominal luminosity spectrum. The small theoretical uncertainty of around 10 MeV associated with converting the measured quantity to the $\overline{\text{MS}}$ (modified minimal subtraction) mass scheme means that a total uncertainty of around 50 MeV is thus feasible.

Top-quark pair-production properties Top-quark pair production at all three energy stages contributes to the determination of electroweak couplings.

At the initial stage, semi-leptonic events, where the W boson from one top-quark decay decays hadronically and the other leptonically, are reconstructed by clustering into four jets, identifying a reconstructed lepton and jets that originate from b-quarks, and performing a kinematic fit. The efficient b-tagging of two jets allows suppression of most of the backgrounds. Measurements of the cross section can be made with a statistical accuracy below 1% for each electron beam polarisation, and the measured top-quark angular distribution in semi-leptonic events gives the forward-backward asymmetry with a statistical uncertainty of around 3–4%.

At the higher energy stages the top quarks are produced with significant boosts. Jet substructure techniques [32] have been successfully applied to reconstructing boosted semi-leptonic events and measuring the forward-backward asymmetry. The total cross section and forward-backward asymmetries are extracted with precisions of $\Delta\sigma/\sigma = 1.1\%$ (2.3%) and $\Delta A_{FB}/A_{FB} = 1.5\%$ (2.0%) at 1.4 TeV (3 TeV) for an electron beam polarisation of -80% . All of these measurements, along with a set of ten statistically optimised observables defined for each centre-of-mass energy and electron beam polarisation on the $e^+e^- \rightarrow t\bar{t} \rightarrow bW^+\bar{b}W^-$ differential distribution [33–36], are used in global fits to constrain possible BSM effects induced by heavy new physics, as described in Section 2.4.

Top-quark Yukawa coupling and CP properties Associated $t\bar{t}H$ production is accessible at the second CLIC stage. Studies of $H \rightarrow b\bar{b}$ with fully-hadronic and semi-leptonic $t\bar{t}$ decays give an expected precision on the cross section at 1.4 TeV with 2.5 ab^{-1} of 5.7%. The cross section is sensitive to the strength of the Yukawa coupling and its measurement can be translated into a determination of the Yukawa coupling with a precision of 2.9%. As an extra probe of the CP structure of the Standard Model, to search for sources of CP violation that could give insight into the matter-antimatter asymmetry in the universe, the CP structure of the $t\bar{t}H$ coupling can be investigated. A CP-odd admixture to the coupling can be parameterised with a mixing angle ϕ as $-ig_{t\bar{t}H}(\cos\phi + i\sin\phi\gamma_5)$; this alters the cross section, which can therefore be used to set limits on the admixture. Further sensitivity can be obtained from differential distributions, for example the up-down asymmetry of the anti-top quark with respect to the plane defined by the incoming electron and the top quark [37]. The sensitivity is $\Delta\sin^2\phi < 0.07$ (0.04) for the range $0 < \sin^2\phi < 1$ ($0.3 < \sin^2\phi < 1$).

Compositeness interpretation Constraints from the global fit of optimised observables from $t\bar{t}$ production and from $t\bar{t}H$ production can also be interpreted in compositeness scenarios. Top-quark compositeness emerges naturally in the composite Higgs frameworks discussed at the end of section Section 2.2. The $t\bar{t}$ and $t\bar{t}H$ sensitivities have been interpreted for the discovery reach of top-quark compositeness scenarios at $\sqrt{s} = 3 \text{ TeV}$. The 5σ discovery reach in the plane of the mass scale m_* and coupling strength parameter g_* that characterise the composite sector is shown in Figure 8 [15, 16, 38], for optimistic and pessimistic values of coefficients of the top-philic operators. In this framework the top-quark compositeness is characterised by couplings y_L and y_R that control the strength of the mixing of the q_L doublet and the t_R singlet with the composite sector. The two benchmark scenarios considered are partial compositeness, where $y_L = y_R = \sqrt{y_L g_*}$; and total t_R compositeness, where $y_L = y_t$ and $y_R = g_*$. The strong sensitivity of the observables to effects that grow with centre-of-mass energy results in a discovery reach for top compositeness beyond 7 TeV, and more than 20 TeV in favourable conditions, at CLIC. These values are higher than could be *excluded* at HL-LHC.

Vector-boson fusion production of top-quark pairs The high-energy stages of CLIC allow the production of top-quark pairs through vector boson fusion, which could reveal large BSM effects. An important role is played by longitudinally-polarised vector bosons, which at high energy are equivalent

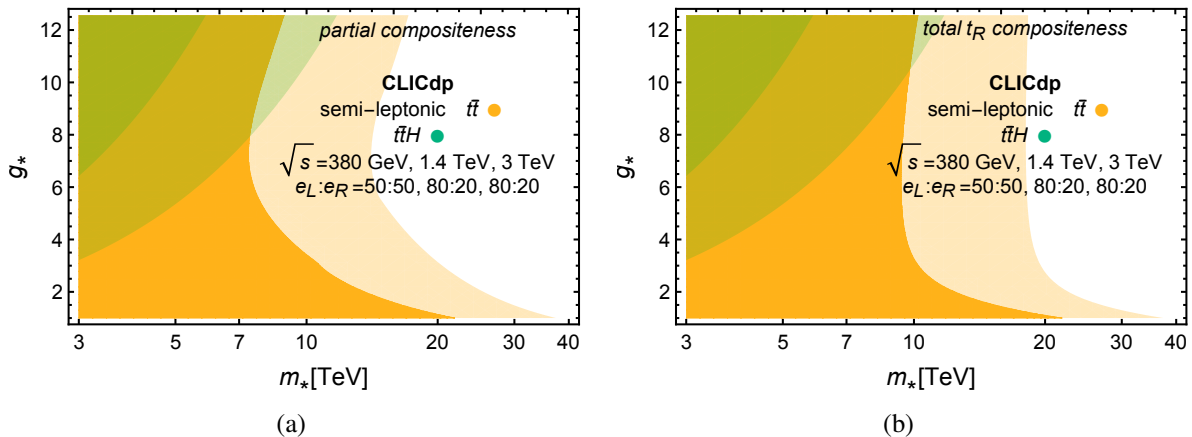


Figure 8: Top compositeness: ‘Optimistic’ (light colour) and ‘pessimistic’ (dark colour) 5σ discovery regions for (a) the partial compositeness, and (b) the total t_R compositeness scenarios. The orange contours are derived from the $t\bar{t}$ global fit, while the green contours are derived from the top Yukawa analysis. From [15].

to the Higgs field. In several new physics scenarios that address the naturalness problem, Higgs boson and top-quark interactions receive large modifications, and a process like $W^+W^- \rightarrow t\bar{t}$ is directly sensitive to this, for example through the modification of the $t\bar{t}$ scattering angle in the centre-of-mass frame. The process $W^+W^- \rightarrow t\bar{t}$ and its backgrounds have been studied at parton level at $\sqrt{s} = 3$ TeV. In e^+e^- collisions at CLIC, the backgrounds to this process (including $t\bar{t}$ production) can be suppressed to a negligible level. The vector-boson fusion process has been used to constrain possible BSM effects as described in Section 2.4, and in particular the high $M(t\bar{t})$ region is sensitive to BSM effects that grow with energy.

2.4 Direct and indirect searches for BSM physics

The exploration of physics beyond the Standard Model is well motivated by problems that the Standard Model cannot address, such as the origin of the weak scale, the nature of dark matter, and the origin of the asymmetry between baryons and anti-baryons in the universe. Typically, at e^+e^- colliders new particles can be observed almost up to the kinematic limit, e.g. $m \lesssim \sqrt{s}/2$, and the flexibility to adjust beam energies and polarisations at a linear collider potentially allows accurate determination of their quantum numbers. Earlier CLIC studies emphasised the capabilities for characterising BSM particles expected to be discovered at the LHC or CLIC, and unveiling the underlying BSM theory [3, 4, 39]. While this is still important, recent work has focused on the prospects for discoveries at CLIC, in the event of no new physics being observed at the LHC. The goal is to go beyond attempting to quantify the performance in terms of a few benchmark models or scenarios, and to explore the landscape of fundamental physics as broadly as possible, showing the reach for broad classes of theories. With this in mind, many new physics models and scenarios have been investigated and are gathered together in a dedicated report [16].

Potential new physics can be probed directly by searching for new states, and indirectly through interpretation of precision measurements. The latter approach can be investigated through the Standard Model Effective Field Theory (SM-EFT), which allows the systematic parameterisation of BSM effects and their modification of SM processes. Direct searches are explored in the context of general scenarios: for example, extended Higgs sectors, which can be connected with models of electroweak baryogenesis; and general dark matter models, such as Higgsinos and minimal dark matter. CLIC can discover the Higgsino for a mass of 1 TeV, which is the mass that it would need to have to be responsible for the observed relic dark matter density. CLIC can also be conclusive on other relevant and less standard dark

matter scenarios. In the remainder of this section, these and other highlights from the recent studies are discussed further in order to illustrate the range and reach of CLIC.

Global EW EFT analysis CLIC precision measurements can be sensitive to different BSM contributions that arise from heavy BSM dynamics, associated with a mass scale beyond CLIC’s direct energy reach. CLIC sensitivities to Higgs couplings, top-quark observables, WW production, and two-fermion scattering processes $e^+e^- \rightarrow f\bar{f}$ where $f = c, b, e, \mu$, have all been put together in a global fit using the SM-EFT. The purpose of the global fit is to probe many classes of BSM theory at once, in a model-independent fashion. The SM-EFT extends the dimension-four SM Lagrangian to include interaction operators of higher dimension $d > 4$. Here, BSM particles are implicit and must be light enough and strongly-enough coupled to the SM to generate large enough operators to give visible effects, while being heavy enough not to be produced directly. The leading effects can be captured by dimension-6 operators:

$$\mathcal{L}_{\text{eff}} = \mathcal{L}_{\text{SM}} + \frac{1}{\Lambda^2} \sum_i c_i \mathcal{O}_i + \dots$$

for dimensionless coefficients c_i and a common suppression scale Λ . Through the global fit, limits are placed on the coefficients for operators or combinations of operators, which can be translated into constraints on particular BSM models.

The CLIC sensitivity to the operator coefficients c_i/Λ^2 for one operator basis set is shown in [Figure 9](#). Sensitivity to smaller values corresponds to probing higher mass scales. Sensitivities for the three CLIC energy stages are shown, along with preliminary HL-LHC sensitivities for comparison. The HL-LHC sensitivities are shown for two scenarios of systematic uncertainties: ‘S1’, where LHC Run 2 systematics are kept constant with integrated luminosity; and ‘S2’, where Run 2 theoretical uncertainties are halved and experimental uncertainties are scaled down with the square root of integrated luminosity until they reach a defined minimum [30, 40]. CLIC’s measurements in the Higgs, top, and EW sectors at all three energy stages are found to be highly synergistic. [Figure 9](#) shows that the initial stage of CLIC is already very complementary to the HL-LHC for many of the operators. The high-energy stages, which are unique to CLIC among all proposed e^+e^- colliders, are found to be crucial for the precision programme. For example, the operators c_{3W}, c_{2W} , and c_{2B} have effects that grow with energy. Hence, they can be probed better by observable measurements at high energy with even moderate accuracy, than they can by very accurate Higgs measurements. The operator c_6 relates to the Higgs self-coupling, and benefits from the direct double-Higgs production available at high energies. The overall result is to probe the SM-EFT much more precisely than is possible at the HL-LHC, to mass scales well beyond the centre-of-mass energy of the collider.

In the following sections, the direct and indirect sensitivities to some general models are discussed.

Extended Higgs sectors In many extensions of the Standard Model the scalar sector is extended by new states that are not charged under the Standard Model gauge group. These states, referred to as ‘singlet’ states, do not interact with Standard Model gauge bosons and fermions at tree level, but may acquire such interactions at loop level or through mixing with the Higgs boson radial mode. Through the couplings that the singlets ‘inherit’, their production and decay can be like Higgs bosons. Experimentally, therefore, they may be searched for directly as resonances, or indirectly through their modifications to the Higgs couplings.

In this example a singlet-like state ϕ that is heavier than twice the 125 GeV SM-like Higgs boson, decays to two SM-like Higgs bosons. Owing to the large branching fraction $H \rightarrow b\bar{b}$, the most promising final state comes from the decay to four b-quarks, which can be well identified at CLIC: $\phi \rightarrow HH \rightarrow b\bar{b}b\bar{b}$. This has been analysed using a fast simulation of the CLIC detector, including background processes.

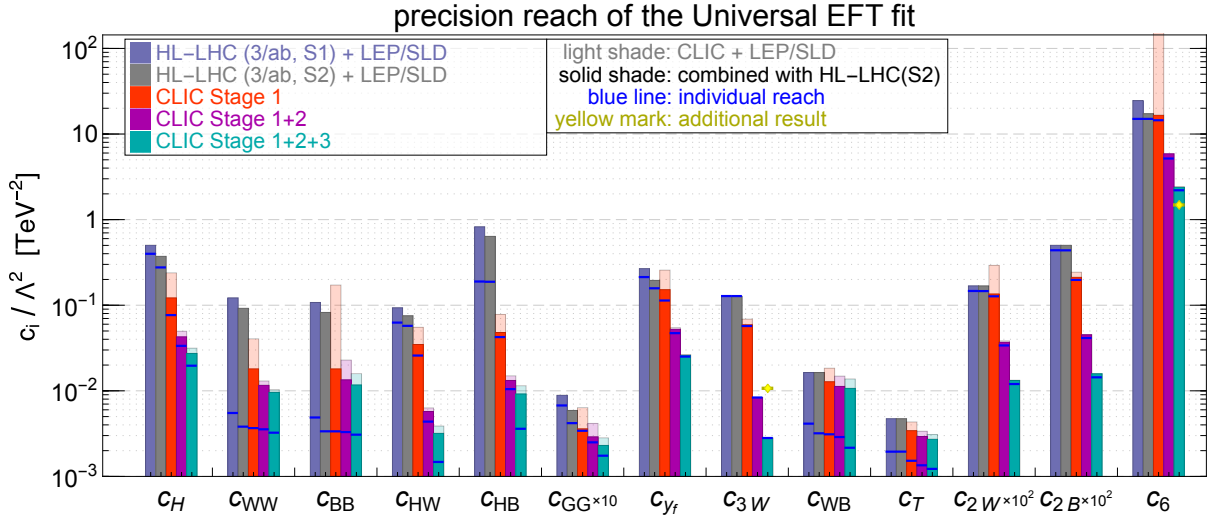


Figure 9: Summary of the sensitivity to SM-EFT operators c_i/Λ^2 from a global analysis of CLIC’s sensitivities to Higgs couplings, top-quark observables, WW production, and two-fermion scattering processes $e^+e^- \rightarrow f\bar{f}$, for three energy stages. Smaller values correspond to a higher scale probed. Preliminary projections for HL-LHC are shown for comparison, under two systematic uncertainty scenarios (described in text). Blue markers correspond to single-operator sensitivities, and yellow markers correspond to results from dedicated individual analyses (for example, the Higgs self-coupling analysis). From [16].

The phenomenology of the model is determined by $\sin \gamma$, where γ describes the mixing between the interaction eigenstates h_0 (a pure doublet of the weak interaction) and S (a real scalar singlet) to give the mass basis $H(125 \text{ GeV})$ and ϕ :

$$H = h_0 \cos \gamma + S \sin \gamma, \quad \phi = S \cos \gamma - h_0 \sin \gamma.$$

The parameter space of the mass of the heavy state ϕ , m_ϕ , and the mixing $\sin^2 \gamma$ can be explored, and the projected cross section bounds for the resonant final states translated into 95% C.L. limits as shown in Figure 10 [16, 41].

The CLIC Higgs coupling sensitivities also give an indirect constraint on $\sin^2 \gamma$, because the Higgs signal strengths are reduced universally by a factor $(1 - \sin^2 \gamma)$ from their SM values. This constraint is complementary to the direct search constraint, and is also shown as a horizontal line in Figure 10.

It is seen that the CLIC limits extend significantly beyond those projected for the HL-LHC, to much lower values of the mixing: for $m_\phi < 1 \text{ TeV}$, the mixing $\sin^2 \gamma$ must be lower than around 0.0013.

Model interpretations Many BSM models contain extra singlets of the kind generically described above, and so the same experimental measurements can be interpreted in different model frameworks. The next-to-minimal supersymmetric Standard Model, NMSSM, is the MSSM augmented by a single chiral super-field, and contains a scalar singlet. The above results have been translated into the NMSSM parameter space of m_ϕ and $\tan \beta$; in this framework the $\sqrt{s} = 1.5 \text{ TeV}$ stage of CLIC is already more sensitive than the HL-LHC over the whole parameter space, and the $\sqrt{s} = 3 \text{ TeV}$ stage significantly extends the reach. Similarly for Twin Higgs models, the $\sqrt{s} = 3 \text{ TeV}$ CLIC stage significantly surpasses the HL-LHC reach [16, 41].

Relaxions The examples above discuss heavy singlets. The case of light singlets can also be examined. One example comes from the relaxion mechanism, which stabilises the Higgs mass dynamically and is interesting for addressing the hierarchy problem. Similarly to the heavy singlets, the relaxion ϕ

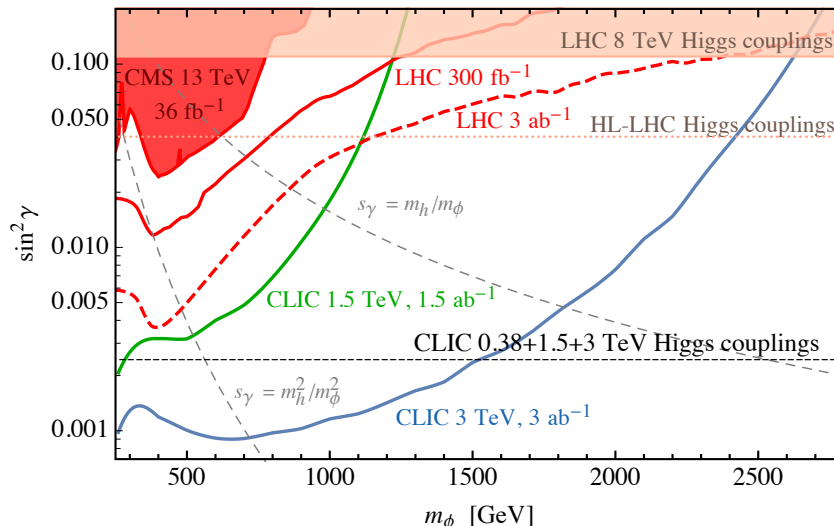


Figure 10: Constraints on singlet-like states ϕ at 95% C.L. in the plane $(m_\phi, \sin^2 \gamma)$. The reach from the direct search for $\phi \rightarrow HH \rightarrow b\bar{b}b\bar{b}$, for the second (green) and third (blue) CLIC stages are compared with the projections for LHC with a luminosity of 300 fb^{-1} (solid red) and 3 ab^{-1} (dashed red). Branching ratios of the ϕ have been fixed as $\text{BR}(\phi \rightarrow hh) = \text{BR}(\phi \rightarrow ZZ) = 25\%$. The horizontal line shows the indirect constraint from the CLIC Higgs couplings measurements (stat. only). The shaded regions are the present constraints from LHC direct searches for $\phi \rightarrow ZZ$ (red) and Higgs couplings measurements (pink). From [16, 41].

mixes with the Higgs and inherits its couplings to SM fields. The possible relaxation mass range spans from sub-eV to tens of GeV. For masses in the GeV range the relaxation is short-lived and decays inside the detector. At CLIC, three approaches have been considered: searching for the exotic decay $H \rightarrow \phi\phi$ directly via the decay $\phi \rightarrow b\bar{b}$ (extrapolated from ILC studies), constraining the decay $H \rightarrow \phi\phi$ indirectly via Higgs ‘untagged’ decays that, while not invisible, consist of soft particles that are not reconstructed as Higgs decays and appear as an extra invisible contribution to the Higgs width; and directly searching via the recoil mass in the process $e^+e^- \rightarrow \phi Z$. CLIC will have the potential to exclude masses down to 20 GeV with indirect searches and further down to 12 GeV with direct searches [16, 42], significantly reducing the available model parameter space beyond the reach of the HL-LHC in regions that are challenging for hadron colliders.

Dark matter The Higgsino is a compelling target of searches for supersymmetric extensions of the Standard Model: it is strongly connected to the naturalness of the weak scale, is important for gauge coupling unification, and is an ideal WIMP dark matter candidate. Naturalness considerations motivate Higgsinos in the range $m_\chi \lesssim \text{TeV}$, while the observed dark matter relic abundance singles out $m_\chi \simeq 1.1 \text{ TeV}$ for thermal Higgsino dark matter. High centre-of-mass lepton colliders such as CLIC provide one of the best avenues for probing Higgsinos across this mass range. A Higgsino that is not the lightest supersymmetric particle can decay into a SM boson and missing energy, and these cases have been examined in previous studies [3]. Here, two complementary approaches to searches for Higgsinos in challenging scenarios are discussed: searches for mono-photon signatures, and searches for disappearing stub track signatures.

Mono-photon signature In the search for dark matter candidates using ISR photons, $e^+e^- \rightarrow \chi\chi\gamma$, the experimental signature is a single photon reconstructed in the detector, while the χ particles escape undetected. A full simulation study at $\sqrt{s} = 380 \text{ GeV}$ has been carried out, including the main SM

background processes, for different values of m_χ . The 95% upper cross section limit for the process $e^+e^- \rightarrow \chi\chi\gamma$ is shown as a function of m_χ in Figure 11(a) [16]. It can be seen that CLIC at $\sqrt{s} = 380$ GeV would be sensitive to the $e^+e^- \rightarrow \chi\chi\gamma$ process down to cross sections of 5–10 fb in the mass range from the LEP limit of around 100 GeV up to almost 180 GeV, depending on the systematic error assumption, and Higgsino pair production with an ISR photon would be excluded across the entire mass range. The mono-photon-based search at an e^+e^- collider is complementary to mono-jet searches at hadron colliders as the different production mechanism allows the coupling to leptons to be probed. Also, once a signal is established, the photon energy distribution could be used to measure the mass of the dark matter candidate in a way that would be very difficult at a hadron collider. For a 120 GeV Higgsino particle, a precision on its mass of about 2 GeV is expected using the endpoint of the photon energy distribution.

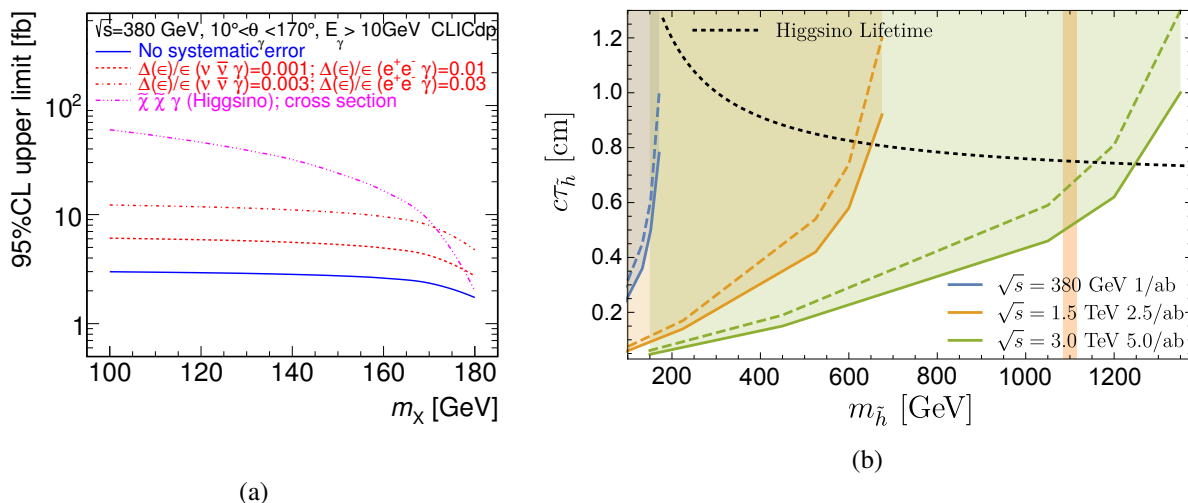


Figure 11: (a): 95% C.L. upper limit on the $e^+e^- \rightarrow \chi\chi\gamma$ cross section at $\sqrt{s} = 380$ GeV as a function of m_χ . The limit without including systematic uncertainties (blue) is compared to two different assumptions on the systematic uncertainty for the two main background processes (red). In addition, the cross section for Higgsino pair production with an ISR photon is shown (magenta). (b): 95% C.L. exclusion contours in lifetime–mass for $N = 3$ (solid) and $N = 30$ (dashed) Higgsino events in the detector acceptance at the three stages of CLIC. The black dashed line indicates the lifetime of the pure Higgsino state of a given mass, and the pure Higgsino thermal relic dark matter mass of 1.1 TeV is indicated by a vertical line. From [16].

Disappearing track signature A very different experimental signature for dark matter production could be ‘disappearing tracks’, for example caused by a heavy charged particle passing through the detector before decaying to a neutral particle that escapes detection. Generically, ‘long-lived particles’ could produce this signature. A particular example is the charged particle in a Higgsino multiplet, χ^\pm , which can be only slightly heavier than the neutral components $\chi_{1,2}^0$. In this case the χ^\pm travels a macroscopic distance, of order 1 cm, before decaying into an invisible χ^0 and SM states that are too soft to reconstruct: $\chi^\pm \rightarrow \pi^\pm \chi^0$. The charged Higgsino lifetime makes it particularly challenging for LHC searches, as the ‘charged stub’ left by the Higgsino is short and is challenging to reconstruct among the large number of hits from pile-up.

CLIC prospects for probing the pure Higgsino via the production of charged Higgsino pairs and the ensuing disappearing track signature have been assessed. The study does not use full simulation, but takes into account the CLIC detector geometry by requiring that the track stub traverses enough of the CLIC tracker to leave at least four hits. The most sensitive analysis comes from requiring a signature of only one charged stub; for which the 95% C.L. exclusion limits are shown in Figure 11(b) [16]. Possible

variations in the Higgsino lifetime, which may arise if the Higgsino is not exactly a pure state, are also given. It is seen that for $\sqrt{s} = 3 \text{ TeV}$, the 1-stub strategy yields around 30 events in the acceptance up to the thermal dark matter target of $m_\chi \simeq 1.1 \text{ TeV}$. A handful of events are produced in acceptance even if an ISR photon with $p_T > 100 \text{ GeV}$ is required. CLIC should therefore be able to probe the thermal relic Higgsino dark matter even with some level of background. The large tracker volume, compact vertex detector geometry and low background conditions compared to those at hadron colliders give CLIC better sensitivity for this type of signature than the HL-LHC.

Electroweak precision tests The process $e^+e^- \rightarrow f\bar{f}$, where f is a SM fermion, can be studied in depth at CLIC, for example through the differential cross section with respect to polar angle, $d\sigma/d\cos\theta$, and related asymmetries. Precision measurements of differential distributions and asymmetries are sensitive to corrections induced by any new state χ that has SM charges, which can modify the EW gauge boson propagators. This has been investigated by adding form factors to the effective Lagrangian and establishing 95% C.L. limits that could be set through a combination of the e, μ, b , and c channels on the masses of different states χ . These limits are shown in Figure 12 [16, 43], for the second and third stages of CLIC. The exclusions assume polarisation fractions $P(e^-) = -80\%$ and $P(e^+) = 0$. Limits are given for different states $\chi \sim (1, n, Y)$, where the entries denote the $SU(3)_c \times SU(2)_L \times U(1)_Y$ representation; and for different Lorentz representations: complex scalar (CS), Majorana fermion (MF), and Dirac fermion (DF). For example, the $n = 2$ Dirac fermion corresponds to the Higgsino and the $n = 3$ Majorana fermion to the wino. The limits show that CLIC at $\sqrt{s} = 3 \text{ TeV}$ excludes the $n = 3$ Dirac fermion for $m_\chi < 0.8 \text{ TeV}$ and $1 \text{ TeV} < m_\chi < 2 \text{ TeV}$; and in addition the intermediate region $0.8 \text{ TeV} < m_\chi < 1 \text{ TeV}$ is covered by CLIC at $\sqrt{s} = 1.5 \text{ TeV}$. For the $n = 3$ Dirac fermion, a mass of $m_\chi = 2 \text{ TeV}$ is needed to saturate the dark matter relic abundance [16, 43], and so CLIC covers the whole relevant parameter space and fully tests that dark matter hypothesis.

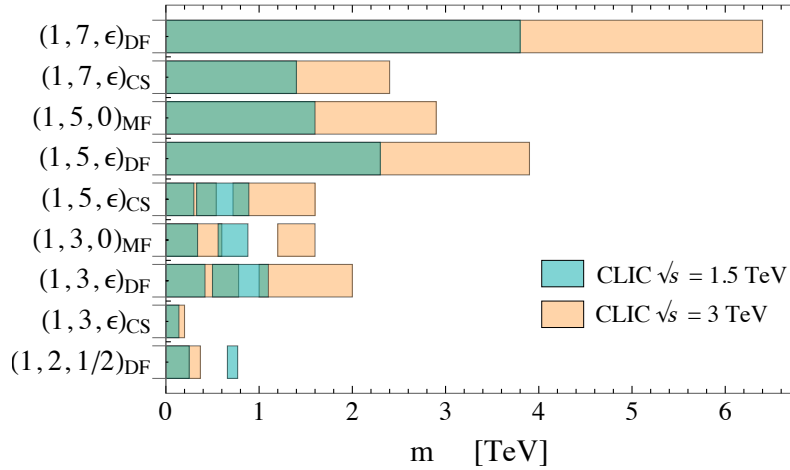


Figure 12: 95% C.L. exclusion ranges on the mass of new SM-charged states from $e^+e^- \rightarrow f\bar{f}$ precision measurements for $P_{e^-} = -80\%$ data at $\sqrt{s} = 1.5 \text{ TeV}$ (blue) and 3 TeV (beige). Green regions would be excluded by data from both centre-of-mass energies. Exclusion regions are obtained by combining the e, μ, b , and c channels with 0.3% systematic error. $(1, n, Y)$ denotes the $SU(3)_c \times SU(2)_L \times U(1)_Y$ representation of the state, and the mass exclusions are given for different Lorentz representations: complex scalar (CS), Majorana fermion (MF), and Dirac fermion (DF). ϵ denotes a milli-charge which has no bearing on collider physics, but ensures stability. From [16, 43].

Electroweak phase transition The SM plus singlet scenario discussed previously can be used to probe the nature of the electroweak phase transition in the early universe. As the universe expanded it cooled, and electroweak symmetry breaking occurred when it became energetically favourable for the Higgs field to acquire a non-zero vacuum expectation value. If there is a potential barrier separating the symmetric vacuum from the broken one, the electroweak phase transition could be first order. The addition of a singlet can result in such a first-order electroweak phase transition. A strong first-order phase transition is a necessary condition for electroweak baryogenesis, so the shape of the Higgs potential and the nature of the electroweak phase transition is a critical open question that could shed light on the stability or instability of the vacuum, and potentially on the origin of the baryon asymmetry.

CLIC can search for resonant double-Higgs production arising from a singlet, as well as looking for deviations from SM predictions for the Higgsstrahlung cross section and the Higgs self-coupling. These measurements can set limits on the parameter space for general scenarios that lead to a strong first-order phase transition. Examples are shown in Figure 13 [16, 44]. The parameter space has been scanned for various fixed values of the singlet mass and singlet mixing; shown here is the singlet mass $m_2 = 500\text{ GeV}$ and two values of the mixing: $\sin \theta = 0.05$, and 0.1 . Values of $\sin \theta$ higher than around 0.2 will be excluded by HL-LHC. The parameter space is that of coefficients a_2 , b_3 , and b_4 of additional T^2 terms in a temperature-dependent effective potential that is added to the Higgs potential and modifies the behaviour as the early universe expands and cools. Points in the parameter space compatible with unitarity, perturbativity, and absolute stability of the EW vacuum have been identified (red circles), and among them the points yielding a strong first-order phase transition have been identified (green circles). Constraints are provided by a fit to an overall rescaling of the Higgs couplings $\Delta\kappa$ (grey regions), the Higgs self-coupling (black lines), and by searches for resonant double-Higgs production in the 4b final state at $\sqrt{s} = 1.4\text{ TeV}$ and 3 TeV (orange and blue lines). The excluded regions are the regions outside the pairs of lines, for higher absolute values of a_2 .

The three complementary methods are all competitive in the interesting region and in the examples in Figure 13 are able to exclude all of the interesting parameter space. CLIC therefore provides a direct avenue to probe the nature of the EW phase transition for non-minimal scalar sectors, and the possible origin of the cosmic matter-antimatter asymmetry via electroweak baryogenesis.

2.5 Overall CLIC physics reach

This section has presented a selection of recent studies to illustrate the overall CLIC physics reach.

In Higgs physics, the initial CLIC energy stage already provides coupling measurements that are in many cases significantly more precise than for the HL-LHC. The higher CLIC energy stages improve upon these, and give access to further couplings. Measured in e^+e^- collisions, the couplings can be determined in a model-independent way; at CLIC they can reach precisions at the percent level, while the model-dependent precisions reach the per-mille level. The Higgs self-coupling can be determined at the level of $[-7\%, +11\%]$. CLIC can measure the top-quark mass at the level of 50 MeV , including current theory systematics. Measurements of top-quark production and decay properties at all three energy stages can be used to probe the top-quark couplings, and give sensitivity to potential new physics scenarios such as top compositeness or CP violation in the ttH coupling.

All of these SM probes, together with measurements of diboson and Drell-Yan production, can be combined and interpreted in the SM-EFT framework. In this way the precision studies at CLIC allow sensitivity to physics beyond the SM that originates from scales at tens of TeV, well above the centre-of-mass energy of the collider. The high energy stages of CLIC, and the electron polarisation afforded by the linear collider, gives sensitivity beyond that achievable at other colliders.

General examples have been given to show that through direct searches, CLIC is sensitive to new particles produced in a wide range of new physics scenarios, including those that are challenging

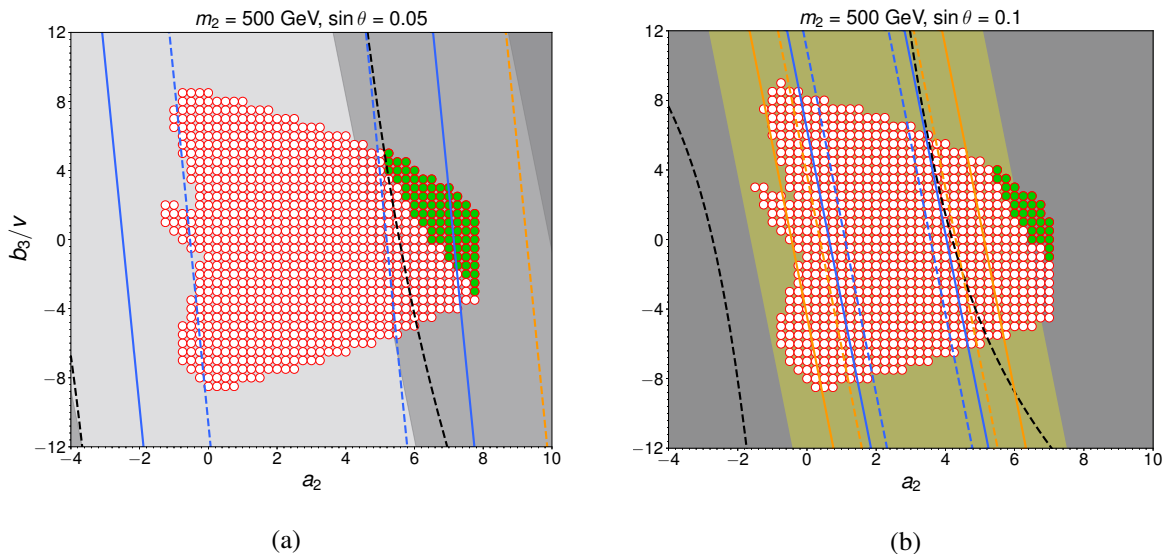


Figure 13: Region of parameter space in $(a_2, b_3/v)$ for singlet mass $m_2 = 500\text{ GeV}$ and singlet mixing (a) $\sin\theta = 0.05$ and (b) $\sin\theta = 0.1$ within the 95% C.L. sensitivity reach of resonant double-Higgs production searches at CLIC. Limits are given for $\sqrt{s} = 1.4\text{ TeV}$ (orange) and $\sqrt{s} = 3\text{ TeV}$ (blue) for a b -tagging efficiency of 70% (solid) and 90% (dashed): the CLIC sensitivity is the region not contained within each pair of sensitivity lines. The red circles indicate the region compatible with the requirements of unitarity, perturbativity and absolute stability of the EW vacuum. The parameter b_4 has been scanned over. Overlaid is the region yielding a strongly first order EW phase transition (green points). The dashed black lines are 95% C.L. lines corresponding to the 68% C.L. CLIC sensitivity $[-7\%, +11\%]$ on the Higgs self-coupling. The yellow band (only for $\sin\theta = 0.1$) corresponds to the projected sensitivity of $pp \rightarrow h_2 \rightarrow ZZ$ searches at HL-LHC. The region within reach of a measurement of an overall scaling of Higgs couplings $\Delta\kappa$ from the first, second, and third CLIC stages is shown in dark, middle, and light grey, respectively. From [16, 44].

experimentally. These scenarios include extended Higgs sectors and a variety of dark matter candidates. Combining the direct and indirect searches provides a direct avenue to probe the nature of the EW phase transition for non-minimal scalar sectors, and the possible origin of the cosmic matter-antimatter asymmetry via electroweak baryogenesis.

Previous studies have demonstrated that if particles are discovered at CLIC or the LHC, CLIC has the ability to measure their masses and couplings at the percent level or better: typically much more precisely than is possible at a hadron collider [3].

A summary of these and further studies showing the overall reach for many aspects of potential new physics is given in Table 4. For example, new particles can be discovered directly over the whole CLIC kinematic reach, under many new physics scenarios, and the sensitivity to high energy scales from EFT fitting is complemented by limits on new physics scales in particular sectors arising from dedicated searches, such as those for lepton flavour violation.

Overall, the stand-alone discovery and precision capacity of CLIC, complementary to that of the HL-LHC, makes it an ideal facility for extending the search for physics beyond the SM.

Table 4: CLIC reach for new physics. Sensitivities are given for the full CLIC programme covering the three centre-of-mass energy stages at $\sqrt{s} = 380\text{ GeV}$, 1.5 TeV and 3 TeV with integrated luminosities of 1 ab^{-1} , 2.5 ab^{-1} and 5 ab^{-1} , respectively. At 380 GeV , equal amounts of -80% and $+80\%$ polarisation running are assumed. Above 1 TeV a sharing in the ratio $80:20$ is assumed between -80% and $+80\%$ electron polarisation. All limits are at 95% C.L. unless stated otherwise.

Process	HL-LHC	CLIC
Heavy Higgs scalar mixing angle $\sin^2 \gamma$	$< 4\%$	$< 0.24\%$
Higgs self-coupling $\Delta\lambda$	$\sim 50\%$ at 68% C.L.	$[-7\%, +11\%]$ at 68% C.L.
BR($H \rightarrow$ invisible)		$< 0.69\%$ at 90% C.L.
Higgs compositeness scale m_*	$m_* > 3\text{ TeV}$ ($> 7\text{ TeV}$ for $g_* \simeq 8$)	Discovery up to $m_* = 10\text{ TeV}$ (40 TeV for $g_* \simeq 8$)
Top compositeness scale m_*		Discovery up to $m_* = 8\text{ TeV}$ (20 TeV for small coupling g_*)
Higgsino mass (disappearing track search)	$> 250\text{ GeV}$	$> 1.2\text{ TeV}$
Slepton mass		Discovery up to $\sim 1.5\text{ TeV}$
RPV wino mass		$> 1.5\text{ TeV}$ ($0.03\text{ m} < c\tau < 30\text{ m}$)
Z' (SM couplings) mass	Discovery up to 7 TeV	Discovery up to 20 TeV
NMSSM scalar singlet mass	$> 650\text{ GeV}$ ($\tan\beta = 4$)	$> 1.5\text{ TeV}$ ($\tan\beta = 4$)
Twin Higgs scalar singlet mass	$m_\sigma = f > 1\text{ TeV}$	$m_\sigma = f > 4.5\text{ TeV}$
Relaxion mass	$< 24\text{ GeV}$	$< 12\text{ GeV}$ (all for vanishing $\sin\theta$)
Relaxion mixing angle $\sin^2 \theta$		$\leq 2.3\%$
Neutrino Type-2 see-saw triplet		$> 1.5\text{ TeV}$ (for any triplet VEV) $> 10\text{ TeV}$ (for triplet Yukawa coupling $\simeq 0.1$)
Inverse see-saw RH neutrino		$> 10\text{ TeV}$ (for Yukawa coupling $\simeq 1$)
Scale $V_{LL}^{-1/2}$ for LFV ($\bar{e}e$)($\bar{e}\tau$)		$> 42\text{ TeV}$

3 CLIC accelerator design, technologies and performance

3.1 Introduction

The aim of the studies for CLIC has been to develop the designs and the technologies to enable the building of a multi-TeV electron–positron collider. The feasibility of the concept and the technologies has been documented in the CLIC CDR [2]. As reported in Section 2, the new staged approach to the project optimally addresses the physics needs. The accelerator design, technologies and implementation have recently been optimised for the first energy stage at 380 GeV, while fully taking upgrades to 1.5 TeV and 3 TeV into account. The following will summarise the CLIC design and parameters for the first energy stage, present a klystron-based alternative, and show the staging to higher energies.

3.2 CLIC design and performance at 380 GeV

3.2.1 Design overview

The schematic layout of the baseline CLIC complex for 380 GeV operation is shown in Figure 14 and the key parameters for all three energy stages are listed in Table 5.

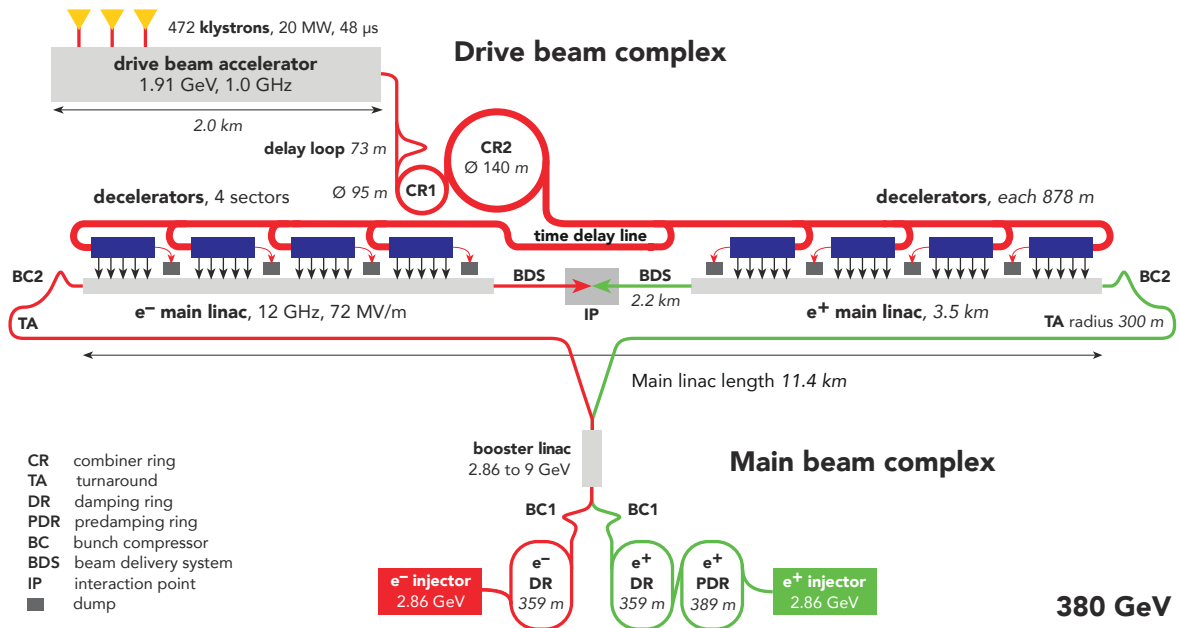


Figure 14: Schematic layout of the CLIC complex at 380 GeV. (image credit: CLIC)

The main electron beam is produced in a conventional radio-frequency (RF) source and accelerated to 2.86 GeV. The beam emittance is then reduced in a damping ring. To produce the positron beam, an electron beam is accelerated to 5 GeV and sent into a crystal to produce energetic photons, which hit a second target and produce electron–positron pairs. The positrons are captured and accelerated to 2.86 GeV. Their beam emittance is reduced first in a pre-damping ring and then in a damping ring. The ring to main linac system (RTML) accelerates the beams to 9 GeV and compresses their bunch length. The main linacs accelerate the beams to the beam energy at collision of 190 GeV. The beam delivery system removes transverse tails and off-energy particles with collimators and compresses the beam to

Table 5: Key parameters of the CLIC energy stages.

Parameter	Symbol	Unit	Stage 1	Stage 2	Stage 3
Centre-of-mass energy	\sqrt{s}	GeV	380	1500	3000
Repetition frequency	f_{rep}	Hz	50	50	50
Number of bunches per train	n_b		352	312	312
Bunch separation	Δt	ns	0.5	0.5	0.5
Pulse length	τ_{RF}	ns	244	244	244
Accelerating gradient	G	MV/m	72	72/100	72/100
Total luminosity	\mathcal{L}	$10^{34} \text{ cm}^{-2} \text{ s}^{-1}$	1.5	3.7	5.9
Luminosity above 99% of \sqrt{s}	$\mathcal{L}_{0.01}$	$10^{34} \text{ cm}^{-2} \text{ s}^{-1}$	0.9	1.4	2
Total integrated luminosity per year	\mathcal{L}_{int}	fb^{-1}	180	444	708
Main linac tunnel length		km	11.4	29.0	50.1
Number of particles per bunch	N	10^9	5.2	3.7	3.7
Bunch length	σ_z	μm	70	44	44
IP beam size	σ_x/σ_y	nm	149/2.9	$\sim 60/1.5$	$\sim 40/1$
Normalised emittance (end of linac)	$\varepsilon_x/\varepsilon_y$	nm	900/20	660/20	660/20
Final RMS energy spread		%	0.35	0.35	0.35
Crossing angle (at IP)		mrad	16.5	20	20

the small sizes required at the collision point. After the collision the beams are transported by the post collision lines to the respective beam dumps.

The RF power for each main linac is provided by a high current, low-energy drive beam that runs parallel to the colliding beam through a sequence of power extraction and transfer structures (PETS). The drive beam generates RF power in the PETS that is then transferred to the accelerating structures by waveguides.

The drive beam is generated in a central complex with a fundamental frequency of 1 GHz. A $48 \mu\text{s}$ long beam pulse is produced in the injector and fills every other bucket, i.e. with a bunch spacing of 0.6 m. Every 244 ns, the injector switches from filling even buckets to filling odd buckets and vice versa, creating 244 ns long sub-pulses. The beam is accelerated in the drive-beam linac to 1.91 GeV. A 0.5 GHz resonant RF deflector sends half of the sub-pulses through a delay loop such that its bunches can be interleaved with those of the following sub-pulse that is not delayed. This generates a sequence of 244 ns trains in which every bucket is filled, followed by gaps of the same 244 ns length. In a similar fashion three of the new sub-pulses are merged in the first combiner ring. Groups of four of the new sub-pulses, now with 0.1 m bunch distance, are then merged in the second combiner ring. The final pulses are thus 244 ns long and have a bunch spacing of 2.5 cm, i.e. providing 24 times the initial beam current. The distance between the pulses has increased to $24 \times 244 \text{ ns}$, which corresponds to twice the length of a 878 m decelerator. The first four sub-pulses are transported through a delay line before they are used to power one of the linacs while the next four sub-pulses are used to power the other linac directly. The first sub-pulse feeds the first drive-beam decelerator, which runs in parallel to the colliding beam. When the sub-pulse reaches the decelerator end, the second sub-pulse has reached the beginning of the second drive-beam decelerator and will feed it, while the colliding beam has meanwhile reached the same location along the linac.

3.2.2 Main-beam design considerations and choices

The CLIC target luminosity at 380 GeV is $\mathcal{L} = 1.5 \times 10^{34} \text{ cm}^{-2} \text{ s}^{-1}$. The nominal beam parameters at the interaction point are given in [Table 5](#). Reaching the energy goal requires achieving the target gradient in the accelerating structures. This in turn requires that the structures can sustain the gradient and that the drive beam provides enough power. In addition, to reach the luminosity goal, the colliding beam needs to have a high current and an excellent quality. Thorough studies established a feasible concept for the 380 GeV stage [2]. Based on this the first stage has been designed. The key considerations are:

- The choice of bunch charge and length ensures stable transport of the beam. The main limitation arises from short-range wakefields in the Main Linac.
- The spacing between subsequent bunches ensures that the long-range wakefields in the Main Linac can be sufficiently damped to avoid beam break-up instabilities.
- The horizontal beam size at the collision point ensures that the beamstrahlung caused by the high beam brightness is kept to an acceptable level for the given bunch charge. This ensures a luminosity spectrum consistent with the requirements of the physics experiments.
- The horizontal emittance is dominated by single particle and collective effects in the Damping Rings and includes some additional contributions from the Ring To Main Linac.
- The vertical emittance is given mainly by the Damping Ring and additional contributions from imperfections of the machine implementation. The target parameters take into account budgets for detrimental effects from static and dynamic imperfections such as component misalignments and jitter.
- The vertical beta-function is the optimum choice in terms of luminosity. The horizontal beta-function is determined by the combination of required beam size and horizontal emittance.

In summary, the parameters are largely determined by fundamental beam physics and machine design with the exception of the vertical emittance that is determined by imperfections. Without them a luminosity of $\mathcal{L} = 4.3 \times 10^{34} \text{ cm}^{-2} \text{ s}^{-1}$ would be achieved.

3.2.3 Performance of the drive-beam concept

The successful technology demonstration of the CLIC accelerating gradient is discussed in [Section 3.5](#). The main performance limitation arises from vacuum discharge, i.e. breakdowns; a rate of less than $3 \times 10^{-7} \text{ m}^{-1}$ is required for the target gradient of 72 MV/m. The key parameters for the accelerating structure and the beam have been optimised together. In particular, structures with smaller iris apertures achieve higher gradients for the same breakdown rate, but they reduce the maximum bunch charge for stable beam transport because they produce stronger wakefields.

To test the drive-beam concept, the third CLIC Test Facility (CTF3) [6] was constructed and operated by an international collaboration. It has addressed the key points of the concept:

- The stable acceleration of the initial high-current drive beam in the accelerator.
- The high transfer efficiency from the RF to the drive beam.
- The generation of the final drive-beam structure using the delay loop and a combiner ring.
- The quality of the final drive beam. In particular, feedback has been used to stabilise the drive-beam current and phase to ensure correct main-beam acceleration. CTF3 achieved the drive-beam phase stability that is required for CLIC [45–47].
- The use of the drive beam to accelerate the main beam and the performance of the associated hardware. The main beam has been accelerated with a maximum gradient of 145 MV/m.

CTF3 established the feasibility of the drive-beam concept and the ability to use this scheme to accelerate

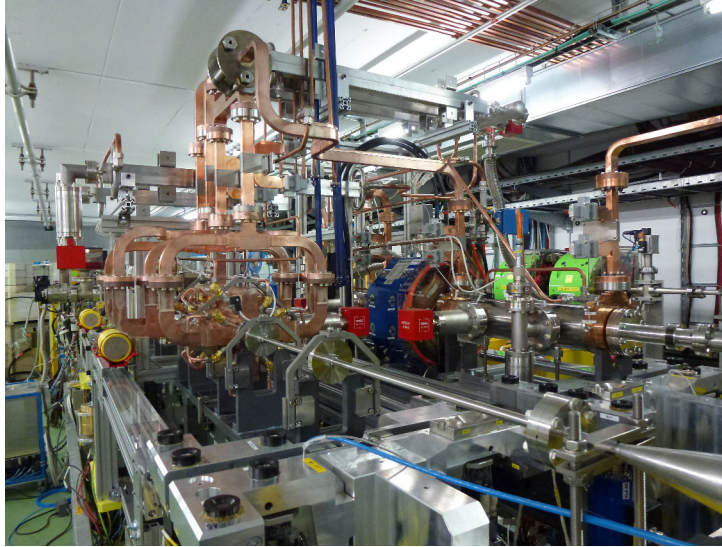


Figure 15: The two-beam acceleration test stand in the CTF3 facility. The drive beam enters from the middle-right, while the probe (main) beam enters from the bottom-right. (image credit: CLIC)

the main beam. [Figure 15](#) shows the corresponding two-beam acceleration test stand in the CTF3 facility.

It has also been instrumental in developing all the different hardware components that are essential for the scheme – among them the drive-beam gun, the bunch compressor, the drive-beam accelerating structures, RF deflectors, the PETS including a mechanism to switch them off individually, the power distribution waveguide system, fast-feedback systems, drive-beam current and phase monitors, as well as other instrumentation. CTF3 stopped operation after successfully completing its experimental programme in December 2016 and a new facility, CLEAR, has started to operate. It re-uses the CTF3 main-beam installations and additional hardware to address further beam dynamics with the focus on the main beam.

3.2.4 Luminosity performance

For static imperfections, the vertical emittance growth budgets are the same at 380 GeV and 3 TeV and they correspond to the values described in the CDR [2]. It is required that each system, i.e. RTML, Main Linac and BDS, remains within its emittance budget with a likelihood of more than 90% without further intervention. The key static imperfection is the misalignment of the beamline components with respect to the design. A sophisticated system has been developed and tested that provides a spacial reference frame with unprecedented accuracy, see [Section 3.5](#). The Main Linac and BDS components are mounted on movable supports and can be remotely aligned with respect to the reference system. In addition, the main linac accelerating structures are equipped with wakefield monitors that allow the measurement and correction of their offset with respect to the beam. Dispersion-free steering, which has been successfully tested at the SLAC Facility for Advanced Accelerator Experimental Tests (FACET), will further reduce the emittance growth using high-resolution Beam Position Monitors (BPM). In the BDS, additional tuning is required using optical knobs that move several multi-pole magnets simultaneously to correct the optics properties.

The performance specifications for the alignment systems and instrumentation are kept the same at 380 GeV and 3 TeV and correspond to the CDR description. They are sufficient to achieve the required performance at 3 TeV and most of them could be relaxed for the first energy stage, typically by about a factor of two, to meet the same emittance budget. However, the original, better performances are required

for the upgrade to the higher energy stages. No substantial cost saving has been identified by relaxing the specifications for the first stage. Therefore, it has been decided to ensure that the system is consistent with the final energy from the very beginning, thus avoiding the need for upgrades of the already existing hardware. This also provides additional margin for achieving the required luminosity.

The tuning procedures for the RTML and the BDS have been improved compared to the CDR. Studies of the static imperfections in the RTML [48], the Main Linac [49] and the BDS [50] show that the target budgets can be met in each system with a margin; in the BDS, the tuning is now also much faster. Combining these effects, one can expect an average luminosity of $\mathcal{L} = 3 \times 10^{34} \text{ cm}^{-2} \text{ s}^{-1}$, about twice the luminosity target at 380 GeV [50].

Also, for the dynamic imperfections the vertical emittance budgets are the same for 380 GeV and 3 TeV. Key imperfections are the movement of components due to ground motion or technical noise, phase and amplitude jitter of the drive beam, and potentially dynamic magnetic fields.

The level of ground motion is site dependent; measurements in the LEP tunnel showed very small motion [51] while measurements in the CMS detector hall showed much larger motion [52]. With the new design of the final focus system, all relevant accelerator components are mounted in the tunnel of the collider, so one can expect ground motion levels similar to the LEP tunnel. However, for the ground motion studies the level of the CMS detector hall has been used in order to evaluate the robustness of the solutions. The ground motion is mitigated by the design of the magnets, a mechanical feedback that decouples them from the ground, and by beam-based feedback on trajectories. Prototypes of the mechanical feedback have been tested successfully. In the CDR, detailed studies of the 3 TeV stage showed that the performance goal can be met with margin. Studies of the 380 GeV case [46] confirm that ground motion will only use about 10% of the budget allocated to dynamic imperfections.

Dynamic magnetic stray fields deflect the colliding beams, leading to trajectory jitter and emittance growth, thus reducing luminosity. Their impact is particularly large in the RTML and the BDS. In the latter they are more important at 380 GeV than at 3 TeV due to the lower beam energy. A study in collaboration with experts from the Hungarian Geophysics Institute has commenced to investigate these fields and define the mitigation technologies. The magnetic fields can originate from different sources: natural sources, such as geomagnetic storms; environmental sources, such as railway trains and power lines and technical sources, i.e. from the collider itself. A survey of natural sources showed that they should not affect the luminosity [53] and a measurement station has been established in the Jura mountains near CERN to collect long-term regional data. The study of the environmental and technical sources has started but is not yet complete. Preliminary estimates have been performed using the magnetic field variations that were measured in the LHC tunnel. They concluded that a thin mu-metal shield of the drifts in the RTML and BDS can bring the fields down to a level that does not impact luminosity [46].

Further development of the foreseen technical and beam-based imperfection mitigation systems should allow for a reduction in the emittance budgets and an increase in the luminosity target. Also, new systems could be devised to this end. As an example, the addition of a few klystron-powered, higher-frequency accelerating structures could allow to reduce the energy spread of the colliding beams, which can improve the luminosity and also the luminosity spectrum for specific measurements such as the top-quark threshold scan.

3.2.5 Operation and availability

The machine protection and operational considerations and strategies at 380 GeV are similar to those at 3 TeV and are described in the CDR [2]. Machine protection relies on passive protection and the processing of the diagnostics data between two beam pulses to generate a beam permit signal.

The tentative plan for the operation of CLIC includes a yearly shutdown of 120 days. In addition

30 days are foreseen for the machine commissioning, 20 days for machine development and 10 days for planned technical stops. This leaves 185 days of operation for the experiments. The target availability for the experiments during this period is 75%. Hence the integrated luminosity per year corresponds to operation at full luminosity for 1.2×10^7 s [54]. An optimisation of the schedule has started which will also refine the trade-off between planned short stops and availability to reach the integrated luminosity goal.

Different events can impact both operation and availability and can be roughly categorised as:

- Events that do not require an intervention in the machine and are handled by the control system. These include RF breakdowns in the accelerating structures, which will lead to a small energy error and potentially slight transverse deflection of the beam. Typically this will happen only every 100 beam pulses and will be corrected by the feedback systems.
- Events that require a short stop on the machine but no intervention, such as a false trigger of the machine protection system – e.g. caused by a single event upset. In this case, the machine can be brought back to full intensity in a few seconds.
- Failures of machine components that might compromise the performance but do not require stopping the beam. This includes failures of klystrons or instrumentation. These are mitigated by providing sufficient reserve.
- Failures that require to stop the beam and repair the machine. This is the case for failures of power converters.

Based on an assessment of the complexity of the different systems, an availability goal has been defined for each of them. This allows investigation of individual systems and focus on the key issues.

A number of key failures has been studied in detail, in particular of magnet power converters and RF power systems. In the drive-beam accelerator, a reserve of 5% RF units are installed and klystrons operate below their maximum power. If one fails, the power of the others is increased accordingly. Similarly, BPMs and orbit corrector failures in the main linac compromise the correction of ground motion. However, if 10% of them fail, the effect of ground motion is only increased by 14%. During the technical stops failed klystrons and instrumentation can be replaced. The CLIC lattice design has been optimised to minimise the impact of power converter failures. In particular in the drive beam, the many quadrupoles are powered in groups to minimise the number of power converters and small trims adjust their strength as needed. Compared to individual powering, this strongly increases the mean time between failures, since failures of trims can be mitigated to a large extent. A similar strategy is used for the main-beam quadrupoles.

Detailed studies will be required during the technical design phase covering all components to ensure that the availability goal can be met. Currently, considering key failures, no obstacle has been identified to reaching the target availability.

3.2.6 Energy flexibility

The beam parameters can be adjusted to different physics requirements. In particular, the collision energy can be adjusted to the requirements by lowering the gradient in the main linacs accordingly. For a significantly reduced gradient, the bunch charge will have to be reduced in proportion the energy to ensure beam stability. However, at this moment the only operation energy different from 380 GeV that is required is around 350 GeV to scan the top-quark pair-production threshold. In this case, the bunch charge can remain constant. The RF phases of the accelerating structures are slightly modified compared to the 380 GeV case in order to achieve an RMS beam energy spread of only 0.3%. This allows reaching a luminosity of $\mathcal{L} = 1.5 \times 10^{34} \text{ cm}^{-2} \text{ s}^{-1}$, similar to the 380 GeV goal.

Also the beam energy can be reduced at the cost of some reduction in luminosity. For example,

at the top-quark threshold, one can reduce the bunch charge by 10% and increase its length by 10%. This would keep the wakefield effects in the main linac constant. This configuration slightly reduces the luminosity to $\mathcal{L} = 1.18 \times 10^{34} \text{ cm}^{-2} \text{ s}^{-1}$, but reduces the beam energy spread to 0.2%. Similarly, it is possible to reduce the beamstrahlung by increasing the horizontal beam size, if the reduced luminosity is out-weighted by the improved luminosity spectrum.

Operation at much lower energies can also be considered. At the Z-pole, between 2.5 fb^{-1} and 45 fb^{-1} can be achieved per year for an unmodified and a modified collider, respectively.

3.2.7 Beam experiments

Beam experiments and hardware tests provide the evidence that the CLIC performance goals can be met. Some key cases are discussed in the following:

- The novel drive-beam scheme has been demonstrated in CTF3, as discussed in [Section 3.2.3](#).
- The Stanford Linear Collider (SLC) [55], the only linear collider so far, is a proof of principle for the linear collider concept and contributed important physics data at the Z-pole. The SLC achieved collision beam sizes smaller than nominal, but did not reach the nominal bunch charge [56]. Two collective effects led to the charge limitations. They have been fully understood and are not present in the CLIC design.
- The electron polarisation that has been achieved at collision in SLC is similar to the CLIC goal.
- The strong beam–beam effect increases the luminosity in CLIC. This effect has been observed at the SLC, in agreement with the theoretical predictions [57].
- Modern light sources achieve CLIC-level vertical emittances, in particular the Swiss Light Source and the Australian Light Source [58–60].
- CLIC parameters require strong focusing at the IP. This focusing has been demonstrated at two test facilities, FFTB [61] at SLAC and the Accelerator Test Facility ATF2 [7, 8] at KEK. The achieved vertical beam sizes were 40% and 10% above the respective design values for these test facilities. In the super B-factory at KEK the beams will perform many turns through the final focus system, still one aims at beta-functions that are only a factor three larger than in CLIC, and even smaller beta-functions similar to the CLIC values are being discussed [62].
- The use of beam-based alignment, i.e. dispersion free steering [63, 64] to maintain small emittances in a linac has successfully been tested in FACET [9] and FERMI [10].
- The effective suppression of harmful long-range wakefields has been tested with beam in the CLIC accelerating structures [65].
- The novel precision pre-alignment system of CLIC and sophisticated beam-based alignment and tuning ensure the preservation of the beam quality during transport. The alignment system is based on a concept developed for the LHC interaction regions, but with improved performance. Prototypes have been built and successfully tested, see [Section 3.5.3](#).
- Quadrupole jitter has been an important source of beam jitter in the SLC. For CLIC this has been addressed by designing the magnet supports to avoid resonances at low frequencies and by developing an active stabilisation system for the magnets, which demonstrated a reduction of the jitter to the sub-nanometre regime, see [Section 3.5.3](#).
- CLIC requires excellent relative timing at the 50 fs level over the collider complex. CTF3 has demonstrated the phase monitor and correction with fast feed-forward. Modern Free Electron Lasers (FEL) have developed the technology to provide the timing reference over large distances.
- High availability is key to achieve the luminosity goal. The very reliable routine operation of light sources, FELs, the B-factories and the LHC provide concepts to address this issue.

In conclusion, the CLIC parameters are ambitious but are supported by simulation studies, measured hardware performances and beam tests. This gives confidence that the goals can be met. More details on the performance benchmarks can be found in the Project Implementation Plan [66].

3.3 A klystron-based CLIC at 380 GeV

An alternative design for the 380 GeV stage of CLIC is based on the use of X-band klystrons to produce the RF power for the main linac. On the one hand, this solution increases the cost of the main linac because the klystrons and modulators are more expensive than the drive-beam decelerator and also because a larger tunnel is needed to house the additional equipment. On the other hand, it avoids the substantial cost of the construction of the drive-beam complex and makes the linac more modular. One can therefore expect a competitive cost at low energies while the drive-beam solution leads to lower cost at high energies. The upgrade of the complex is cheaper with a drive-beam based design, since the additional cost to upgrade the drive-beam complex to feed a longer linac is relatively modest. However, an important advantage of the klystron-based design is that the main linac modules can easily be fully tested for performance when they are received. In contrast, the drive-beam option requires the construction of a substantial complex that can produce a 100 A drive beam before modules can be fully tested. The klystron-based option could therefore be implemented more rapidly than the drive-beam based solution.

3.3.1 Design choice

The klystron-powered design is based on a study [5] that uses the same optimisation tools as for the drive-beam based option. The main linac model has been replaced with one that consists of a sequence of RF units, each powered by klystrons, see Section 3.5.7, and the drive-beam complex has been removed. A cost model for the klystrons and modulators is included. Based on the conclusions of the study, a tentative accelerating structure and a parameter set have been chosen for this design. The optimum structure differs from the drive-beam based design. It is slightly shorter and has a smaller aperture. If one were to use the same accelerating structure as for the drive-beam based design, the expected cost would be about 330 MCHF higher.

As can be seen in Table 6, the beam emittance, energy spread and charge of the klystron-based design are very similar to the 380 GeV parameters, while the bunch is somewhat longer. The vertical emittance is also the same as for the drive-beam based design, while the horizontal emittance is smaller and proportional to the bunch charge. The number of bunches per train is significantly higher in order to produce the required luminosity.

The evolution of the vertical emittance along the collider is similar to the drive-beam based design, while the horizontal emittance corresponds to the 380 GeV design. The horizontal and vertical emittances remain below 500 nm and 5 nm at extraction from the damping ring, below 600 nm and 10 nm at injection into the main linac and below 630 nm and 20 nm at the end of the main linac. At the interaction point they will be below 660 nm and 30 nm, respectively.

3.3.2 Design implications

For the klystron-based alternative, the main linac has been redesigned to evaluate the cost and verify the beam dynamics. No design optimisation has been performed for the other systems. It is expected that these have only minor impact on cost and system performance, as detailed below.

The RF design of the klystron-based injector has to differ from the drive-beam based case in order to accommodate the longer bunch train. However, the total charge per pulse is the same in both cases. Hence, to first order the same amount of installed RF is required. However, the choice of accelerating

Table 6: Key beam parameters of the klystron-based alternative at the collision point.

Parameter	Symbol	Unit	Stage 1
Centre-of-mass energy	\sqrt{s}	GeV	380
Repetition frequency	f_{rep}	Hz	50
Number of bunches per train	n_b		485
Bunch separation	Δt	ns	0.5
Total luminosity	\mathcal{L}	$10^{34} \text{ cm}^{-2} \text{ s}^{-1}$	1.5
Luminosity above 99% of \sqrt{s}	$\mathcal{L}_{0.01}$	$10^{34} \text{ cm}^{-2} \text{ s}^{-1}$	0.9
Total integrated luminosity per year	\mathcal{L}_{int}	fb^{-1}	180
Number of particles per bunch	N	10^9	3.87
Bunch length	σ_z	μm	60
IP beam size	σ_x/σ_y	nm	119/2.9
Normalised emittance (end of linac)	$\varepsilon_x/\varepsilon_y$	nm	$\leq 630/\leq 20$
Final RMS energy spread		%	0.35
Crossing angle (at IP)		mrad	16.5

structure and pulse compressor in the injection system would be slightly different to obtain optimum efficiency.

The single bunch parameters at the entrance of the linac are very similar to the drive-beam based design. The main difference is the lower bunch charge, which helps the emittance preservation, and the smaller horizontal emittance, which needs to be achieved. Both parameters are very similar to the 380 GeV design and can thus be achieved with the corresponding design. The bunch length at the start of the main linac and afterwards is larger in the klystron-based design, which requires less compression in the RTML and eases the system requirements.

An optimised layout of the main linac has been developed and beam dynamics studies have been performed. They confirmed the expected results that the performance is the same as for the drive-beam case.

The beam delivery system design is the same for the baseline option and the klystron-based alternative, since the beta-functions at the collision point are the same.

3.4 Extension to higher energy stages

The CLIC 380 GeV energy stage can be efficiently upgraded to higher energies, like the proposed 1.5 TeV and 3 TeV stages. This flexibility has been an integral part of the design choices for the first energy stage. The highest energy stage corresponds to the design described in the CLIC CDR [2], with minor modifications due to the first energy stages, as described below. The only important difference to the CDR design is a new final focus system that has an increased distance between the last quadrupole of the BDS and the interaction point. This allows the magnet to be installed in the tunnel and outside of the detector.

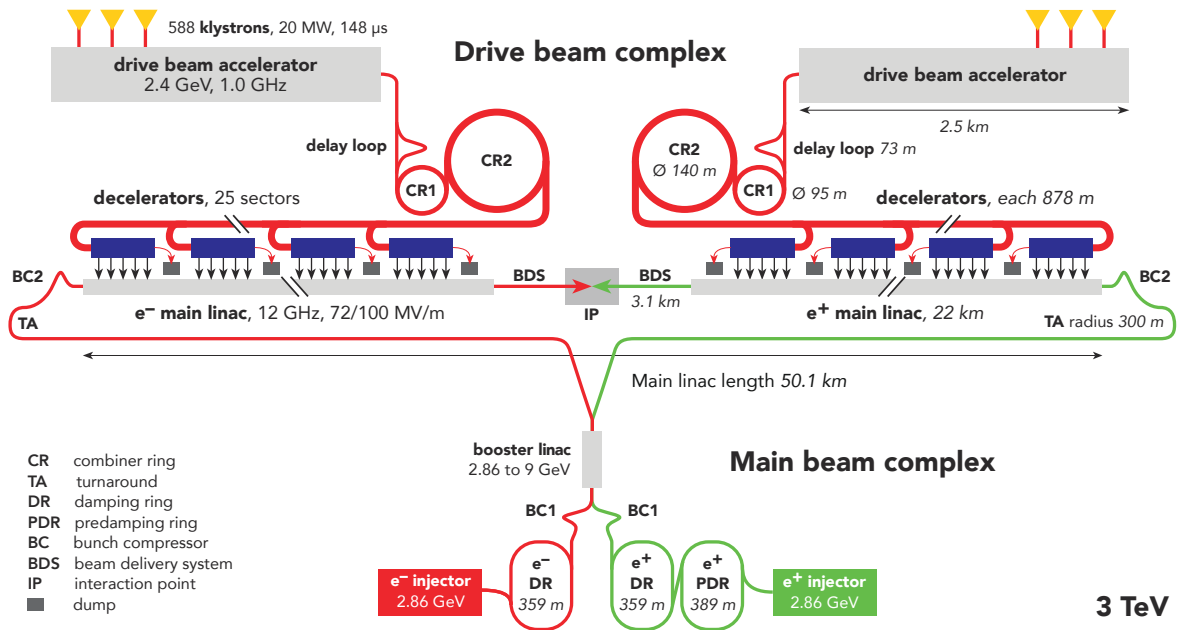


Figure 16: Schematic layout of the CLIC complex at 3 TeV. (image credit: CLIC)

3.4.1 Baseline design upgrade

The key parameters for the different energy stages of CLIC are given in Table 5 and the schematic layout for the 3 TeV stage is shown in Figure 16. The baseline concept of the staging implementation is illustrated in Figure 17. In the first stage, the linac consists of modules that contain accelerating structures that are optimised for this energy. At higher energies these modules are reused and new modules are added to the linac. First, the linac tunnel is extended and a new main-beam turn-around is constructed at its new end. The technical installations in the old turn-around and the subsequent bunch compressor are then moved to this new location. Similarly, the existing main linac installation is moved to the beginning of the new tunnel. Finally, the new modules that are optimised for the new energy are added to the main linac. Their accelerating structures have smaller apertures and can reach a higher gradient of 100 MV/m; the increased wakefield effect is mitigated by the reduced bunch charge and length. The beam delivery system has to be modified by installing magnets that are suited for the higher energy and it will be extended in length. The beam extraction line also has to be modified to accept the larger beam energy but the dump remains untouched. Alternative scenarios exist. In particular one could replace the existing modules with new, higher-gradient ones; however, this would increase the cost of the upgrade. In the following only the baseline is being discussed.

The design of the first stage considers the baseline upgrade scenario from the beginning. For the luminosity target at 380 GeV, the resulting cost increase of the first stage is 50 MCHF compared to the fully optimised first energy stage (without the constraints imposed by a future energy upgrade beyond 380 GeV). To minimise the integrated cost of all stages, the upgrades reuse the main-beam injectors and the drive-beam complex with limited modifications, and reuse all main linac modules.

In order to minimise modifications to the drive-beam complex, the drive-beam current is the same at all energy stages. The existing drive-beam RF units can therefore continue to be used without modification. In addition, the RF pulse length of the first stage is chosen to be the same as in the subsequent energy stages. This is important since the lengths of the delay loop and the combiner rings, as well as the spacings of the turn-around loops in the main linac, are directly proportional to the RF pulse length.

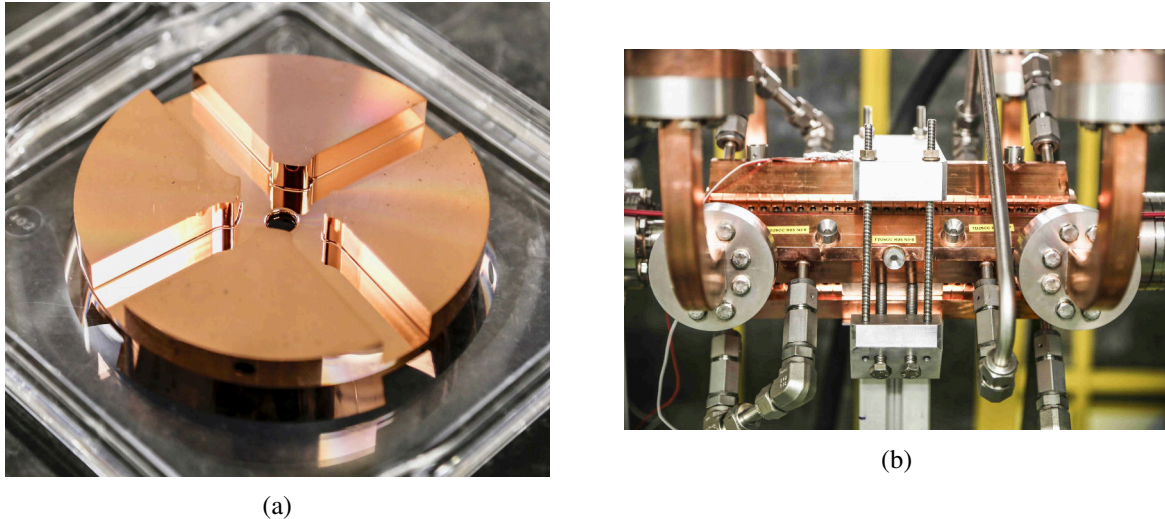


Figure 19: (a) The micron-precision disk which is the basic assembly block of the CLIC accelerating structures. Higher-order mode damping is provided by the four waveguides. (b) A prototype CLIC-G accelerating structure installed for high-gradient test. (image credit: CLIC)

3.5.1 Main linac accelerating structures

The main linac accelerating structures have to accelerate a train of bunches with a gradient of 72 MV/m and a breakdown rate of less than $3 \times 10^{-7} \text{ m}^{-1}$. Damping features suppress higher-order modes, so-called transverse multi-bunch wakefields, to avoid beam emittance growth; this enables high beam current and consequently high RF-to-beam efficiency. Finally, the accelerating structures must be built with micron precision tolerances and be equipped with special beam position monitors, so-called wake monitors, in order to limit single-bunch emittance growth.

The overall optimisation of CLIC has been carried out following the insights from in-depth studies of the different aspects of the accelerating structure behaviour. This optimisation has allowed the main parameters of the accelerating structure to be determined, the detailed design to be made, and prototypes to be constructed and validated in both high-power and beam-based tests.

CLIC accelerating structures are travelling wave with a tapered inner aperture diameter ranging from 8.2 mm down to 5.2 mm, and are approximately 25 cm in length. They are made from copper and operate at 12 GHz. They are assembled from micron-precision disks that are bonded together. Higher-order-mode suppression is provided by a combination of heavy damping, which is accomplished through four short terminated waveguides connected to each cell, and detuning accomplished through the iris aperture tapering. Photographs of the basic component disk, an assembled test prototype accelerating structure and a drawing of a full double structure assembly are shown in [Figures 19](#) and [20](#).

The different performance aspects have been validated in a series of dedicated tests. The most resource intensive has been high-gradient testing. The objective of these tests is to understand and determine high-field limits and to operate prototype accelerating structures for extended periods. These tests have been carried out in dedicated test stands, both at CERN and at KEK, which use klystron RF power sources in a configuration similar to the klystron-based version of CLIC. The tests involve conditioning the structures; that is, increasing the field level gradually to the nominal level, then operating them for extended periods at low breakdown rate. Over a dozen prototype 3 TeV accelerating structures, the so-called CLIC-G design, have been tested and a summary is shown in [Figure 21](#). The 380 GeV initial energy stage of CLIC requires a lower loaded accelerating gradient, 72 MV/m, than the 3 TeV stage. However, the iris aperture must be larger. The structures optimised for 380 GeV incorporate

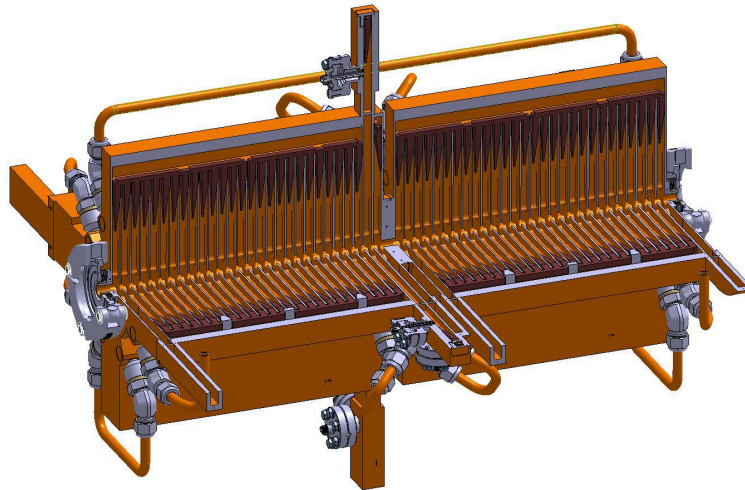


Figure 20: Assembly drawing of the double-structure acceleration unit. (image credit: CLIC)

improvements understood from the high-gradient testing carried out up until now. They are currently in advanced stages of fabrication and will be tested soon.

In addition to these tests, an experiment to determine the effect of the heavy beam loading has been carried out using the CTF3 drive-beam injector beam. This experiment confirmed expectations of the effect and validated the design choices. Finally, the higher-order-mode suppression has been directly validated with beam in the FACET facility at SLAC [65].

The accelerating structures represent an important contribution to the overall cost of CLIC and consequently costing and cost reduction are under active study. The micron tolerances as well as complexity related to the waveguide couplers and damping waveguide manifolds are the main cost drivers. Although the main focus of the prototypes described above has been high-gradient testing, important insights have been made on precision assembly and cost. More precise and lower cost alternatives based on these insights are now under design and fabrication.

3.5.2 RF power generation and distribution

Increasing the efficiency of the currently available klystrons is essential for CLIC, both for the two-beam and klystron-based CLIC options. For the drive-beam generation complex, two high-efficiency klystron prototypes in L-band technology have been developed in collaboration with industry, with the goal to obtain an efficiency above 70%. The first prototype, using a 6-beam Multi-Beam Klystron (MBK), reached 21 MW output power during the factory tests. Its efficiency of 71.5% remains remarkable high for a wide range of output power. A second prototype built by another firm, based on a 10-beam MBK, also reached the required peak power and an efficiency of 73%. However, it does not yet fulfil the requirements concerning stability and average power. Extensive testing of both prototypes continues [67].

Modulator requirements for the drive beam were found to be in an unexplored range, where specifications of fast pulse modulators (fast voltage rise and fall times to minimise power losses) and long pulse modulators (long voltage flat-top) have to be merged. The design effort for a suitable klystron-modulator topology has taken the high power electrical distribution over a ~ 2 km long drive beam into account. The solution found in this global optimisation imposes a modulator topology with a medium voltage DC stage and a voltage step-up pulse transformer [67]. Series and parallel redundancies have

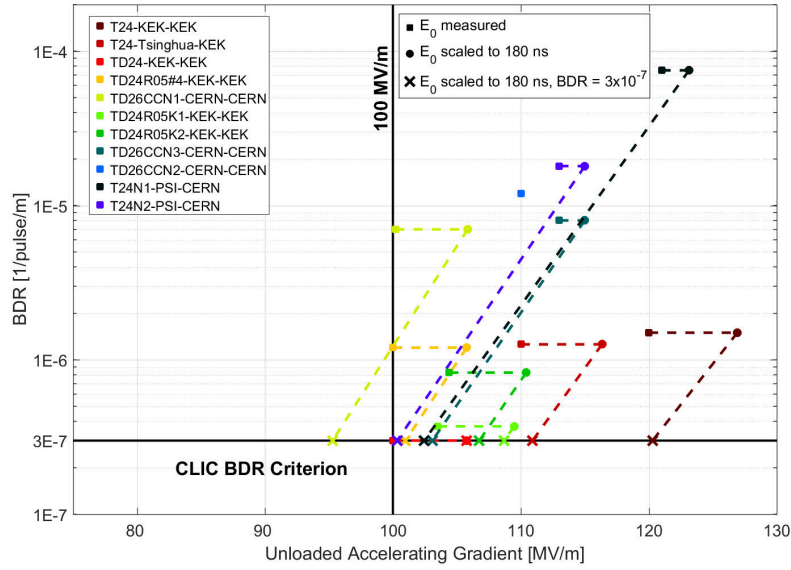


Figure 21: A summary of achieved performances of 3 TeV acceleration structures in tests. The vertical axis represents the breakdown rate per metre (BDR). The final operating conditions of the tests are indicated by squares. Known scaling is used to determine the performance for the nominal CLIC pulse duration (dashed lines connecting squares to circles) and subsequently for the CLIC-specified breakdown rate of $3 \times 10^{-7} \text{ m}^{-1}$ (dashed lines connecting circles to crosses). (image credit: CLIC)

been studied and small scale prototypes have been designed and built. A full scale modulator prototype based on parallel redundancy topology has been designed and delivered to CERN from ETH Zürich. First tests on an electrical dummy load demonstrated the feasibility of the voltage pulse dynamics up to 180 kV. This modulator represents the new state of the art in fast pulsed modulators with flat-top and medium voltage input.

For a klystron powered machine at 380 GeV, each X-band klystron will provide a peak RF power of 50 MW with a pulse width of $1.6 \mu\text{s}$ and a pulse repetition rate of 50 Hz at a frequency of 11.9942 GHz. These parameters are achievable using technology already available from industry [68], as demonstrated in the operation of the X-band test facilities at CERN [69]. As in the case of the L-band klystrons, and in collaboration with industry, a study is ongoing to improve the existing design of the klystron to achieve an efficiency of 70% while maintaining the required peak power [70]. Additionally, a study to replace the normal-conducting solenoid in the klystron with a superconducting solenoid is ongoing in collaboration with KEK.

The PETS are passive microwave devices that interact with the drive beam to generate RF power for two accelerating structures. The power is collected and extracted at the downstream end, where a remotely controlled mechanism allows adjustment of the RF power that flows into the accelerating structures. This flexibility allows sparking structures to be effectively switched off and also allows the structures in the main linac to be conditioned in parallel, each pair at their individual performance level. The PETS also contain damping waveguides that are equipped with loads and avoid beam instabilities. A total of sixteen PETS have been manufactured and tested in the two beam line of CTF3.

The RF power source for the main linac is connected to the accelerating structure through a network of waveguides that must transport RF power in excess of 100 MW with as little attenuation as

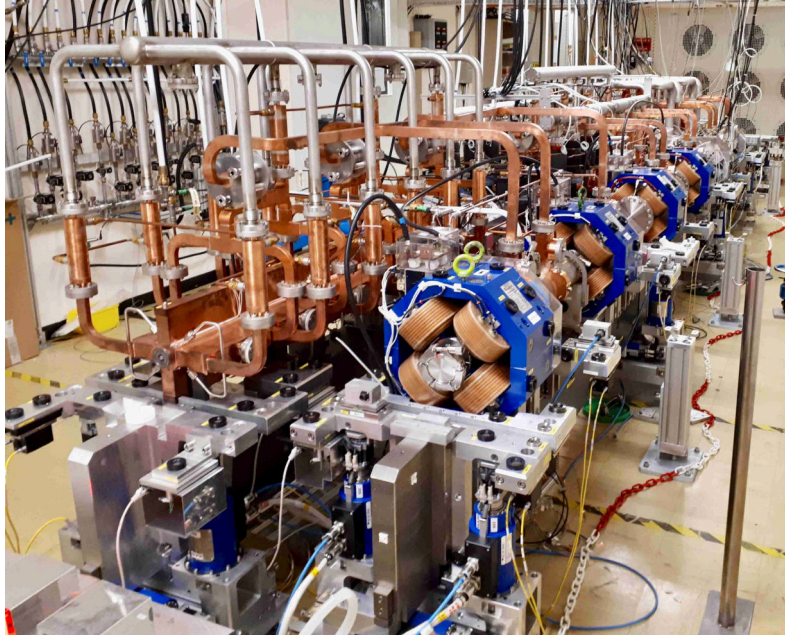


Figure 22: Two-beam module string used for alignment, thermomechanical stability and vacuum tests. The drive beam can be seen on the right, the main beam on the left. (image credit: CLIC)

possible. It controls the power produced in the PETS for the two-beam option or shapes the pulses from the klystron-modulator unit. The network distributes power among multiple accelerating structures, provides diagnostics and allows independent movement of the accelerating structure and power source.

Fully equipped two-beam modules have been tested in a dedicated facilities with and without beam at CERN (see [Figure 22](#)). Results obtained concerning alignment, vibrations, thermal stresses etc. have been fed back into the design of the next generation of modules.

All of the necessary elements for the wave guide system (over-moded low loss transmission lines, mode converters, hybrids, pulse compressors, active phase shifters and power splitters, bends, direction couplers and loads) have been designed, fabricated and operated to full specifications, in the two-beam test stand and the X-band test facility at CERN. [Figure 23](#) shows some examples of recently produced components needed in the waveguide systems. Although the waveguide network is not as technically challenging as the power source and accelerating structures, it represents an important cost element. Continuous efforts are being made to simplify the fabrication and assembly and reduce the cost [71].

3.5.3 Alignment and stabilisation

In order to preserve the luminosity, the total error budget allocated to the absolute positioning of the major accelerator components is 10–20 μm . For comparison, 100–500 μm are sufficient for LHC and HL-LHC.

The first ingredient of the CLIC alignment system is the Metrological Reference Network (MRN). Simulations have been carried out for the CLIC MRN [72], considering stretched reference wires with a length of 200 m and an accuracy of alignment sensors of 5 μm . Simulations showed that the standard deviation of the position of each component with respect to a straight line was included in a cylinder with a radius smaller than 7 μm . This was confirmed experimentally in a 140 m long test facility. In order to achieve this accuracy, the sensors and active elements themselves were re-engineered in some

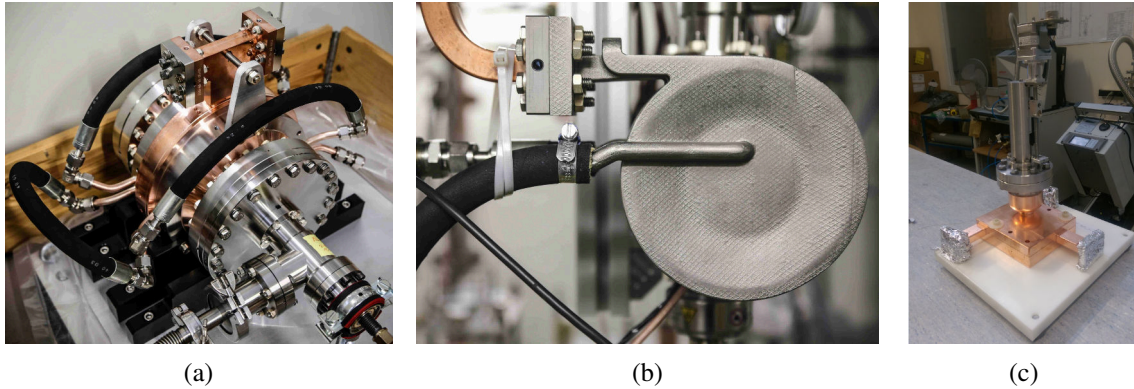


Figure 23: Components used in the waveguide system: (a) Barrel Open Cavity (BOC) pulse compressor (designed and manufactured by PSI), (b) compact 3D printed load and (c) variable power splitter. (image credit: CLIC)

cases. The performance of the capacitive Wire Positioning Systems and Hydrostatic Levelling Sensors was measured in the laboratory. Asymmetric cam movers with sub-micron displacement resolution have also been developed.

For the fiducialisation and alignment of each element on the common 2-beam module support, a new strategy has been proposed, based on results obtained in the PACMAN project [73, 74] and on the development of an adjustment platform with five degrees of freedom [75]. This strategy is based on individual determination of the axes of each component using metrological methods and a stretched wire. The absolute position of the wire can be measured to very high precision using a Coordinate Measuring Machine or a portable Frequency Scanning Interferometry system.

However, in order to maintain all the benefits of this very accurate alignment along the accelerator, absolute displacements of system elements caused by ground motion or vibrations during operation need to be avoided. As a first approximation, the integrated RMS displacement above a frequency of 1 Hz must stay below 1.5 nm in the vertical direction and below 5 nm in the horizontal direction for all main-beam quadrupoles (MBQ). For the final focus magnets, the integrated displacement above 4 Hz shall remain below 0.14 nm in the vertical plane. Besides an adapted civil engineering and a very careful design of the supporting systems of all the elements in the accelerator, an active vibration stabilisation system is required for all MBQ magnets along the main linac. Active stabilisation is based on a stiff support and piezo actuators that can reposition the magnet during the 20 ms between pulses with high accuracy. Five prototypes have been built with increasing complexity, mass and degrees of freedom. The fourth prototype reached the requirements for the main linac for a higher vibration background and for a nominal magnetic field and water-cooling. The last prototype (Figure 24) is a complete, fully integrated stabilisation system with an MBQ. Tests in the laboratory are in preparation. Most equipment used is commercially available, while the in-house developed components are technologically well within reach. Tests of a full system in a radiation environment are still outstanding.

Recent beam dynamics studies indicate that the shape of the transmissibility function is more important for the luminosity than the obtained integrated RMS displacement. This implies that a single combined control system, simultaneously taking measurements of ground motion and technical noise into account, is needed for the beam and for the stabilisation of the hardware. This understanding has triggered the development of adapted ground motion sensors for the stabilisation.

Indeed, commercial sensors including inertial sensors, geophones or broadband accelerometers, have two main limitations: they are not radiation hard and need to be re-designed to be integrated in a vibration control system. CERN is collaborating with LAPP Annecy on the development of new

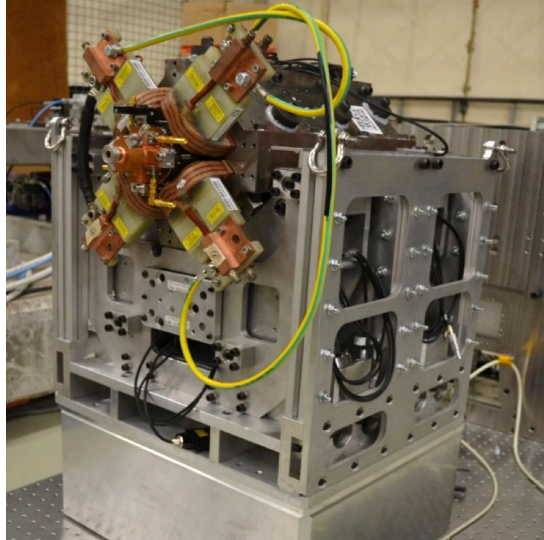


Figure 24: Main-beam quadrupole active stabilisation prototype. (image credit: CLIC)

sensors, based on new or combined methods, such as transducers, optical encoders, one-pass or multi-pass interferometers [76, 77] to measure the internal mass motion. At the same time, ULB Brussels is studying the replacement of the classical spring mass by an internal beam [78, 79].

3.5.4 Beam instrumentation

In order to preserve low emittance beams over long distances, dispersion free-steering needs to be applied along the CLIC main linac. It relies on the use of cavity Beam Position Monitors (BPM) capable of achieving a few tens of nanometre precision in space, combined with a time resolution better than 50 ns. A low-Q cavity BPM for the CLIC main beam was constructed and tested at CTF3. Its ability to measure the beam position for a 200 ns long train of bunches with a time accuracy better than 20 ns was demonstrated [80].

CLIC relies also on colliding electron and positron bunches as short as 150 fs. The bunch length needs to be measured and controlled accurately with time resolution better than 20 fs. An R&D programme was launched in 2009 to design and test non-invasive bunch length monitors using laser pulses and bi-refringent Electro-Optical (EO) crystals [81, 82]. Based on such a technology, a new scheme, called Spectral Up-conversion, has been developed [83]. It directly measures the Fourier spectrum of the bunch using an optical spectrum imaging system, as the beam fields are printed onto a laser beam and up-converted from the far-IR-mid-IR spectrum to the optical region. The technique uses a long-pulse laser probe, transported through an optical fibre. This makes the system simpler and cheaper than the ultra-fast amplified systems of other EO schemes.

A breakthrough in beam size monitoring was achieved in 2011, with the experimental measurement in ATF2 at KEK of the point-spread function of optical transition radiation, that allows for sub-micron resolution measurements using a simple, cheap and compact optical imaging system [84]. In addition, Cherenkov diffraction radiation from long dielectrics has recently been tested at Cornell Electron Storage Ring (CESR) and ATF2 as an alternative to diffraction radiation from a small slit. It provides a very promising technique for non-invasive beam size measurements.

A high-performance and cost-efficient Beam Loss Monitor (BLM) system, based on optical fibre measuring Cherenkov light induced by lost charged particles, has been developed to monitor losses in the drive-beam decelerator sections [85]. In particular, the study has addressed several key features of

the BLM system such as the position resolution of the optical fibre detection system when using long electron pulses (i.e. 200 ns) [86], and the crosstalk between losses from the main beam and the drive beam [87].

3.5.5 Vacuum system

The original baseline for the vacuum system for the main linac, with long vacuum chambers providing pumping to several modules, was demonstrated in the laboratory module from the point of view of pumping performance. However, transverse forces from the vacuum system on the main-beam and drive-beam structure generated displacements which are not compatible with the CLIC requirements. Therefore, the current architecture of the vacuum system is based on a combination of Non-Evaporable Getters (NEG) cartridge pumps combined with sputter ion pumps (100 L s^{-1} and 5 L s^{-1} , respectively) and NEG cartridge pumps (100 L s^{-1}). A set of Pirani and Penning gauges are installed on each beam line and in each module to complete the system [88].

Technology originally proposed for the CLIC drive beam, e.g. a deformable RF bridge [89], is now being implemented for LHC and HL-LHC. On the other hand, new vacuum technologies currently under development are considered for application at CLIC. Examples are the NEG-coated electroformed copper chambers [90], permanent radiation-hard bake out systems, and Shape Memory Alloy connectors (see Figure 25) [91, 92].

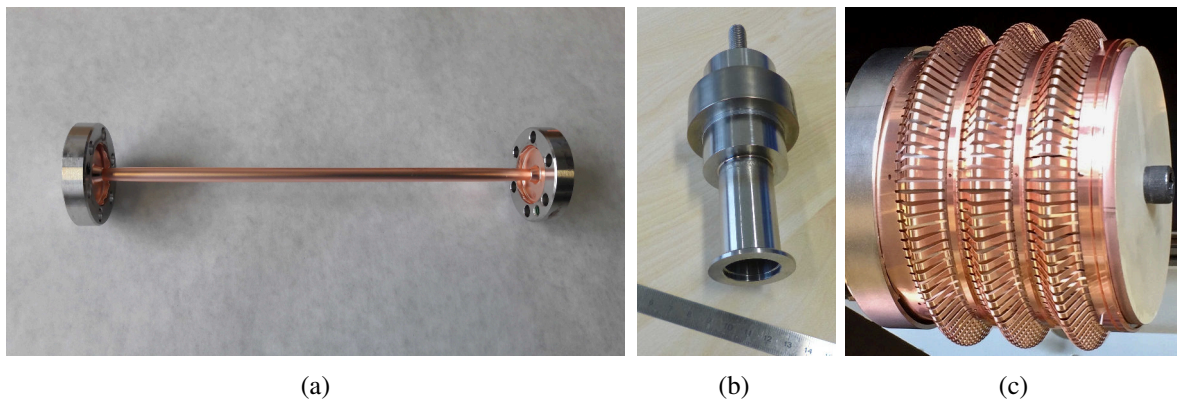


Figure 25: Examples of CLIC vacuum system components using new technologies: (a) electroformed copper chamber integrating stainless steel flanges, (b) ultrahigh vacuum coaxial Shape Memory Alloy connector and (c) deformable RF bridge. (image credit: CLIC)

3.5.6 Magnets

Most of the magnets required for CLIC are normal-conducting electromagnets, well within the state of the art. However, their number and variety are well beyond current accelerator projects. For this reason, a significant effort has been invested in optimising the fabrication, assembly, and installation procedures. A total of 15 prototype electro-magnets have been manufactured and tested to verify the design choices, with system tests at CTF3 and in the laboratory. Given the large number of magnets in the CLIC complex, it is important to minimise costs and power consumption. Tuneable Permanent Magnets (PM) have been designed and manufactured for the quadrupoles in the main decelerator, in collaboration with the Daresbury laboratory [93]. The design has been optimised for cost and industrialisation. The feasibility of the concept is now proven but studies on the radiation effects on the PM material are still needed before re-evaluating the baseline [94, 95]. Prototypes of the final quadrupole and sextupole, QD0

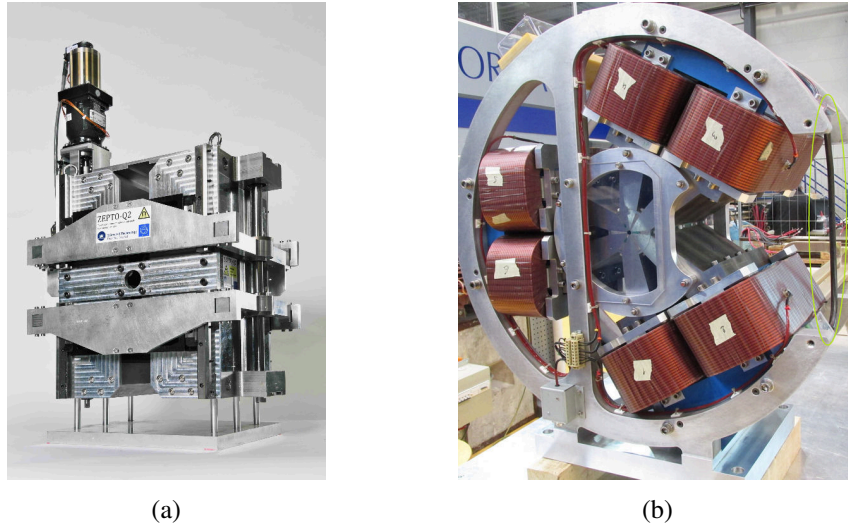


Figure 26: Prototypes of magnets for CLIC: (a) the tuneable permanent magnet quadrupole for the drive beam and (b) the hybrid SDO final sextupole. (image credit: CLIC)

and SDO, have been manufactured using a hybrid technology (permanent magnets and electro-magnets) to increase the field with a reduced imprint. [Figure 26](#) shows examples of recently built prototypes.

A special magnet, designed and currently being manufactured by CIEMAT, is the so-called longitudinal variable field magnet. This type of magnet will allow for a reduction in the total circumference of the damping ring of 13%, while preserving performance. The concept is being applied to the upgrade of light sources such as ESRF. However, the CLIC prototype is more challenging, as it is a tuneable permanent magnet combining dipole and quadrupole components, with a very high field of 2.3 T at its centre.

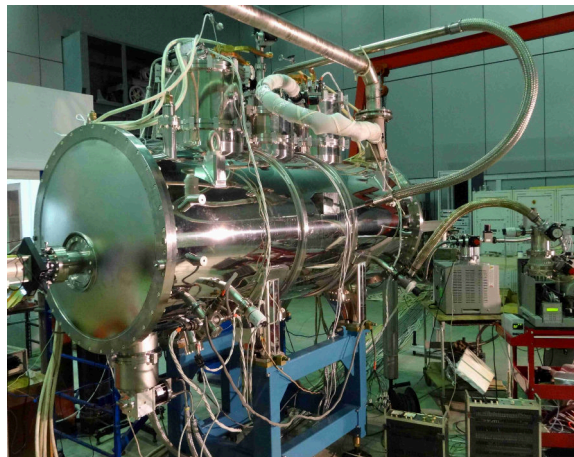


Figure 27: Superconducting wiggler being tested in BINP. (image credit: CLIC)

The damping rings will contain a number of wigglers in each straight section to increase radiation damping and reduce the Intrabeam Scattering (IBS) effect, thereby reaching an emittance which is at least an order of magnitude lower compared to planned or existing rings. This is achievable by using superconducting wigglers. A Nb-Ti prototype (see [Figure 27](#)) was manufactured by Budker Institute of Nuclear Physics in collaboration with CERN and the Karlsruhe Institute of Technology, where it is

currently installed [96]. The prototype magnet was used to validate the technical design of the wiggler, in particular the conduction-cooling concept applied in its cryostat design. As part of the study, the expected heat load (several tens of Watt) due to synchrotron radiation from a future up-stream wiggler is simulated by heating the vacuum pipe with an electrical heater. A short model using Nb_3Sn , which will be able to reach a higher field and further reduce the damping ring circumference was also designed and manufactured. Further improvements on this prototype are under way.

Concerning pulsed magnets, the most challenging requirements come from the damping rings and the very high field uniformity and time stability required to extract the electron beam without deteriorating the final luminosity. The combined flat-top ripple and drop of the field pulse must be $\pm 2 \times 10^{-4}$. In addition, the total allowable beam coupling impedance for each ring must be below 1Ω . The damping ring extraction uses a strip-line kicker specifically designed for the CLIC characteristics. It is equipped with electrodes with a novel shape, called half-moon electrodes. The electrode support, feedthroughs and manufacturing tolerances have been optimised to match the impedance during operation and to minimise the field inhomogeneity [97, 98]. A prototype of this kicker, shown in Figure 28(a), has been manufactured in a collaboration between CERN, CIEMAT and IFIC in Spain [99].

To power the strip-line kicker, an inductive adder (see Figure 28(b)) has been selected as a promising means of achieving the demanding specifications for the extraction kicker modulator of the damping ring. The inductive adder is a solid-state modulator, which can provide relatively short and precise pulses. The adder is assembled in layers each of which contributes linearly to the final voltage. Detailed research and development has been carried out on this device, which has the potential to be used also in other accelerators. Recent measurements on the prototype inductive adder show that the flat-top stability achieved by applying modulation was $\pm 2.2 \text{ V}$ over 900 ns at 10.2 kV output voltage. This pulse meets the stability specifications for the damping ring extraction kicker [100].

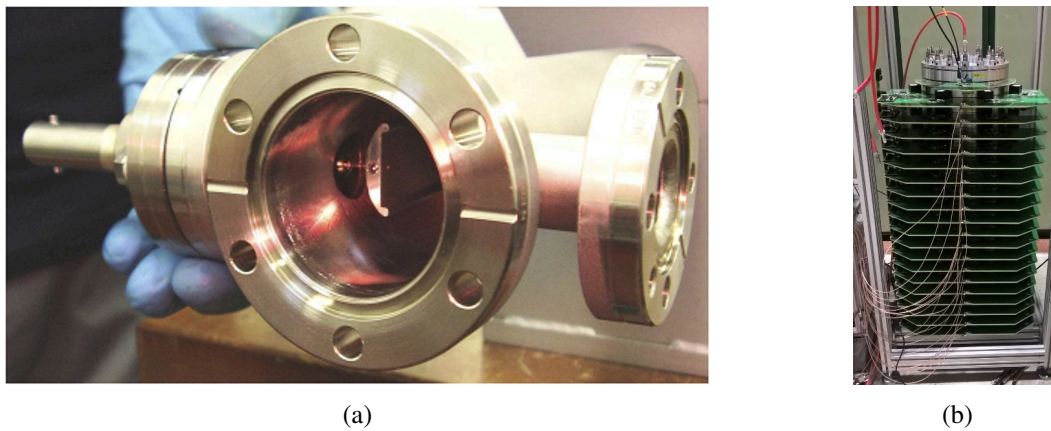


Figure 28: (a) Prototype strip-line kicker with optimised half-moon electrodes. (b) 20-layers inductive adder. (image credit: CLIC)

In order to complete its characterisation, the prototype strip-line kicker has been installed in the ALBA synchrotron to be tested with beam. A first measurement indicates that the field homogeneity is within the desired range ($\pm 1 \times 10^{-4}$) although the measurement error is still too large to quote definitive results. In order to confirm the stability of the full system, the inductive adder will be also sent to ALBA and tested together with the strip-line kicker.

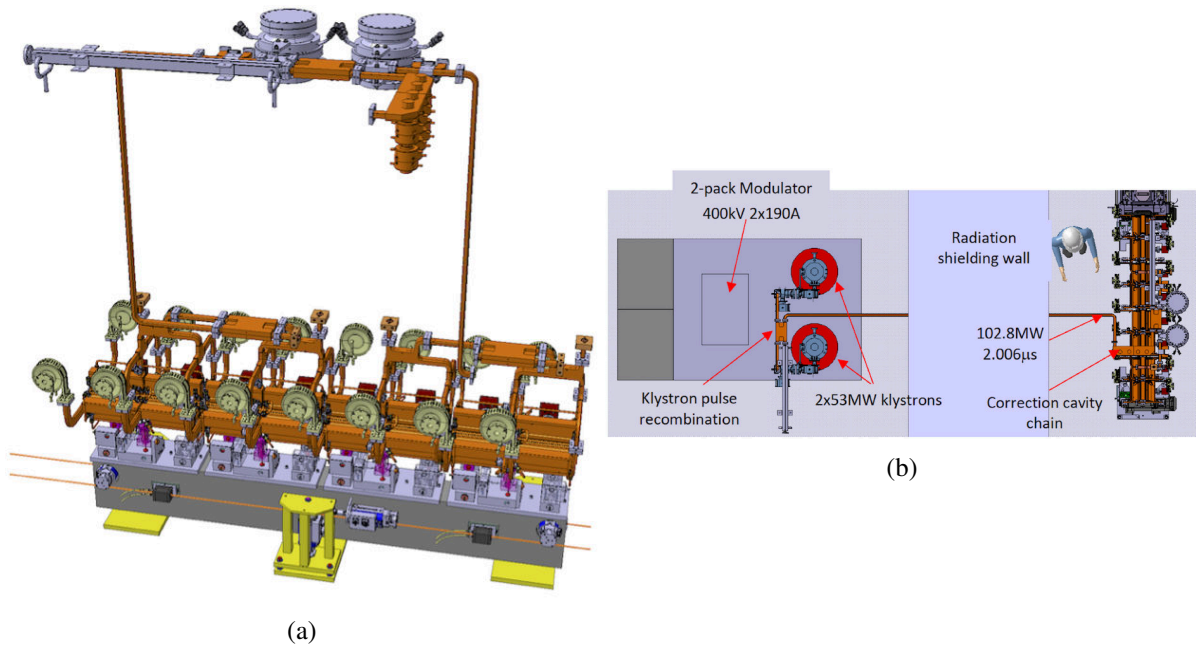


Figure 29: (a) The klystron-based module with pulse compression and linearisation system. (b) Top view of one RF unit in the Klystron and Main Linac tunnels. (image credit: CLIC)

3.5.7 Klystron-based main linac RF unit and module design

Each main linac consists of a sequence of 1456 identical RF modules that are interleaved with quadrupole modules to form the FODO lattice. The RF module supports four pairs of accelerating structures, each with an active length of 0.46 m and a gradient of 75 MV/m.

The RF power system per module consists of a two-pack solid-state modulator equipped with two 53 MW klystrons. Two pulse compressor systems, which are equipped with linearising cavities, compress the $2.0006\ \mu\text{s}$ -long RF pulses of the klystrons to 334 ns. The pulse is then distributed into the accelerating structures. In [Figure 29](#) a klystron-based module is shown on the left, equipped with linearisation and pulse compression cavities. On the right a top view of one RF unit in the Klystron and Main Linac tunnels. High efficiency klystrons are considered in this scheme [101], operating with an efficiency in excess of 60%; the pulse compression device adopts Barrel Open Cavities providing a compression factor of 3.5 and delivering 170 MW RF power at their output to feed each of the four accelerating structures with 40.6 MW.

4 CLIC detector design, technologies and performance

The CLIC detector layout and its technology choices are driven by the CLIC physics programme described in [Section 2](#), and by the experimental conditions at CLIC described in [Section 4.1](#). The resulting detector concept is described in [Section 4.3](#). Details on the technology choices under investigation for the CLIC detector concept are given in [Section 4.4](#) and the detector concept performance is detailed in [Section 4.5](#).

4.1 Experimental conditions at CLIC

The experimental conditions at CLIC are given by the CLIC beam structure, the presence of beam-induced backgrounds, the low-rate environment in the e^+e^- collisions, and the beam particle energy spectrum at collision.

Beam structure Linear colliders operate in bunch trains. For example, at 380 GeV, CLIC has a train repetition rate of 50 Hz with 352 bunches per train, each separated by 0.5 ns, resulting in a train duration of 176 ns. One hard physics event is expected on average per bunch train. Beam-induced background events (described in detail below) giving significant energy deposits in the detector, can take place in several bunch crossings per train. The rates of physics and beam-induced background events, combined with the bunch separation, drive the timing requirements of the sub-detectors. Full detector simulation studies were performed with a CLIC detector concept optimised to achieve low occupancies. It was found that a hit time resolution of ~ 5 ns is needed in the vertex and tracking detectors, and 1 ns in the central calorimeters in order to sufficiently distinguish between energy deposits from hard physics events and those from beam-induced backgrounds.

The 50 Hz repetition rate and short bunch-train structure result in a low duty cycle, below 0.001% for all CLIC energy stages. This offers the possibility of power pulsing the detector's front-end electronics, which leads to a reduced power consumption and consequent reduction in the cooling infrastructure of the sub-detectors. This for instance results in a lower material budget for the vertex and tracking systems, which is of particular importance for the physics performance of the detector. Triggerless readout of the CLIC detector is foreseen at the end of each bunch train.

Beam-induced backgrounds In order to achieve high luminosities at CLIC, extremely small beam sizes and high bunch charges are required. As an example, the transverse beam size at 380 GeV is about $150 \text{ nm} \times 3 \text{ nm}$ in the horizontal and vertical direction, the bunch length is $70 \mu\text{m}$, and one bunch contains 5.2×10^9 particles, as shown in [Table 5](#). This leads to very high electromagnetic fields in the collision region that cause beam–beam interactions, leading to beam-induced background. While most of these particles are produced at very small angles, some enter the detector region. The two processes that produce significant fluxes of particles relevant for the CLIC detector design are incoherent e^+e^- pairs and $\gamma\gamma \rightarrow \text{hadron}$ events [[102](#)]. The energy and polar angle distributions of the particles produced in these processes are shown in [Figure 30](#) for a centre-of-mass energy of 3 TeV. The detector occupancies caused by these background processes have an impact on the detector design choices, such as the diameter of the central beam pipe (thus the radius of the innermost vertex detector layer) and on the sub-detector granularity.

The design effort for the CLIC detector has so far mainly focused on the 3 TeV case. The number of $\gamma\gamma \rightarrow \text{hadron}$ events produced is reduced by a factor of almost 20 at 380 GeV, the incoherent e^+e^- pairs are reduced by a factor of 5 [[12](#)]. Therefore, a detector layout with a smaller vacuum pipe and lower inner radius of the vertex detector barrel is being prepared for the first stage of CLIC operation.

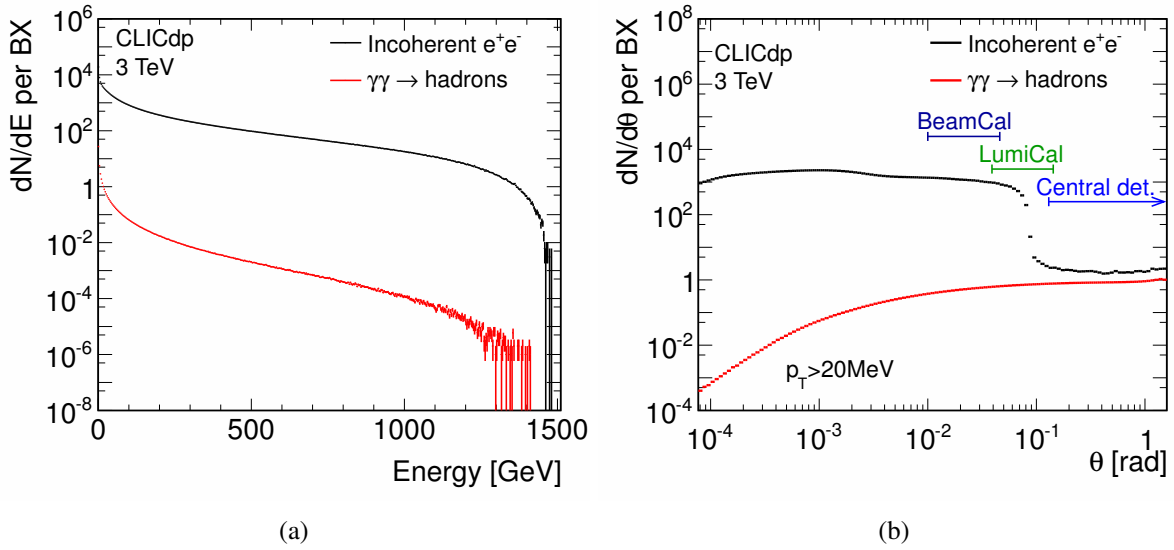


Figure 30: (a) Energy distribution and (b) polar angle distribution per bunch crossing (BX) of beam-induced backgrounds. Both figures are for CLIC at 3 TeV. Generated particle distributions for $p_T > 20$ MeV are shown, including a 2 GeV c.m. threshold for $\gamma\gamma \rightarrow$ hadrons. (image credit: CLICdp)

Clean environment in e^+e^- collisions In hadron collisions such as at the LHC, large QCD backgrounds drive the design of the collider detectors. The design and technology choices emphasise radiation hardness of many sub-detectors as well as complex trigger schemes. In spite of the beam-induced backgrounds described above, e^+e^- collisions provide a much cleaner environment than hadron collisions, such that radiation damage considerations are relevant only for the design of the very forward calorimeters. Also, at linear e^+e^- colliders, there is no need for triggers. This is possible due to the clean events, the low duty cycle, and the relatively low events rates described above.

An upper limit of the data volume per train and the data rate written to tape was estimated for the full CLIC detector including zero suppression and address encoding. The data volume per bunch train ranges from 75 MB at 380 GeV to 115 MB at 3 TeV. With a bunch-train repetition rate of 50 Hz, this results into data rates ranging from 4 GB/s at 380 GeV to 6 GB/s at 3 TeV [13]. These numbers are mainly driven by the beam-induced backgrounds.

Collision energy and energy spread Due to beamstrahlung at the interaction point, a fraction of the incoming e^\pm energy can be lost before the collision takes place leading to a reduction of the e^+e^- collision energy. Due to the beamstrahlung photons, $e^\pm\gamma$ and $\gamma\gamma$ collisions can also take place. The resulting luminosity spectra for e^+e^- , $e^\pm\gamma$ and $\gamma\gamma$ collisions at two different CLIC centre-of-mass energies are illustrated in Figure 31. The effects caused by beamstrahlung increase with centre-of-mass energy. Initial State Radiation (ISR) creates an additional energy loss, which reduces further the collision energy.

Suppression of beam-induced backgrounds Particles from beam-induced backgrounds entering the central detector region have relatively low transverse momenta. By applying p_T cuts on the reconstructed objects during physics analyses, the impact of beam-induced backgrounds can be reduced. Beam-induced background can be further suppressed by making use of the hit time resolution of the different sub-detectors. When combining hit timing information into cluster timing of the reconstructed particles, even tighter timing cuts can be applied. Combined p_T and timing cuts optimised for the dif-

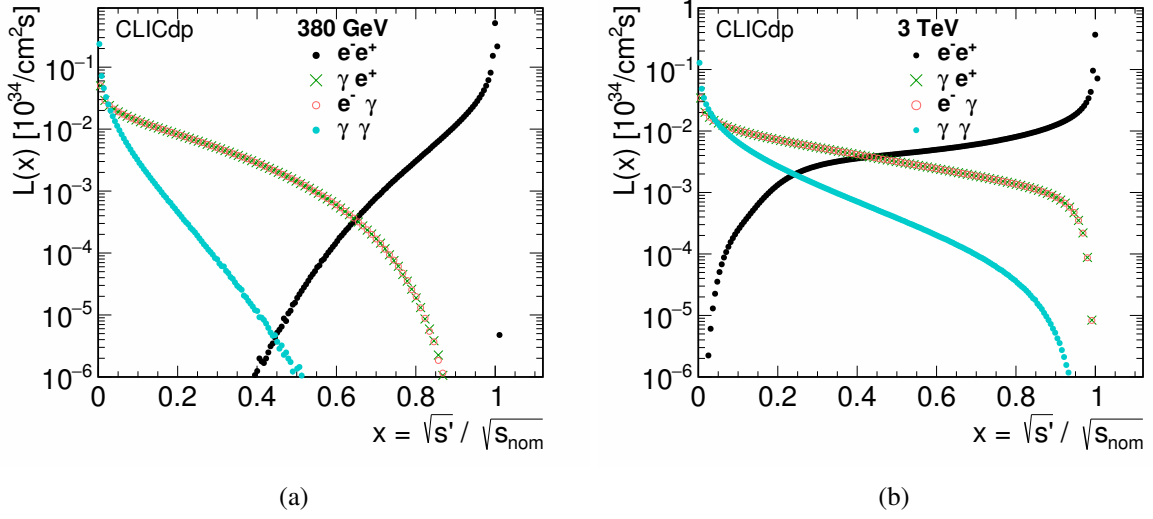


Figure 31: Luminosity distributions for different types of collisions, (a) at $\sqrt{s_{\text{nom}}} = 380 \text{ GeV}$ and (b) at $\sqrt{s_{\text{nom}}} = 3 \text{ TeV}$ [12].

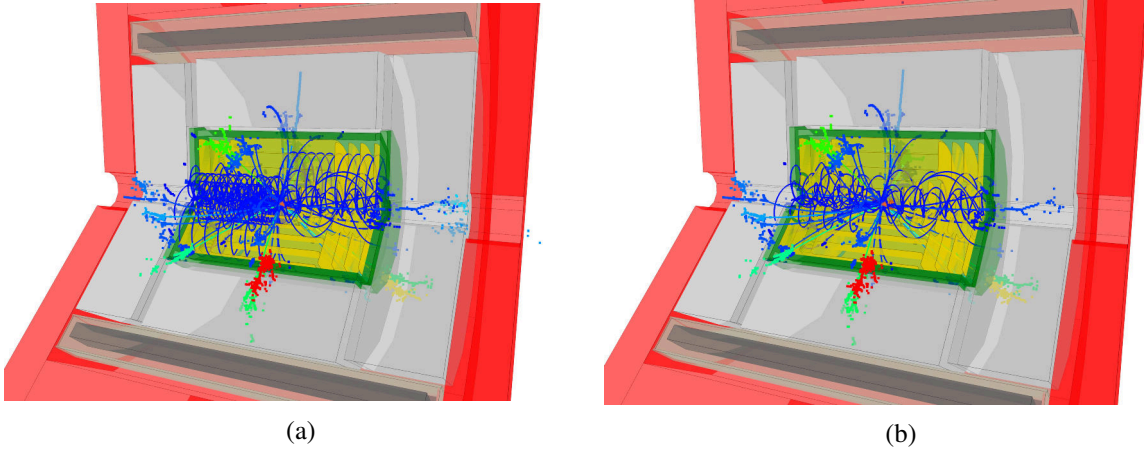


Figure 32: Event displays of $e^+e^- \rightarrow t\bar{t}$ events at a centre-of-mass energy of 380 GeV (a) before, and (b) after background suppression using *Loose* p_T and timing cuts (image credit: CLICdp)

ferent detector regions are described in [3, 103]. The tightness of the cuts, called *Loose*, *Selected*, and *Tight*, can be adjusted to the event type under study and the centre-of-mass energy. For centre-of-mass energies of 380 GeV and below, a special set of *low energy Loose* cuts has been introduced.

For example, when considering $e^+e^- \rightarrow t\bar{t}$ events at $\sqrt{s} = 380 \text{ GeV}$, the average reconstructed energy is 370 GeV. This is reduced slightly by the *Loose* or *Tight* timing cuts to 366 GeV or 357 GeV, respectively, corresponding to 98.9% and 96.5% of the initial value. At the same time, the average reconstructed energy of the $\gamma\gamma \rightarrow \text{hadrons}$ background, which is initially 45 GeV, is reduced to 28 GeV or 62.2% with the *Loose* cuts and 8 GeV or 17.8% with the *Tight* cuts [103].

Figures 32 and 33 show the impact of such combined p_T and timing cuts for typical $e^+e^- \rightarrow t\bar{t}$ events at centre-of-mass energies of 380 GeV and 3 TeV. Displayed are the reconstructed objects originating from the hard physics collision and from the $\gamma\gamma \rightarrow \text{hadrons}$ interactions of 10 bunch crossings before and 20 bunch crossings after the hard event.

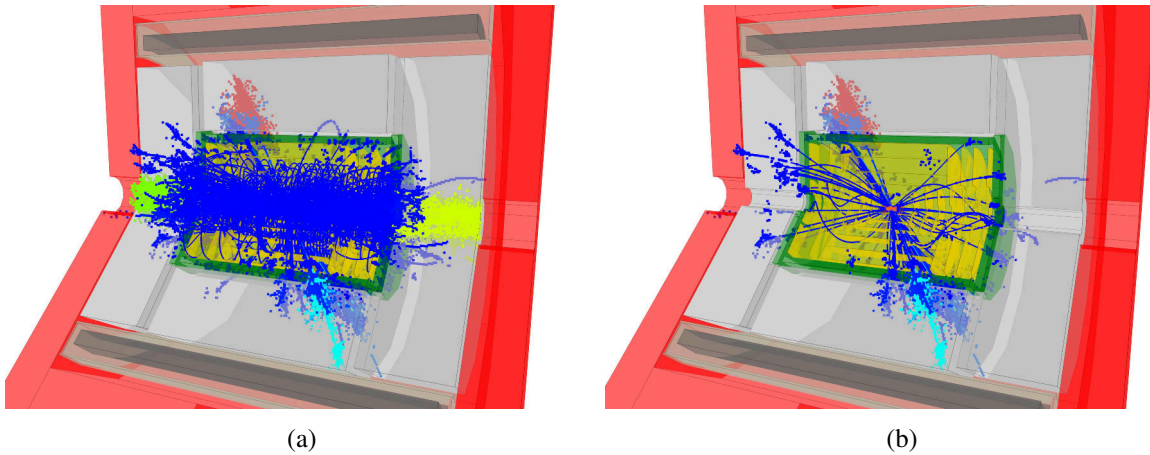


Figure 33: Event displays of $e^+e^- \rightarrow t\bar{t}$ events at a centre-of-mass energy of 3 TeV (a) before, and (b) after background suppression using *Tight* p_T and timing cuts. (image credit: CLICdp)

4.2 Physics-driven detector requirements

Besides being compatible with the CLIC operation conditions described above, the CLIC detector also needs to meet the physics performance targets. Motivated by precision physics measurements described in [Section 2](#), the targets used for the development of the CLIC detector are:

- excellent track-momentum resolution for high-momentum tracks in the barrel, at the level of $\sigma_{p_T}/p_T^2 \leq 2 \times 10^{-5} \text{ GeV}^{-1}$;
- precise impact-parameter resolution, at the level of $\sigma_{d_0}^2 = (5\mu\text{m})^2 + (15\mu\text{m GeV})^2/(p^2 \sin^3 \theta)$, to allow accurate reconstruction and enable flavour tagging with clean b-, c-, and light-quark jet separation;
- jet-energy resolution for light-quark jets of $\sigma_E/E \leq 3.5\%$ for jet energies in the range 100 GeV to 1 TeV ($\leq 5\%$ at 50 GeV);
- detector coverage for electrons and photons to very low polar angles ($\sim 10\text{mrad}$) to assist with background rejection.

4.3 CLIC detector concept

The CLIC detector concept, referred to hereafter as CLICdet, is optimised for particle flow analysis. It comprises a light-weight silicon-pixel vertex detector with a central barrel and forward petals in a spiral arrangement optimised for air cooling, a light-weight silicon tracker, and highly-granular electromagnetic (silicon-tungsten ECAL) and hadronic (scintillator-steel HCAL) calorimeters. These detectors are surrounded by a superconducting solenoid providing a magnetic field of 4 T. Beyond the solenoid, CLICdet comprises an iron yoke interleaved with detectors for muon identification. The forward region of CLICdet close to the beam pipe is equipped with forward calorimeters, called LumiCal and BeamCal, optimised for the luminosity measurements and forward electron-tagging. A more detailed description of CLICdet can be found in [\[11\]](#). CLICdet was optimised for operation at $\sqrt{s} = 3 \text{ TeV}$. As background rates at $\sqrt{s} = 380 \text{ GeV}$ are lower, some modifications to the inner detector layers are anticipated for the first energy stage [\[3\]](#). A quarter-view of the cross section of the CLICdet concept is shown in [Figure 34\(a\)](#). An enlarged view of the vertex detector is shown in [Figure 34\(b\)](#). The forward region of the detector is presented in [Figure 34\(c\)](#).

An important change with respect to the CDR detector models [\[3\]](#) is the location of the final

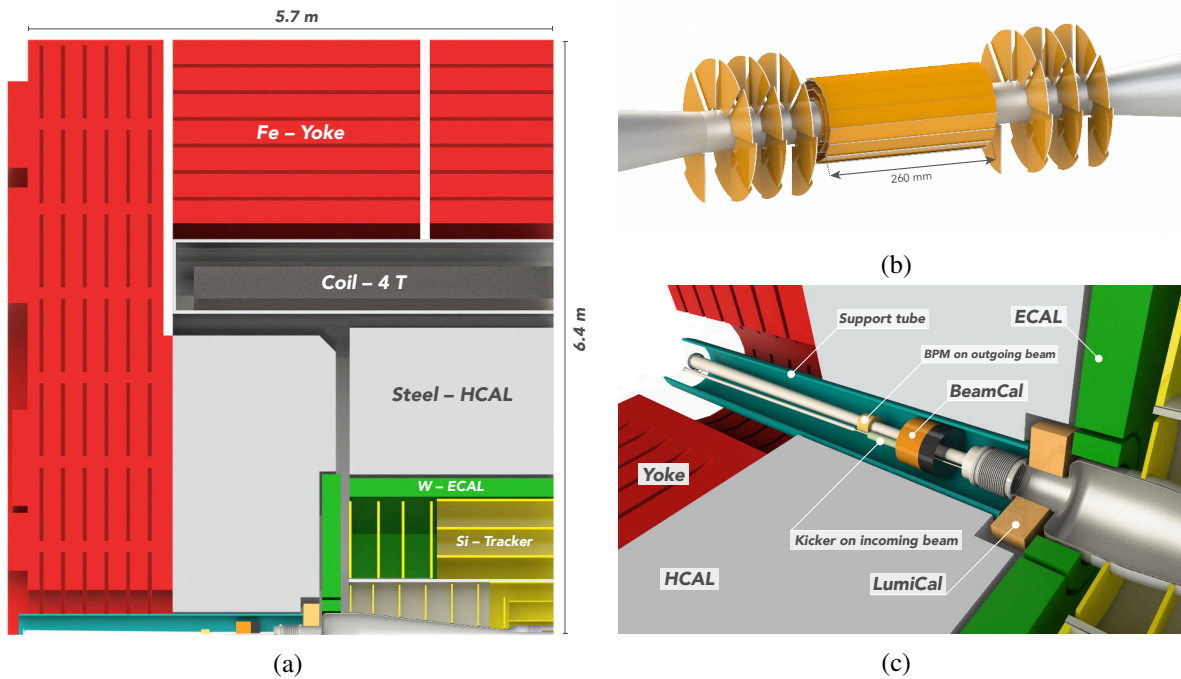


Figure 34: (a) Longitudinal cross section showing a quadrant of CLICdet (side view). The structures shown on the left of the image (i.e. outside of the yoke endcap) represent the end coils. (b) View of the vertex detector layout, with three double-layers in the barrel, and double-layer forward petals in a spiralling arrangement to facilitate air cooling. (c) Layout of the forward region of CLICdet. (image credit: CLICdp)

focusing quadrupole QD0. In order to enlarge the angular coverage of the HCAL endcap and thus to extend the physics reach of the CLIC detector, this quadrupole is located outside of the detector in the accelerator tunnel. Nevertheless, for best luminosity performance the QD0 must be as close as possible to the interaction point. The overall length of CLICdet has therefore been minimised by reducing the thickness of the iron yoke endcaps. The missing iron is compensated by a set of end coils. Both the position of the QD0 in the accelerator tunnel as well as the end coils are shown in [Figure 35\(a\)](#).

[Figure 35\(b\)](#) shows the experimental cavern around the interaction point as well as the service cavern, where the final assembly of the detector and maintenance work will take place. Contrary to the push-pull scenario with two detectors, described in the CDR, operation with only one detector at CLIC is proposed here.

4.4 Detector technologies

A broad detector technology R&D programme for CLIC has been ongoing for several years, as described in detail in [13]. In view of the time scales involved and the limited resources, the development targets those areas where CLIC requirements are the most challenging: the silicon vertex and tracking system, the high-granularity ECAL and HCAL calorimeter systems, as well as the compact very forward electromagnetic calorimeters LumiCal and BeamCal. The technology R&D effort for the silicon vertex and tracking system is coordinated by the CLICdp collaboration, while the calorimeter developments are carried out within the CALICE and FCAL collaborations. For the muon identification system, CLIC requirements do not represent particular challenges. Therefore work was not yet initiated in this domain. The large superconducting detector solenoid, operating at 4 T, has been the subject of design studies [3] and first extrusion tests towards a reinforced conductor have been performed [104, 105]. With its 3.5 m

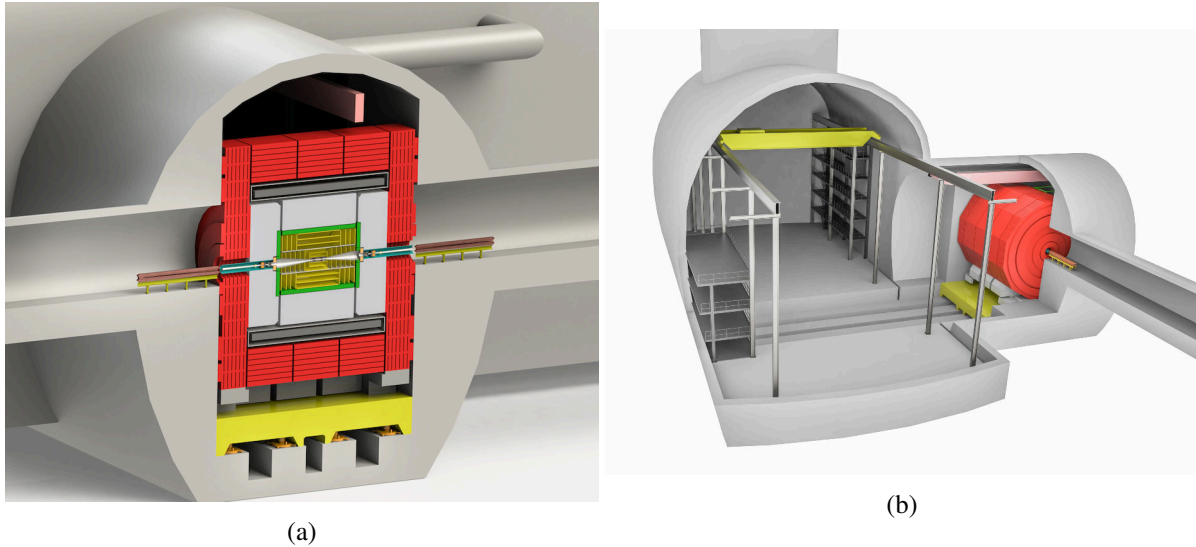


Figure 35: (a) The last focusing magnets QD0 are located just outside of CLICdet.
 (b) Experimental cavern and service cavern of CLICdet. (image credit: CLICdp)

inner bore radius, technology challenges for the CLIC solenoid go beyond what was achieved for the CMS experiment. Development for the solenoid will therefore have to start as soon as decisions towards the realisation of CLIC are taken. Several general engineering studies, including detector assembly and access scenarios, were performed in the framework of the CDR [3]. More recent engineering studies have focused mainly on the vertex and tracking system, in particular concerning low-mass supporting structures and air cooling [106, 107].

4.4.1 Vertex and tracking technologies

The CLIC physics objectives, combined with its experimental conditions, pose challenging technology requirements on the vertex and tracking system. For the vertex detector, the occupancy from beam-induced background particles requires the pixel size to be $\leq 25 \times 25 \mu\text{m}^2$. A hit position resolution of $3 \mu\text{m}$ is required, together with a hit time resolution of approximately 5 ns. The material budget must be at most $0.2\% X_0$ per layer, including sensors, electronics, supports and cabling. This limit in material budget implies a limit of $50 \text{ mW}/\text{cm}^2$ on power consumption including power pulsing, as this will allow for air cooling. While the individual requirements for the vertex detector can be met using state-of-the-art technologies, the combination of all requirements is very challenging and requires new technological solutions. Compared with the vertex detector, the technology requirements on the CLIC tracking layers are more relaxed. Occupancies in the tracker impose strip length limits of 1 mm to 10 mm for an assumed strip pitch of $50 \mu\text{m}$ [108]. Anticipating future advances in integrated technologies, one can expect, however, that large pixels will be chosen for the tracker instead. A hit position resolution of $7 \mu\text{m}$ and a hit time resolution of $\sim 5 \text{ ns}$ are required, while the material budget is limited to $2\% X_0$ per layer. Leak-less water cooling at sub-atmospheric pressure and at room temperature is currently foreseen for the tracker. The expected radiation exposure from non-ionising energy loss, dominated by $\gamma\gamma \rightarrow$ hadrons events, leads to an equivalent neutron flux below $1 \times 10^{11} \text{ neq}/(\text{cm}^2 \text{ yr})$ in the inner vertex layers. The total ionising dose is dominated by background from incoherent pairs and is less than $1 \text{ kGy}/\text{yr}$ in the inner vertex layers.

In order to match the challenging vertex detector requirements, a comprehensive R&D programme is ongoing. It involves simulations, ASIC and sensor designs, the construction and readout of small detector assemblies, laboratory tests and beam tests. It addresses several state-of-the-art technology ap-

proaches and includes systematic performance mapping of parameters (e.g. sensor thickness) in order to fully understand options and dependencies. Detector simulation tools have been extended and refined accordingly in order to guide subsequent R&D steps [109]. Both hybrid assemblies and depleted monolithic sensors are assessed. In addition, the feasibility of power pulsing, air cooling and ultra-thin support structures have been assessed for the vertex detector. While the R&D programme focused initially on the vertex detector with small pixels of $25 \times 25 \mu\text{m}^2$, some of the technologies are now also under consideration for the CLIC tracker.

For the different development steps undertaken, suitable test assemblies were designed, built and tested. These are listed in Table 7. Timepix and Timepix3 ASICs with $55 \times 55 \mu\text{m}^2$ pixel pitch have been used in initial studies of hybrid assemblies in order to assess the effect of sensor thickness on the charge-collection efficiency and the position resolution. Subsequently, the CLIC project pioneered a first hybrid pixel detector ASIC for particle physics in 65 nm CMOS process technology and with small $25 \times 25 \mu\text{m}^2$ pixel size. As a result CLICpix and its CLICpix2 upgrade are used in hybrid detector assemblies. In these assemblies either a thin silicon planar sensor is bump-bonded directly to the ASIC (DC coupling), or a HV-CMOS (High Voltage) sensor with embedded amplification is glued to the ASIC (capacitive coupling). In another approach, monolithic CMOS technologies are explored. Recent progress with depleted monolithic CMOS technologies make them promising candidates for large-scale systems with low mass, together with facilitated production and reduced cost. In these technologies, the depleted signal formation region and the electronic readout circuitry are embedded in the same monolithic device. In the HV-CMOS technology studied, the pixel circuitry is embedded in a deep n-well that covers most of the pixel area. The deep n-well acts as a signal collecting electrode, while shielding the CMOS readout circuitry from the high voltage applied to the silicon bulk. On the other hand, HR-CMOS (High Resistivity) sensors are designed with a small collection electrode on top of a depleted high-resistivity epitaxial layer to achieve a small sensor capacitance for a large signal-to-noise (S/N) ratio and a low analogue power consumption. Monolithic Silicon-On-Insulator (SOI) wafers implement a layer of SiO_2 insulator between a high-resistivity sensor wafer and a thin low-resistivity electronics wafer. Figures 36 to 38 show a collection of images illustrating the silicon vertex and tracker R&D effort.

Table 7: Summary of sensor assemblies and technologies explored in the framework of the CLIC vertex and tracker detector R&D.

test assembly	type	coupling	cell size (μm^2)	active sensor thickness (μm)	references
Timepix(3) + Si sensor	hybrid planar	bump-bonded	55×55	50 – 500	[110–113]
CLICpix + Si sensor	hybrid planar	bump-bonded	25×25	50 – 200	[114]
CLICpix2 + Si sensor	hybrid planar	bump-bonded	25×25	130, 200	[115]
CLICpix + CCPDv3	hybrid HV-CMOS	capacitive	25×25	~ 30	[116–119]
CLICpix2 + C3PD	hybrid HV-CMOS	capacitive	25×25	$\sim 30 - 100$	[120, 121]
ALICE investigator	HR-CMOS	monolithic	28×28	$\sim 15 - 20$	[122, 123]
ATLASpix simple	HV-CMOS	monolithic	40×130	$\sim 30 - 100$	[124]
Cracow SOI	SOI	monolithic	30×30	300, 500	[125]
CLIPS	SOI	monolithic	20×20	100 – 500	in production
CLICTD	HR-CMOS	monolithic	$30 \times (8 \times 37.5)^a$	< 40	design phase [126]

^a The CLICTD cells are segmented in 8 sub-pixels in the long direction, in order to maintain the benefits of the small collection electrode.

Given the progress with the CLIC vertex and tracker R&D, together with overall expected advances in semiconductor technologies worldwide, one can expect good prospects for reaching the CLIC objectives in due time. At the current phase of the CLIC vertex and tracker R&D, a number of conclusions can already be drawn from the obtained results:

- Good S/N ratios have been achieved for the detection of signals from thin ($50\mu\text{m}$) fully-depleted planar sensors, sufficient for full detection efficiency and for satisfying the CLIC time-stamping requirements [110, 111, 113].
- In general the position resolution depends strongly on the pixel size and on the depleted sensor thickness. For planar sensors, small sensor thicknesses, which are needed to reach the low-mass requirements, go together with small charge sharing, limiting the achievable position resolution [110, 111]. Sensor design with enhanced charge sharing is underway [127]. More advanced ASIC process technologies (e.g. 28 nm instead of 65 nm) offer prospects for smaller pixel sizes and better position resolution.
- Good progress was made towards reducing detector mass through the use of active-edge sensor technologies [111, 112] and advances in Through-Silicon Via (TSV) interconnect technologies [128, 129].
- Fine-pitch bump-bonding processes for hybrid silicon detector assemblies with pixel sizes as small as $25 \times 25\mu\text{m}^2$ are not readily available commercially at single die level. This slows down the R&D process for this type of detector [114, 115]. Capacitively coupled hybrid detectors have been assembled and operated successfully [116–121]. They, however, pose other challenges, such as uniform pressure and planarity during the bonding step, as well as the integration and cooling of larger module surfaces.
- Promising results were obtained from tests using integrated technologies (SOI, HV-CMOS, HR-CMOS) [122–125]. CLIC-specific fully integrated designs are underway (CLICTD [126], CLIPS). Integrated technologies offer a potential for high-precision performance over large surfaces, with a reduced material budget and at a lower cost.
- Feasibility of power pulsing was demonstrated at the level of module-size low-mass powering demonstrators in the laboratory, including tests in a magnetic field [130, 131]. Power pulsing was also implemented successfully in hybrid ASICs and HV-CMOS sensors for CLIC. Power consumption levels below $50\text{mW}/\text{cm}^2$ have been achieved.
- Feasibility of air cooling was demonstrated in simulation studies and in a full-scale CLIC vertex detector mock-up with realistic heat loads [107].

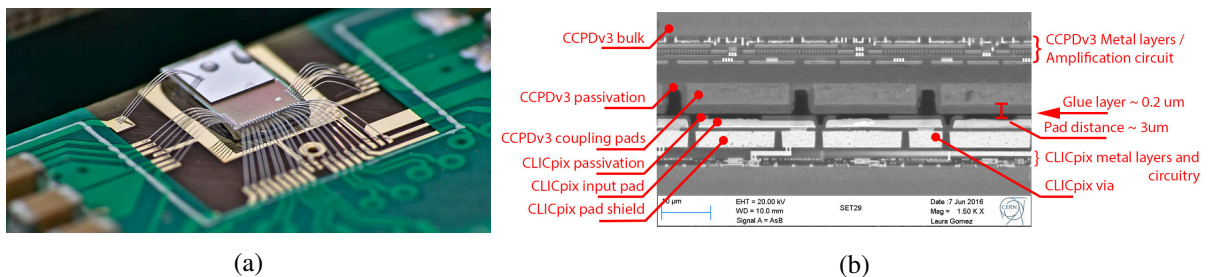


Figure 36: (a) Photograph of a ($50\mu\text{m}$) thin planar sensor, shown on top, bump-bonded to a CLICpix ASIC, shown at the bottom. (b) Scanning electron microscope image of the cross section through a CCPDv3 and CLICpix capacitively-coupled assembly, showing the active HV-CMOS CCPDv3 sensor at the top, the CLICpix ASIC at the bottom, and the thin glue layer in the middle. (image credit: CLICdp)

4.4.2 Electromagnetic and hadronic calorimeters

Requirements on the barrel and endcap calorimeter systems are driven by physics performance aims combined with the need to efficiently reject beam-induced background particles in the data. Highly-

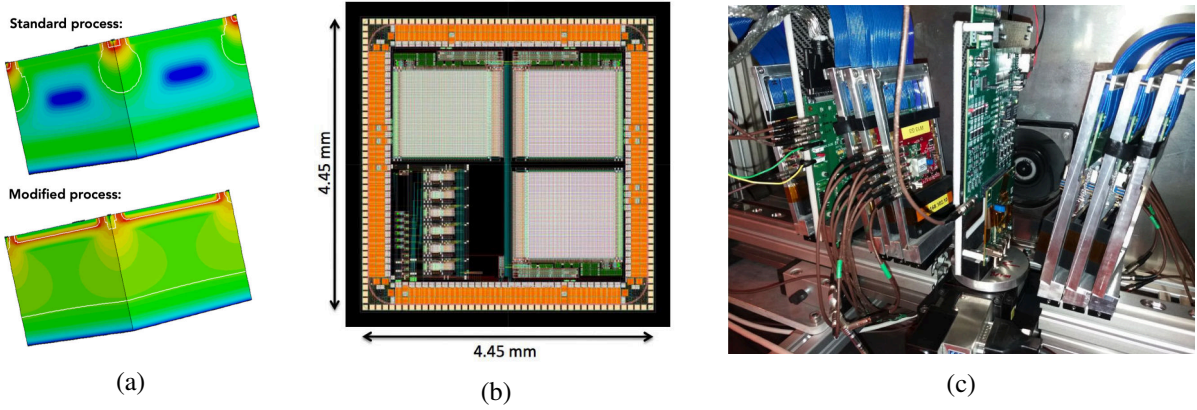


Figure 37: (a) Images of 3D TCAD (Technology Computer Aided Design) simulations of single-pixel electric field distributions for two HR-CMOS process variants. (b) Sensor layout of the CLIPS fully monolithic sensor with $20 \times 20 \mu\text{m}^2$ pixel sizes, designed in SOI technology. (c) Photograph of the Timepix3 test beam telescope that was built for testing CLIC vertex and tracking R&D assemblies. Seven Timepix3 reference layers are shown, together with two devices under test. (image credit: CLICdp)

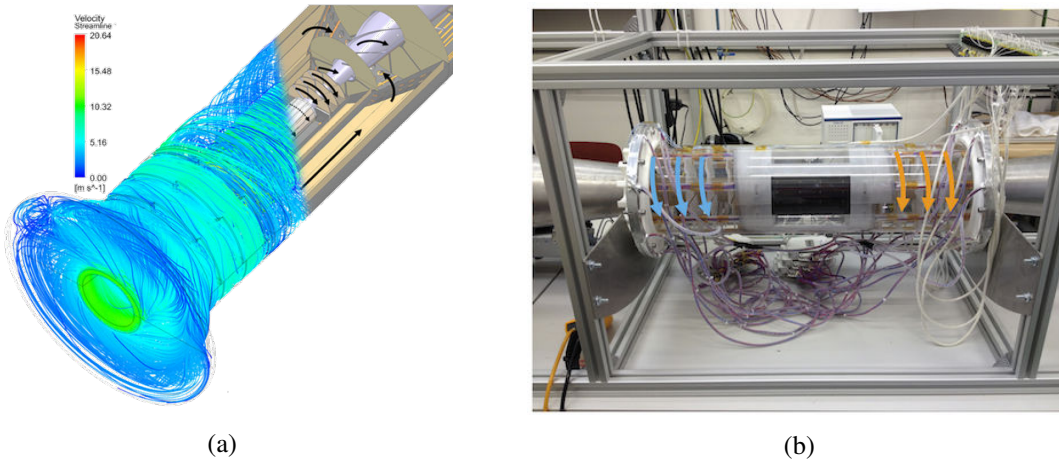


Figure 38: (a) Composed image showing the vertex detector design, together with stream lines of cooling air as simulated by computational fluid dynamics. (b) Photograph of a full-scale vertex detector mock-up, used to demonstrate the feasibility of air cooling. (image credit: CLICdp)

granular calorimetry together with performant particle flow analysis efficiently address both requirements. The CLICdet calorimeter system has been optimised accordingly, by combining simulation results with CALICE technology experiences on highly-granular calorimetry [11, 132]. The electromagnetic calorimeter comprises a 40-layer sandwich of silicon pad sensors as active material interspersed with 1.9 mm tungsten plates, for a total depth of $22X_0$ and $1\lambda_1$. The silicon pads have a lateral size of $5 \times 5 \text{ mm}^2$, and each active layer occupies only 3.15 mm in depth, including space for readout and cabling. The hadronic calorimeter comprises a 60-layer sandwich of plastic scintillator active material interspersed with 19 mm thick steel plates, for a total depth of $7.5\lambda_1$. The scintillator tiles, with a thickness of 3 mm and $3 \times 3 \text{ cm}^2$ lateral size, are read out individually by silicon photomultipliers (SiPM). Each active layer covers 7.5 mm in depth. A time resolution of 1 ns is required for individual calorimeter hits in ECAL and HCAL. A large dynamic range is required, covering large energy deposits from high-energy showers, as well as from single minimum-ionising particles.

Technologies for both the silicon-tungsten (SiW) ECAL and the scintillator-steel analogue HCAL (AHCAL) have been validated through the construction and tests of successive prototypes. Initial prototypes, the so-called physics prototypes [133, 134], served to implement the core technology features in devices. These prototypes are large enough to assess their response to showers from individual particles and to provide detailed shower data for validating the expected jet performance through event reconstruction with PandoraPFA particle flow analysis [21–24]. Also they served to gain deeper understanding of core technological aspects like mechanical assembly, embedded electronics, signal development, noise, power pulsing (SiW ECAL), calibration and systematic effects [135]. For the 30-layer SiW ECAL the results show an energy resolution for electrons at the level of $16.6\%/\sqrt{E}$ with a constant term of 1.1% [136]. Furthermore, a full separation of close-by particles down to a distance of 2.5 cm was demonstrated [135]. A 38-layer AHCAL prototype with more than 7000 readout cells was built and tested in beams of different particles over a wide energy range. This was the first device to use SiPMs on a large scale. The imaging capabilities of the calorimeter allow exploiting shower substructures, such as using MIP tracklets for calibration purposes or using knowledge of local hit density for improving the energy resolution through software compensation [137]. Exposure to pions in the range 10 - 80 GeV yields an energy resolution at the level of $57.6\%/\sqrt{E}$ with a constant term of 1.6%. This result is further improved to $44.3\%/\sqrt{E}$ with a constant term of 1.8% through software compensation, which gives a lower weight to energy deposits in high-density regions.

The next generation of highly-granular calorimeter prototypes are so-called technological prototypes. Their design includes lessons learned from the first generation prototypes and, in addition, includes engineering constraints and scalability features for the construction, that will also be needed for the final detectors. One example is the SiPM-on-tile hadronic calorimeter prototype, comprising 38 detection layers for a total of nearly 22000 scintillator tiles (see Figure 39(a)) [138]. For this prototype, construction and quality assurance processes have been optimised and automatised. For example, the SiPMs are integrated in the readout boards, the scintillators are produced and wrapped via automated processes and the assembly makes use of automated pick-and-place devices. Improved electronics readout with auto-triggering capability, nanosecond-level timing capabilities and power pulsing is included. Figures 39(b) and 39(c) show event displays of a 100 GeV electron and a 100 GeV hadron, respectively, recorded with the SiPM-on-tile calorimeter prototype at the CERN SPS test beam.

Likewise, recent prototypes of the SiW ECAL integrate more of the engineering and scalability aspects, which will be needed for the future silicon ECAL calorimeter system with tens of millions of channels. For the current prototypes, electro-mechanical challenges were overcome in order to fit the active layers into thin slots (< 4 mm) between the absorber layers. Robotic procedures are used for the assembly. Modules with 5×5 mm² cell sizes and advanced electronics readout features are currently undergoing beam tests. Two sensor thicknesses are used, 320 μ m and 650 μ m, in order to assess the optimal signal-to-noise ratio.

CALICE prototype results confirm the performances expected from simulations, thereby giving overall confidence in the performance predictions for the CLIC detector.

4.4.3 Very forward calorimeters

The very forward calorimeters, LumiCal and BeamCal, are compact fine-grained cylindrical electromagnetic calorimeters centred on the outgoing beams at 2.5 m and 3.2 m from the interaction point, see Figure 34(c). Their main functions include tagging of very forward-going electrons and photons, as well as in-situ measurement of the luminosity based on Bhabha scattering. Their geometrical acceptance range spans $\theta = 10 - 46$ mrad for BeamCal and $\theta = 39 - 134$ mrad for LumiCal. In view of large beam-induced backgrounds in this region, the very forward calorimeters are exposed to high radiation levels. This holds in particular for BeamCal for which radiation resistance for an ionising dose of up to 1 MGy per year is required. Angular precision for the measurement of high-energy electromagnetic showers

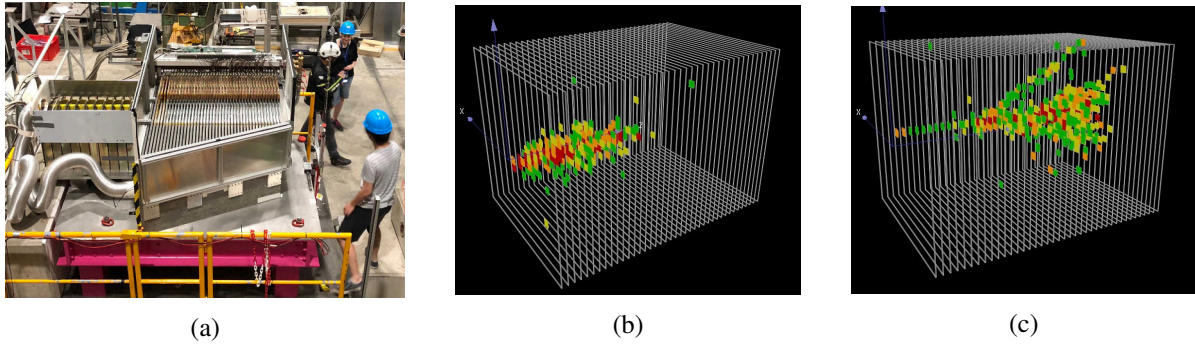


Figure 39: (a) Photograph of the CALICE SiPM-on-tile hadronic calorimeter technological prototype, comprising 38 detection layers for a total of nearly 22000 scintillator tiles. (b) Event display of a 100 GeV electron. (c) Event display of a 100 GeV hadron. (image credit: CALICE)

(up to 1.5 TeV) call for a very small Molière radius of ~ 1 cm and a large dynamic range. Both devices are based on 40-layer sandwich designs comprising $300\ \mu\text{m}$ thick semiconductor detectors (in < 1 mm gaps) interleaved with 3.5 mm thick ($1 X_0$) tungsten absorbers. The detector development for the very forward calorimeters is carried out in the framework of the FCAL collaboration. Detector development for BeamCal principally concentrates on radiation studies of sensor materials (GaAs, sapphire, SiC and silicon diode sensors). Recent LumiCal milestones are the construction and beam tests of compact 4-layer and 8-layer LumiCal prototypes with silicon sensors. The 4-layer prototype uses custom-designed FCAL electronics, albeit with a limited number of readout channels, whereas the 8-layer prototype is based on existing APV25 readout ASICs [139–142]. For the latter, ultra-compact readout layers were achieved, covering only $650\ \mu\text{m}$ in depth including connections to the readout electronics located outside the active area. As a result, a small effective Molière radius of 8.1 ± 0.3 mm was measured [143] using electron beams of 1–5 GeV. Current FCAL prototypes use silicon pad sizes of $\sim 0.3\ \text{cm}^2$. In view of the high occupancies expected at CLIC, significantly reduced pad sizes will be an advantage. Ongoing R&D on monolithic CMOS silicon sensors with small pixel sizes (see Section 4.4.1) opens future perspectives towards pixelised (analogue or digital) LumiCal sensor layers, offering compactness as well as large dynamic range for the measurement of high-energy electromagnetic showers. While radiation tolerances of up to 1 MGy have been achieved for BeamCal for several sensor technologies, further R&D is needed to fully assess the performance of the various sensor materials and means to integrate them in BeamCal. The forward calorimeters also require very high alignment accuracy of $10\ \mu\text{m}$ in transverse direction and $100\ \mu\text{m}$ in longitudinal direction, for which initial concepts have been devised.

4.5 Detector performance

In this section a summary of the CLICdet detector performance is presented for single particles, complex events and jets. Individual particles are used to probe track reconstruction and particle identification, while the reconstruction of particles inside jets and the flavour tagging performances are tested in di-jet events. Jet energy and angular resolution as well as W - Z mass separation are studied in di-jet samples.

The CLICdet detector geometry is described with the DD4hep software framework [144] and simulated in Geant4 [145–147]. The reconstruction software is implemented in the linear collider Marlin-framework [19]. The reconstruction algorithms use geometry information provided by DD4hep [148]. The reconstruction starts with the overlay of $\gamma\gamma \rightarrow$ hadrons background events, corresponding to 30 bunch crossings around the physics event [149]. Subsequently, the hit positions in the tracking detectors are smeared with Gaussian distributions according to the expected resolutions. Tracks are reconstructed using the ConformalTracking algorithm [150]. Particles are reconstructed and identified using the

PandoraPFA particle flow algorithms [21–24], combining information from tracks, calorimeter clusters, and hits in the muon system. The detector response to each type of Pandora particle flow object (PandoraPFO) – charged hadrons, photons, neutral hadrons, electrons, and muons – is calibrated separately with type-specific calibration constants. After full particle flow reconstruction, particles from beam-induced backgrounds are suppressed through p_T -dependent timing cuts described above. Vertex reconstruction and heavy-flavour tagging is performed by the LCFIPlus program [25]. Larger simulation and reconstruction samples were produced with the iLCDirac grid production tool [151]. A more detailed description of the software tools, analysis methods and a complete set of performances are given in [12]. Selected examples are presented below.

Tracking performance Figure 40 shows the transverse momentum resolution and the transverse impact parameter resolution, obtained with isolated muon tracks of different momenta and polar angles. The precise measurement of leptonic final states requires a transverse momentum resolution of the order of $2 \times 10^{-5} \text{ GeV}^{-1}$ for high-energy particles [3], which is achieved in the central detector region as shown in Figure 40(a). Similar performances are achieved with isolated electrons and pions. Efficient flavour tagging, relying on the precise reconstruction of primary and secondary vertices, requires excellent impact parameter resolution. The targeted transverse impact parameter resolution, depicted as dashed lines in Figure 40(b), is clearly reached for high-energy muons in the central detector region. This result is closely linked to the single point resolution in the vertex detector: varying this parameter from the nominal $3 \mu\text{m}$ to $5 \mu\text{m}$ leads to a d_0 resolution degradation by 50%. The material budget in the vertex detector impacts the 10 GeV tracks in the forward detector region, and the 1 GeV tracks at any angle (cf. Figure 40(b)). In additional studies, the longitudinal impact parameter resolution is found to be much smaller than the longitudinal bunch length ($44 \mu\text{m}$ at 3 TeV collision energy) for high-energy muons at all polar angles and reaches a minimum of $1.5 \mu\text{m}$ for 100 GeV muons at 90° . Polar and azimuthal angular resolutions of, respectively, 0.05 mrad and 0.025 mrad are achieved for high-energy muons in the central detector region.

Tracking performance has been studied in detail for prompt and displaced (i.e. not originating from the interaction point) tracks [12]. A reconstruction efficiency of 100% has been demonstrated for single particles (muons, pions, electrons), with an efficiency loss of up to 1% observed only in the very forward region ($\theta = 10^\circ$). Similarly, tracks from displaced particles are found to be reconstructed with good efficiency.

The tracking efficiency and fake rate inside jets have been tested in $b\bar{b}$ events at 3 TeV centre-of-mass energy. The results are shown in Figure 41 as a function of transverse momentum. Fully efficient tracking down to $p_T \simeq 1 \text{ GeV}$ is observed, then the efficiency decreases to 92% at $p_T = 100 \text{ MeV}$. This value is reduced to 80%, when beam-induced background particles from $\gamma\gamma \rightarrow \text{hadrons}$ events as produced at the 3 TeV CLIC stage are overlaid (cf. Figure 41(a)). In these studies, only tracks are considered, whose associated Monte Carlo particle is separated from all other particles by at least 0.02 rad, in order to limit confusion in pattern recognition. However, the efficiency loss for less separated tracks is found to amount to only 2–3%, independently on the beam-induced background.

The fake rate is shown in Figure 41(b). In events without backgrounds, it increases with transverse momentum from 0.3% at 1 GeV to roughly 1% above 10 GeV, where more straight tracks lead to increased confusion in pattern recognition. The effect of background is particularly large for $p_T < 1 \text{ GeV}$, and the fake rate reaches a maximum of 6% at 100 MeV. The origin of this fake rate is found to be mostly due to tracks in the region $10^\circ < \theta < 20^\circ$, and due to two particles separated by less than 0.04 rad. The fake rate for displaced tracks amounts to a few percent for the whole range of radii of production vertices probed, while the beam-induced background is found to have a small impact. For additional investigations, using Z/γ^* events of different masses decaying into light quarks and $t\bar{t}$ events at 3 TeV, performance very similar to that described above for $b\bar{b}$ has been found.

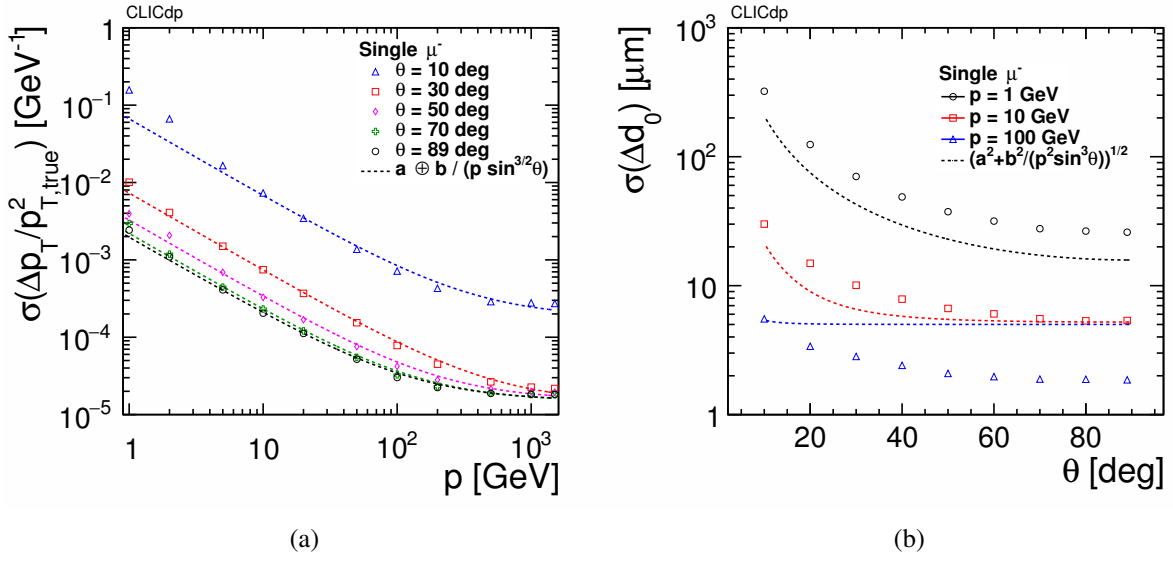


Figure 40: (a) Transverse momentum resolution as a function of momentum for muons at polar angles $\theta = 10^\circ, 30^\circ, 50^\circ, 70^\circ, 89^\circ$ and (b) transverse impact parameter resolution as a function of polar angle for muons with momenta of 1, 10 and 100 GeV [12]. The lines in (a) represent the fit of each curve with the parameterisation as inserted in the figure. In figure (b), the lines show the detector performance goals with $a = 5 \mu\text{m}$ and $b = 15 \mu\text{m GeV}$ used in the parameterisation inserted [3].

Calorimetry performance The PandoraPFA particle identification efficiency is studied over a wide range of energies in all regions of polar angle [12], and more than 90% efficiency is found for all particle types, all energies, and for polar angles from $15^\circ - 165^\circ$. In the case of muons, the identification efficiency is larger than 99% from 10 GeV up to 1.5 TeV. The impact of beam-induced backgrounds from $\gamma\gamma \rightarrow \text{hadrons}$ is investigated in $t\bar{t}$ events at 3 TeV. Considering the W bosons leptonically decaying into muons and electrons in these events, the muon identification is largely unaffected, while the efficiency for electrons is reduced by 3–5%.

Di-jet samples from $Z/\gamma^* \rightarrow q\bar{q}$ (with $q=u, d$ or s quarks), simulated without initial state photon radiation and at several centre-of-mass energies, are used to study the performance of jet reconstruction. Software compensation [152] is applied to hadron clusters in the HCAL, in order to improve their energy measurement. The jet energy resolution is studied by comparing the response of Monte Carlo (MC) truth particle-level jets (clustering stable particles excluding neutrinos) to those reconstructed at detector level (clustering PandoraPFOs), using the VLC algorithm [153] in exclusive mode to force the event into two jets. The γ and β of VLC parameters are fixed to 1.0 and the radius parameter is set to $R = 0.7$. The two reconstructed jets are required to be matched to each of the MC truth particle-level jets within an angle of 10° .

The resulting jet energy resolution is shown in Figure 42(a) for several jet energies as function of the $|\cos\theta|$ of the quark. The performance goal [3] of 3–4% jet energy resolution at high energies is achieved in the barrel ($|\cos\theta| < 0.7$) and endcap region with the exception of the most forward angles. For low energy jets (50 GeV), the jet energy resolution is around 4.5–5.5%. For very forward jets with $0.975 < |\cos\theta| < 0.985$, the jet can be partly outside of the tracker volume. This leads to a large tail to lower reconstructed energies, and is reflected in jet energy resolution values which reach up to 20%.

In events where 3 TeV beam-induced backgrounds from $\gamma\gamma \rightarrow \text{hadrons}$ are overlaid on the physics event, *Tight* selection cuts are applied to the PandoraPFOs prior to jet clustering [3]. Figure 42(b) shows the jet energy resolution for di-jet events with 3 TeV $\gamma\gamma \rightarrow \text{hadrons}$ background overlaid. A degradation

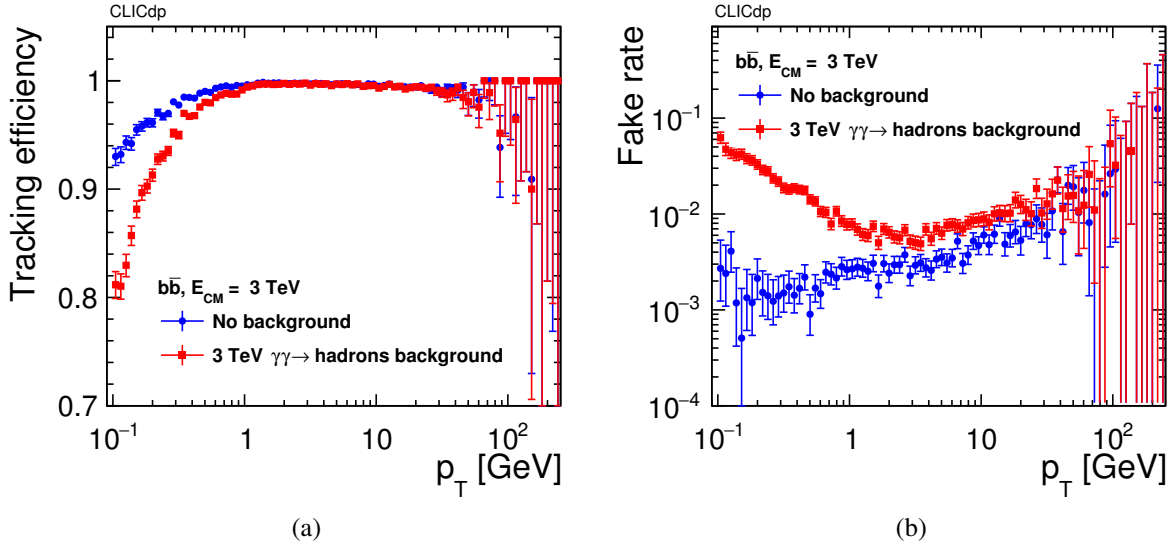


Figure 41: (a) Tracking efficiency and (b) fake rate as a function of p_T for $b\bar{b}$ events at 3 TeV, with and without $\gamma\gamma \rightarrow$ hadrons background overlay [12]. Note that the errors bars indicate statistical uncertainties, which are naturally larger at high p_T due to the particle spectrum in the sample used.

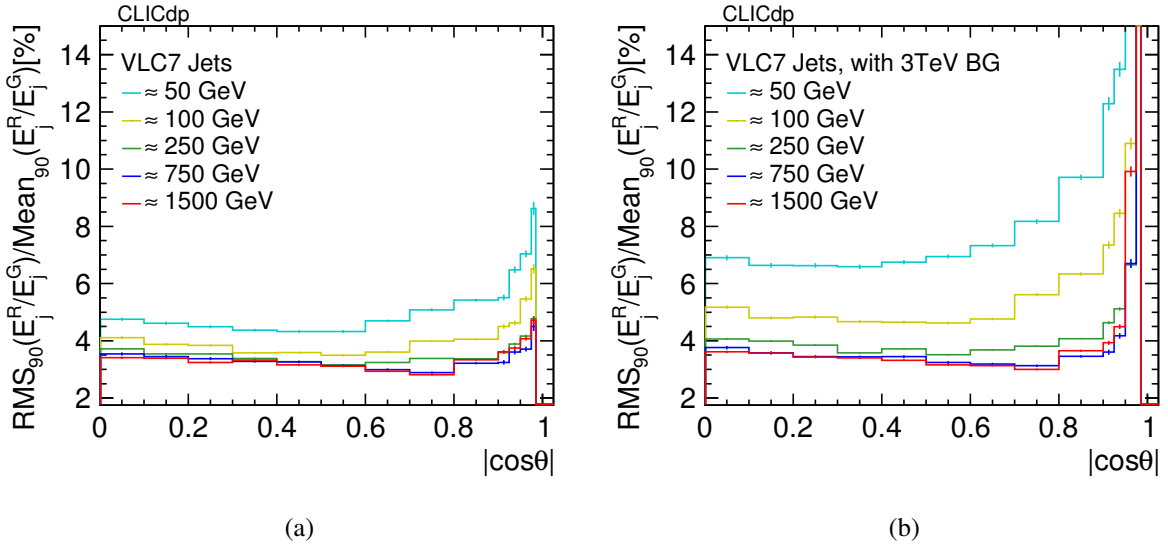


Figure 42: (a) Jet energy resolution for various jet energies as function of $|\cos\theta|$ of the quark for events without and (b) with $\gamma\gamma \rightarrow$ hadrons background conditions at 3 TeV. RMS_{90} is used as a measure of the jet energy resolution [12].

of the jet energy resolution is observed for all jet energies, however for high energy jets, this is limited to less than 0.5% for most of the $|\cos\theta|$ range. Since hadrons from beam-induced backgrounds tend to be produced more in the forward direction, the impact is larger for jets with $|\cos\theta| > 0.80$.

Beam-induced backgrounds at 380 GeV CLIC are expected to be significantly smaller than at 3 TeV. For this reason less strict *low energy loose* selections [103] are used for 380 GeV jet resolution studies. As shown in Figure 43, overlaying the 380 GeV beam-induced background levels has little impact on the jet energy resolution for most jet energies, except for very forward jets, where an increase

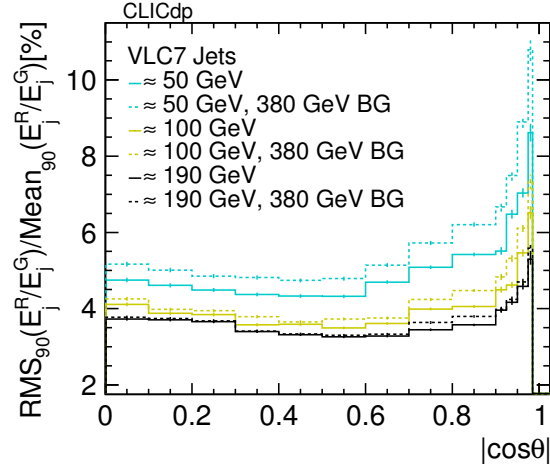


Figure 43: Jet energy resolution for various jet energies as function of $|\cos\theta|$ of the quark with and without 380 GeV $\gamma\gamma \rightarrow$ hadrons background overlaid on the physics di-jet event. RMS90 is used as a measure of the jet energy resolution [12].

of 0.5–1% is observed. Even for 50 GeV jets, only a small degradation of the jet energy resolution to about 5% is observed in the barrel, and to 6–9% for endcap and forward jets. In further studies, jet angular resolutions have been found to be below 1° in azimuth ϕ , and in polar angle θ values below 0.5° have been found for jet energies above 100 GeV.

The precise reconstruction of masses of resonances in hadronic channels over wide ranges of energies is a challenging task. Di-jet masses from hadronic decays of W and Z bosons are studied using simulated di-boson events, in which only one of the bosons decays into di-quarks, i.e. $ZZ \rightarrow \nu\bar{\nu}q\bar{q}$ and $WW \rightarrow l\nu q\bar{q}$. The boson energies in this study vary from 125 GeV, where both bosons are created almost at rest, up to 1 TeV, where the bosons are heavily boosted. The event is clustered in two VLC jets with the same parameter setting and input selection as used in the jet energy resolution studies. In the WW events the charged lepton from the leptonically decaying W is removed prior to jet clustering. A cut is imposed on the polar angle of both MC truth jets $|\cos\theta| < 0.9$ to ensure that jets are well contained within the detector acceptance. The di-jet mass distributions are fitted with a Gaussian, iteratively changing the limits of the fit range to 2σ around each side of the mean of the fit, until the fitted σ stabilises within 5%. As an example, Figure 44 shows the di-jet mass distributions for W and Z bosons with $E = 500$ GeV with the Gaussian fits in events without and with the overlay of 3 TeV beam-induced backgrounds from $\gamma\gamma \rightarrow$ hadrons. The ideal Gaussian separation between the reconstructed W and Z di-jet masses is derived using the overlap fraction between both Gaussian curves, which is defined as the fraction of W (Z) bosons which are above (below) the intersection point of the di-jet mass distributions. Without backgrounds, a separation between 2.0 and 2.5σ can be achieved, corresponding to overlap fractions of 15–19%. In the presence of beam-induced backgrounds as expected for CLIC at 3 TeV, the separation achieved is between 1.7 and 2σ , with overlap fractions between 19 and 23%. For low energy bosons the impact of 380 GeV beam-induced background levels is evaluated, leading to a modest decrease of the separation from 2.1 to 2.0σ .

Flavour tagging performance To investigate detector performances in terms of flavour tagging, di-jet events at 500 GeV centre-of-mass energies (at the 3 TeV CLIC) with a mixture of polar angles between 20° and 90° have been simulated and reconstructed. Tracks and selected PandoraPFOs are used as input to the LCFIPlus vertex finder. The beauty (charm) misidentification probability is assessed separately for charm (beauty) and light-flavour contamination. The effect of 3 TeV $\gamma\gamma \rightarrow$ hadrons background is also

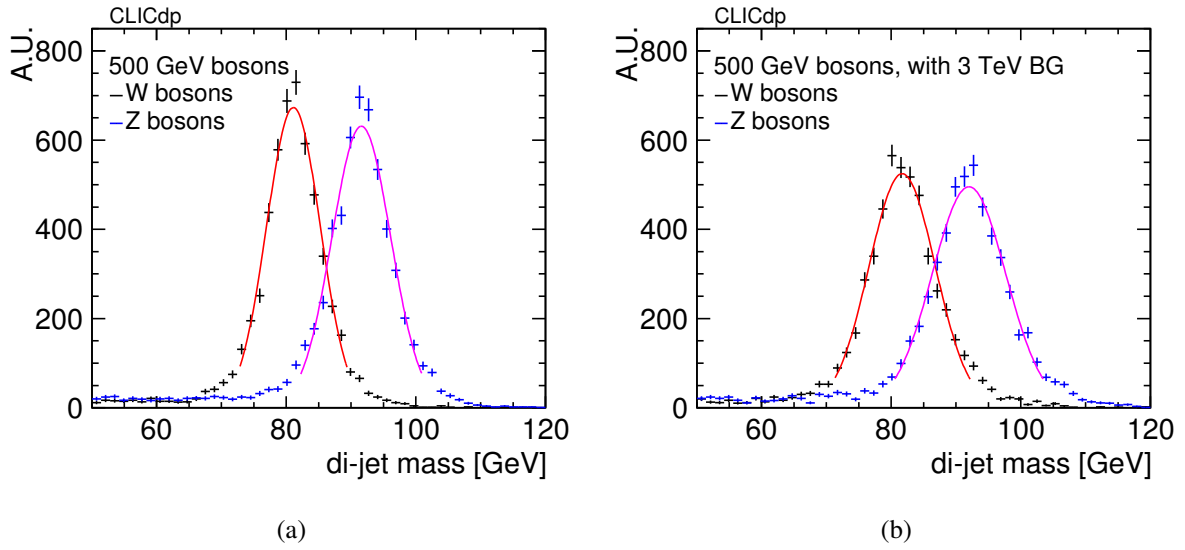
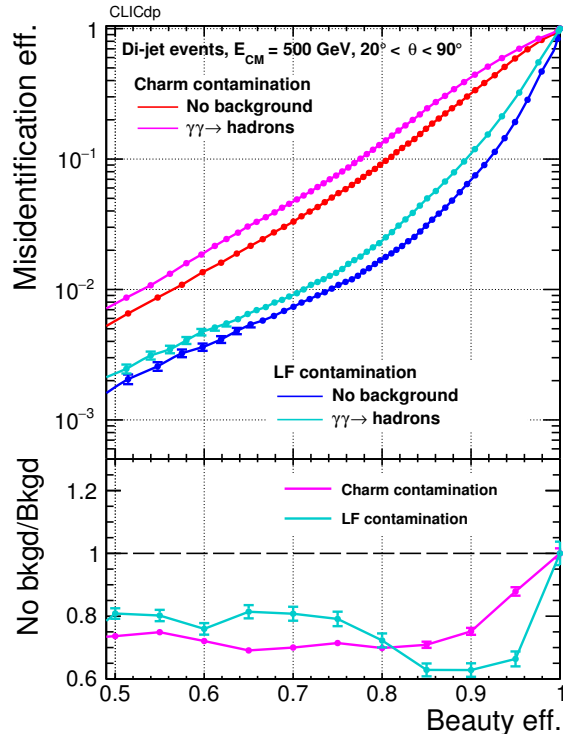


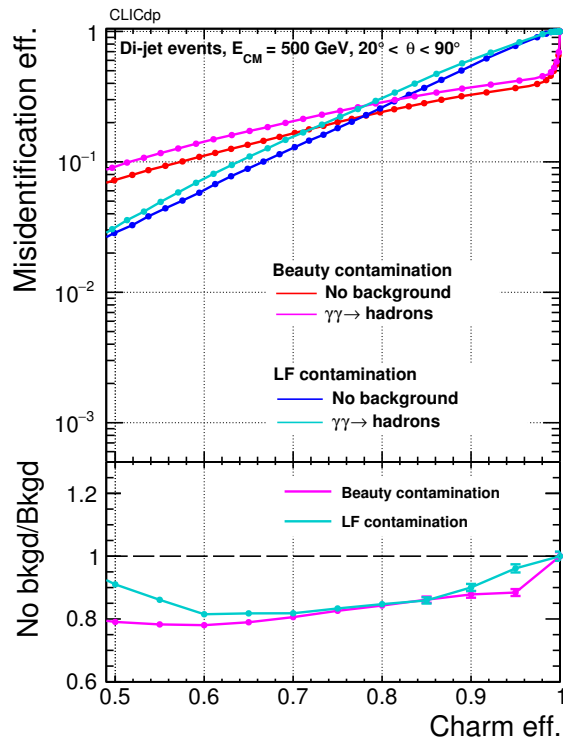
Figure 44: Di-jet mass distributions of hadronically decaying W and Z with $E = 500$ GeV in $WW \rightarrow lvqq$ and $ZZ \rightarrow \nu\bar{\nu}q\bar{q}$ events, together with Gaussian fits of the di-jet mass for events, (a) without beam-induced backgrounds and (b) with overlay of 3 TeV beam-induced backgrounds from $\gamma\gamma \rightarrow \text{hadrons}$ [12].

evaluated. Without background overlaid, at 80% beauty identification efficiency the misidentification amounts to 10% as charm and 1.5% as light-flavour jets. If the $\gamma\gamma \rightarrow \text{hadrons}$ background is included, the performance is slightly worse, with 13% and 2% identified as charm and light-flavour jets, respectively (Figure 45(a)). Similarly, at 80% charm identification efficiency the misidentification is 25% as beauty jets without, 30% with background overlaid (Figure 45(b)). In this case, the same misidentification rate holds for light-flavour jets.

In order to estimate the impact of track reconstruction on the flavour tagging, the same study has been performed using the true (Monte Carlo) pattern recognition [12]. The results indicate that both beauty and charm tagging can be improved by optimising the pattern recognition. In particular, in beauty tagging a reduction of misidentification of a b-quark as c- or light-quark by 20 to 30% can be expected.



(a)



(b)

Figure 45: Global performance of (a) beauty tagging and (b) charm tagging for jets in di-jet events at $\sqrt{s} = 500 \text{ GeV}$ with a mixture of polar angles between 20° and 90° . A comparison of performance with and without $\gamma\gamma \rightarrow \text{hadrons}$ background is presented. On the y-axis, the misidentification probability and the ratio of the misidentification probabilities with and without 3 TeV $\gamma\gamma \rightarrow \text{hadrons}$ background are given [12].

5 CLIC project implementation

The general concept of the CLIC accelerator staging and the parameters of the three centre-of-mass stages are described in [Section 3](#). This section describes the implementation of the CLIC accelerator. [Section 5.1](#) summarises the civil engineering and infrastructure. [Section 5.2](#) describes the schedule for the CLIC programme, from the start of construction to the end of operation at 3 TeV, while [Sections 5.3](#) and [5.4](#) cover the cost, and the power and energy consumption of the accelerator.

5.1 The CLIC stages and construction

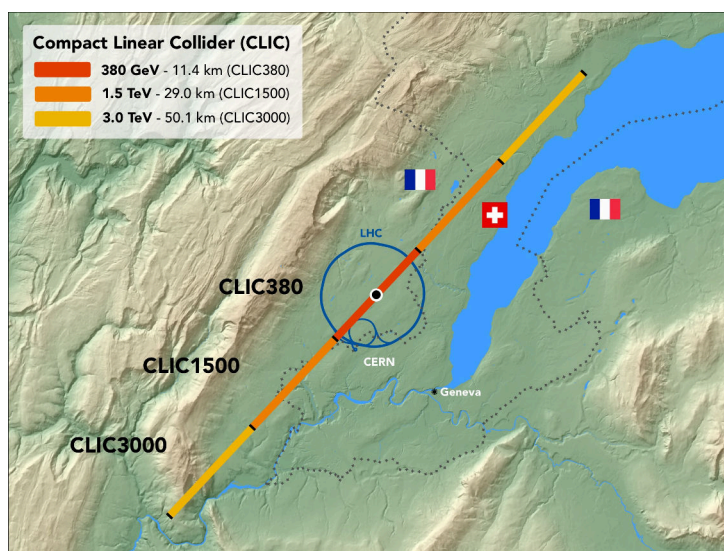


Figure 46: The CLIC main linac footprint near CERN, showing the three implementation stages. (image credit: CLIC)

The CLIC accelerator is foreseen to be built in three stages with centre-of-mass energies of 380 GeV, 1.5 TeV and 3 TeV as schematically shown in [Figure 46](#). [Table 5](#) in [Section 3](#) summarises the main accelerator parameters for the three stages. The accelerator extension from 380 GeV to higher energies is described in [Section 3.4](#). The installation and commissioning schedules are presented in [Section 5.2](#). More details about the CLIC accelerator and the staged implementation can be found in [\[66\]](#).

Along with the optimisation of the accelerator complex for 380 GeV, the civil engineering and infrastructure designs have been revised, maintaining an optimal path for extending the facility to higher energies. These studies are summarised in the following.

5.1.1 Civil engineering and infrastructure

The civil engineering design has been optimised for the 380 GeV stage including: the tunnel length and layout, an optimised injection complex, and a siting optimisation for access shafts and their associated structures. For the klystron option, a larger tunnel diameter is needed and a detailed layout study was completed.

Previous experience from the construction of LEP and LHC has shown that the sedimentary rock in the Geneva basin, known as molasse, provides suitable conditions for tunnelling. Therefore, boundary conditions were established so as to avoid the limestone of the Jura mountain range and to avoid siting the tunnels below Lake Geneva, whilst maximising the portion of tunnel located in the molasse. Based

on the regional geological and surface data, and using a bespoke digital modelling Tunnel Optimisation Tool (TOT) developed specifically for CLIC, a 380 GeV solution has been found that can be readily upgraded to the higher energy stages at 1.5 TeV and 3 TeV. Figure 47 shows the simplified geological profile of the CLIC accelerator stages. The 380 GeV and 1.5 TeV stages are located entirely in molasse rock. The solution shown is both optimised for 380 GeV and provides a realistic upgrade possibility for the 1.5 TeV and 3 TeV stages.

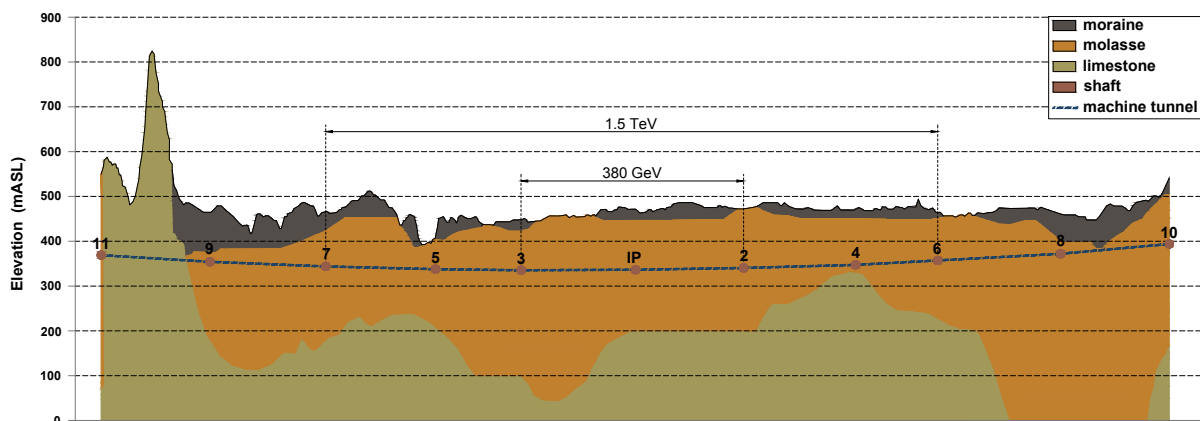


Figure 47: Geological profile of the CLIC three-stage main tunnel. (image credit: CLIC)

An initial boundary condition for the civil engineering layout was to concentrate the drive-beam and main-beam injectors and the interaction point on the CERN Prévessin site. As shown in Figure 48 a solution was found in which the injection complex and the experimental area can be located entirely on CERN land.

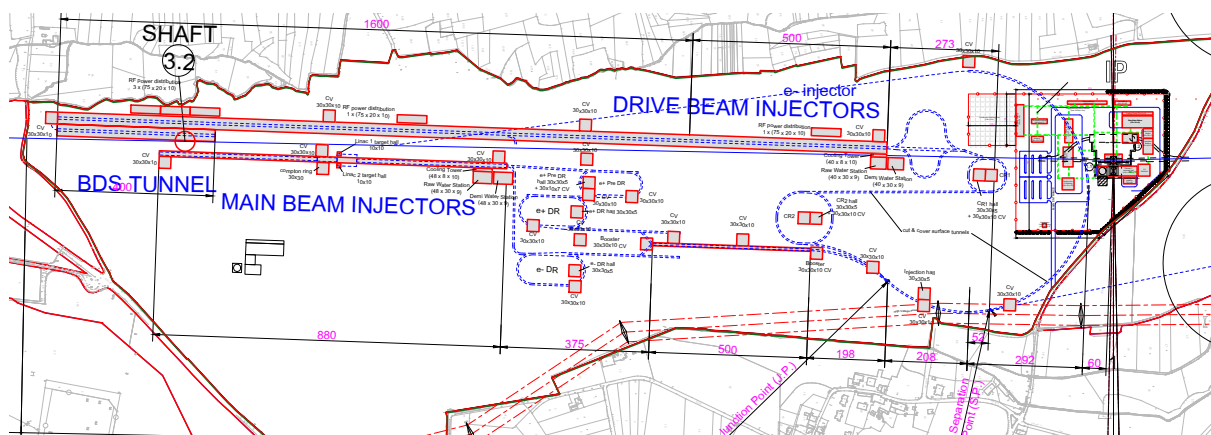


Figure 48: Schematic layout of the injectors, damping rings and drive beam complex centred on the CERN Prévessin site. (image credit: CLIC)

For the baseline design with drive beam a tunnel with a 5.6 m internal diameter is required to house the two-beam modules and all the necessary services, as shown in Figure 49(a). For the klystron design a 10 m internal diameter tunnel is required (Figure 49(b)) to house both the accelerating modules and the klystron gallery separated by a 1.5 m thick shielding wall. In order to minimise the impact of vibrations on the accelerating modules, the services compartment will be located below the klystron gallery.

The detector and service caverns are connected to one another by an escape tunnel that leads to a safe zone in each of the caverns. The service cavern is accessible via a shaft with 12 m internal diameter. Figure 35(b) provides a view of the interaction region and the service cavern.

CERN site. The most demanding aspects of transport and handling concern the installation of the underground equipment in both the two-beam and the klystron designs.

- Safety systems, access systems and radiation protection systems have been studied and are included in the schedules, cost and power estimates, covering all areas from injectors to beam-dumps. A hazard identification and mitigation analysis shows that fire protection is the dominant safety-related implementation issue.

The above studies, carried out by the CERN civil engineering and infrastructure groups, follow the standards used for other accelerator implementations and studies at CERN (e.g. HL-LHC, FCC). The standardisation applies to all items listed above, including their cost, power and schedule estimates.

5.1.2 Annual and integrated luminosities

Estimates of the integrated luminosities are based on an annual operational scenario [54]. After completion of CLIC commissioning, it is estimated that 185 days per year will be used for operation, with an average accelerator availability of 75%, thus yielding physics data taking during 1.2×10^7 seconds annually. The remaining time is shared between maintenance periods, technical stops and extended shut-downs as discussed in Section 5.4. The yearly luminosity and the cumulative integrated luminosity for the three stages of the CLIC programme are shown in Figure 50. A luminosity ramp-up of three years (10%, 30%, 60%) is assumed for the first stage and two years (25%, 75%) for subsequent stages. Prior to data-taking at the first stage, commissioning of the individual systems and one full year of commissioning with beam are foreseen. These are part of the construction schedule. The beam-polarisation scheme foreseen for the CLIC programme is described in Section 2.1.

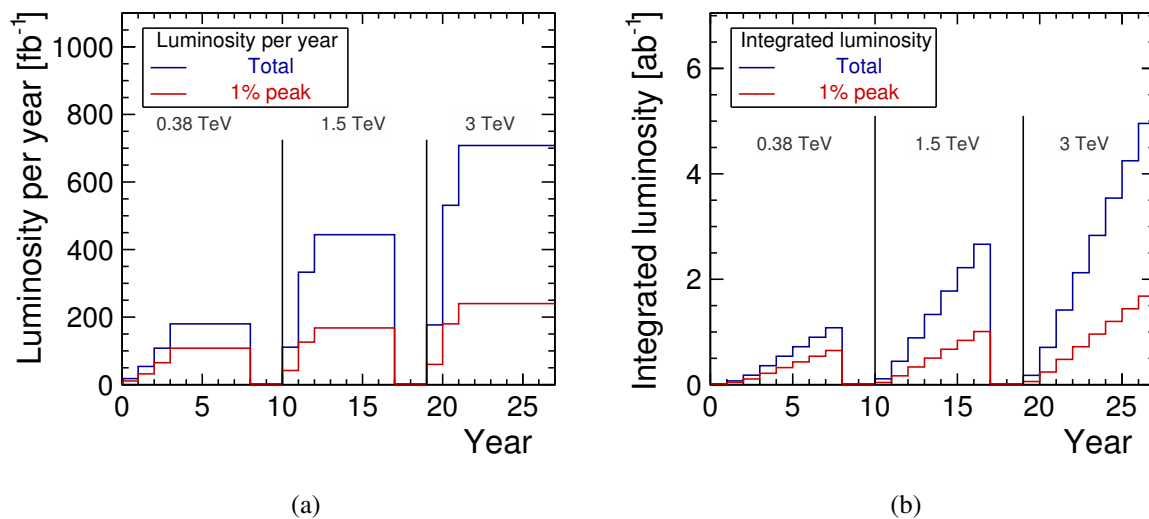


Figure 50: (a) Luminosity and (b) integrated luminosity per year in the proposed staging scenario, for the total luminosity in blue and the luminosity at centre-of-mass energies above 99% of the nominal centre-of-mass energy in red. Years are counted from the start of physics running. From [28].

5.2 Construction and operation schedules

The construction schedules presented in this section are based on the same methodologies as those used for the CLIC CDR [2]. Following input from equipment experts and the CERN civil engineering and

infrastructure groups, small adjustments were made to the construction and installation rates used for the schedule estimates. Details about the various parameters used can be found in [66]. The installation is followed by hardware commissioning, final alignment and commissioning with beam.

5.2.1 380 GeV drive-beam schedule

The schedule for the first stage of CLIC at 380 GeV, based on the drive-beam design, is shown in Figure 51. It comprises the following time-periods:

- Slightly more than five years for the excavation and tunnel lining, the installation of the tunnel infrastructures, and the accelerator equipment transport and installation.
- Eight months for the system commissioning, followed by two months for final alignment.
- One year for the accelerator commissioning with beam.

In parallel, time and resources are allocated for the construction of the drive-beam surface building, the combiner rings, damping rings, main-beam building and experimental areas, and their corresponding system installation and commissioning, as shown in Figure 51.

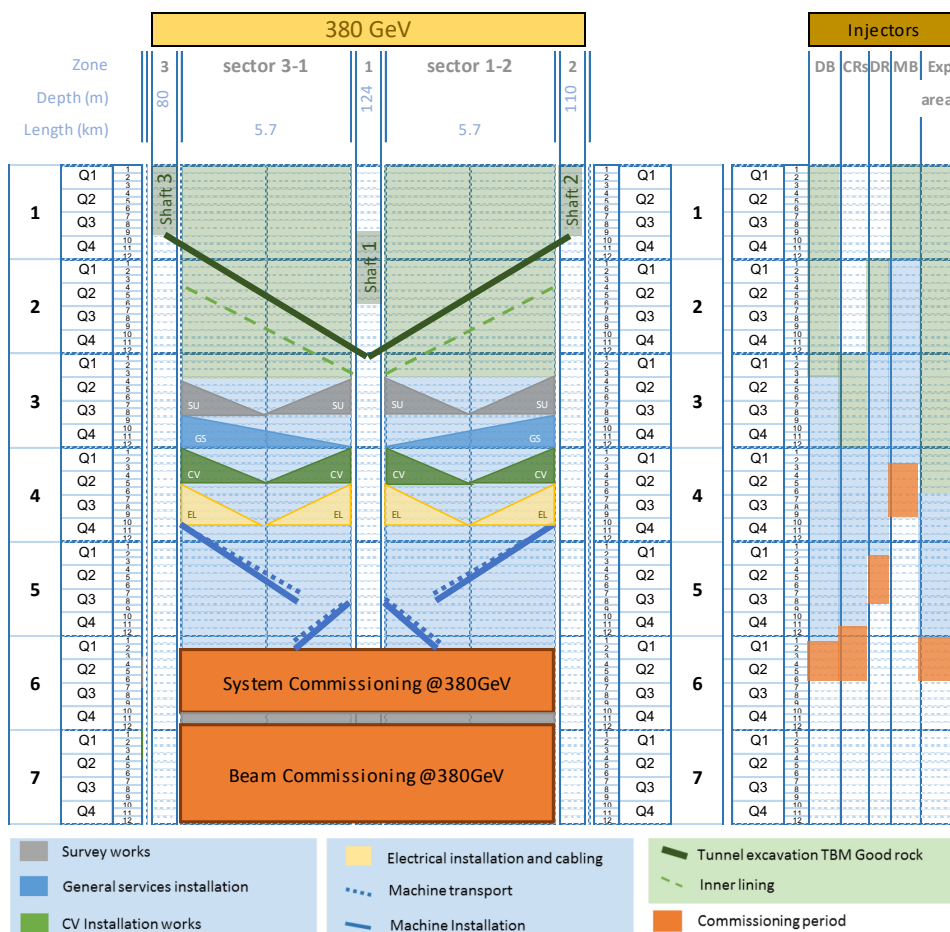


Figure 51: Construction and commissioning schedule for the 380 GeV drive-beam based CLIC facility. The vertical axis represents time in years. The abbreviations are introduced in Figure 14. (image credit: CLIC)

5.2.2 380 GeV klystron-driven schedule

In this scheme the RF power is provided by X-band klystrons and modulators, installed underground all along the main linac. The total time for installation is slightly different from the drive-beam case. The surface buildings and installations are reduced to those exclusively needed for the main beam and experimental area, reducing the surface construction activities correspondingly. On the other hand, the installation time in the main tunnel is longer, due to the RF units and the additional infrastructures required. Even though it is possible to work in parallel in the main linac tunnel and in the klystron gallery, the overall transport, installation and handling logistics are more time consuming. The time needed for construction, installation and commissioning is eight years, compared to seven years for the drive-beam option at the same CLIC energy of 380 GeV.

5.2.3 Schedules for the stages at higher energies and the complete project

In both cases discussed above, the 380 GeV collider is designed to be extended to higher energies. Most of the construction and installation work can be carried out in parallel with the data-taking at 380 GeV. However, it is estimated that a stop of two years in accelerator operation is needed between two energy stages. This time is needed to make the connection between the existing machine and its extensions, to reconfigure the modules used at the existing stage for their use at the next stage, to modify the beam-delivery system, to commission the new equipment and to commission the entire new accelerator complex with beam.

As the construction and installation of the 1.5 TeV and subsequent 3 TeV equipment cover periods of 4.5 years, the decision about the next higher energy stage needs to be taken after ~ 4 -5 years of data taking at the existing stage, based on physics results available at that time. The corresponding scenario is shown in Figure 52 for the drive-beam based scenario. A more detailed breakdown of the full project schedule can be found in [66]. The overall upgrade schedule is very similar for the case in which the first stage will be powered by klystrons.

In a schedule driven by technology and construction, the CLIC project would cover 34 years, counted from the start of construction. About 7 years are scheduled for initial construction and commissioning and a total of 27 years for data-taking at the three energy stages, which includes two 2-year intervals between the stages.

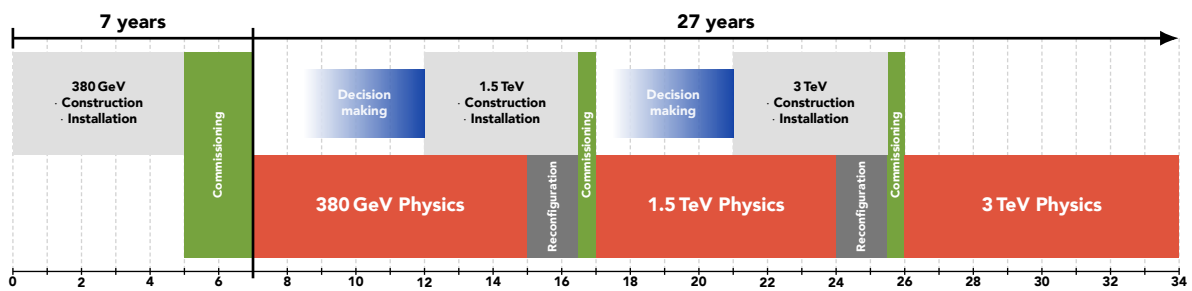


Figure 52: Technology-driven CLIC schedule, showing the construction and commissioning period and the three stages for data taking. The time needed for reconfiguration (connection, hardware commissioning) between the stages is also indicated. (image credit: CLIC)

5.2.4 Concluding remarks on the schedule

The schedule for construction and installation shows that the CLIC project can be implemented well in time for first collisions in 2035, provided it can be launched by 2026. The most critical CLIC technology-specific items driving the schedule are the main-beam module production and installation, as well as the RF units. The other schedule drivers, such as the tunnelling, the buildings and the infrastructures are more common, similar to other projects at CERN and elsewhere.

5.3 Cost estimate

For the cost estimate of CLIC the methodology used is the same as for previous CLIC cost estimates and the estimates of other projects, such as the LHC experiments and the Reference Design Report and Technical Design Report of the International Linear Collider (ILC) [154, 155]. Previous CLIC cost estimates were reported in the CLIC CDR [4] for two different implementation options at 500 GeV. An initial cost estimate for the first stage at 380 GeV was presented together with the introduction of the corresponding CLIC energy staging scenario in [5]. Since then, many CLIC optimisation studies have been undertaken with a particular focus on cost reduction, as reported in Section 3. The resulting cost estimates, as well as the methodologies and assumptions used have been presented in November 2018 to a cost review panel composed of international experts. After recommendations on minor issues by the review panel, the estimates have been updated accordingly. As the cost of the accelerator is significantly larger than the cost of the experiment, this Section focuses on the accelerator when presenting the methodologies and the various aspects of the outcome. The resulting estimated cost of the 380 GeV stage is presented, together with an estimate for upgrading to higher energies. The same tools and basic principles are applied for estimating the cost of the experiment, and the results are presented in Section 5.3.4.

5.3.1 Scope and method

CLIC is assumed to be a CERN-hosted project, constructed and operated within a collaborative framework with participation and contributions from many international partners. Contributions from the partners are likely to take different forms (e.g. in kind, in cash, in personnel, from different countries, in different currencies or accounting systems). Therefore a "value and explicit labour" methodology is applied. The value of a component or system is defined as the lowest reasonable estimate of the price of goods and services procured from industry on the world market in adequate quality and quantity and satisfying the specifications. Value is expressed in a given currency at a given time. Explicit labour is defined as the personnel provided for project construction by the central laboratory and the collaborating institutes, expressed in Full Time Equivalent (FTE) years. It does not include personnel in the industrial manufacturing premises, as this is included in the value estimate of the corresponding manufactured components. The personnel in industrial service contracts that are part of the accelerator construction, outside CERN or at CERN, are also accounted for in the value estimate of the corresponding items.

For the value estimate, a bottom-up approach is used, following the work breakdown structure of the project, starting from unit costs and quantities for components, and then moving up to technical systems, subdomains and domains. This allows accounting for all aspects of the production process and the application of learning curves for large series. For some parts (e.g. standard systems), cost scaling from similar items is used, implying that detailed knowledge on the work breakdown is not required, but rather estimators characterising the component.

The basic value estimate concerns the construction of the 380 GeV CLIC stage on a site close to CERN, where the 380 GeV stage of CLIC constitutes a project in itself. As a consequence, large-series effects expected on unit costs – learning curves and quantity rebates – remain limited to the quantities required for the completion of the 380 GeV stage. Estimates are provided both for the drive-beam

based and the klystron-based options, together with the corresponding incremental value for upgrading to higher energies.

The value estimates given cover the project construction phase, from approval to start of commissioning with beam. They include all the domains of the CLIC complex from injectors to beam dumps, together with the corresponding civil engineering and infrastructures. Items such as specific tooling required for the production of the components, reception tests and pre-conditioning of the components, and commissioning (without beam) of the technical systems, are included. On the other hand, items such as R&D, prototyping and pre-industrialisation costs, acquisition of land and underground rights-of-way, computing, and general laboratory infrastructures and services (e.g. offices, administration, purchasing and human resources management) are excluded. Spare parts are accounted for in the operations budget. The value estimate of procured items excludes VAT, duties and similar charges, taking into account the fiscal exemptions granted to CERN as an Intergovernmental Organisation.

The uncertainty objective for the final outcome is $\pm 25\%$. To this aim, uncertainties on individual items are grouped in two categories. The first one, *technical uncertainty*, relates to technological maturity and likelihood of evolution in design or configuration. The second category, *commercial uncertainty*, relates to uncertainty in commercial procurement. Based on a statistical analysis of LHC procurements this uncertainty is estimated as $50\%/n$, where n is the number of expected valid bids for each component [156].

The CLIC value estimates are expressed in Swiss franc (CHF) of December 2018. Consequently, individual entries are escalated in time according to appropriate indices, as published by the Swiss federal office of statistics. Furthermore, the following average exchange rates have been applied: 1 EUR=1.13 CHF, 1 CHF=1 USD, 1 CHF=114 JPY. More detailed information on the costing tool, on escalation and currency fluctuations, and on the individual cost uncertainty factors applied can be found in the CLIC project plan [66].

5.3.2 Value estimates and cost drivers

The breakdown of the resulting cost estimate up to the sub-domain level is presented in Table 8 for the 380 GeV stage of the accelerator complex, both for the baseline design with a drive beam and for the klystron-based option. Figure 53 illustrates the sharing of cost between different parts of the accelerator complex. The injectors for the main-beam and drive-beam production are among the most expensive parts of the project, together with the main linac, and the civil engineering and services.

Combining the estimated technical uncertainties yields a total (1σ) error of 1270 MCHF for the drive-beam based facility, and 1540 MCHF when using klystrons. In addition, the commercial uncertainties, defined above, need to be included. They amount to 740 MCHF and 940 MCHF for the drive-beam and klystron-based options, respectively. The total uncertainty is obtained by adding technical and commercial uncertainties in quadrature. Finally, for the estimated error band around the cost estimate, the resulting total uncertainty is used on the positive side, while only the technical uncertainty is used on the negative side [4]. The cost estimate for the first stage of CLIC including a 1σ overall uncertainty is therefore:

$$\begin{aligned} \text{CLIC 380 GeV drive-beam based} & : 5890_{-1270}^{+1470} \text{ MCHF} \quad ; \\ \text{CLIC 380 GeV klystron based} & : 7290_{-1540}^{+1800} \text{ MCHF} \quad . \end{aligned}$$

The difference between the drive-beam and klystron-based estimates is mainly due to the current cost estimates for the X-band klystrons and corresponding modulators. The increased diameter of the main linac tunnel, required to host the RF gallery in the klystron-based option, also contributes to the cost-difference. By reducing the X-band RF costs by 50% in the klystron option, the overall cost of the

Table 8: Cost breakdown for the 380 GeV stage of the CLIC accelerator, for the drive-beam baseline option and for the klystron option.

Domain	Sub-Domain	Cost [MCHF]	
		Drive-beam	Klystron
Main-Beam Production	Injectors	175	175
	Damping Rings	309	309
	Beam Transport	409	409
Drive-Beam Production	Injectors	584	—
	Frequency Multiplication	379	—
	Beam Transport	76	—
Main Linac Modules	Main Linac Modules	1329	895
	Post decelerators	37	—
Main Linac RF	Main Linac Xband RF	—	2788
Beam Delivery and Post Collision Lines	Beam Delivery Systems	52	52
	Final focus, Exp. Area	22	22
	Post-collision lines/dumps	47	47
Civil Engineering	Civil Engineering	1300	1479
Infrastructure and Services	Electrical distribution	243	243
	Survey and Alignment	194	147
	Cooling and ventilation	443	410
	Transport / installation	38	36
Machine Control, Protection and Safety systems	Safety systems	72	114
	Machine Control Infrastructure	146	131
	Machine Protection	14	8
	Access Safety & Control System	23	23
Total (rounded)		5890	7290

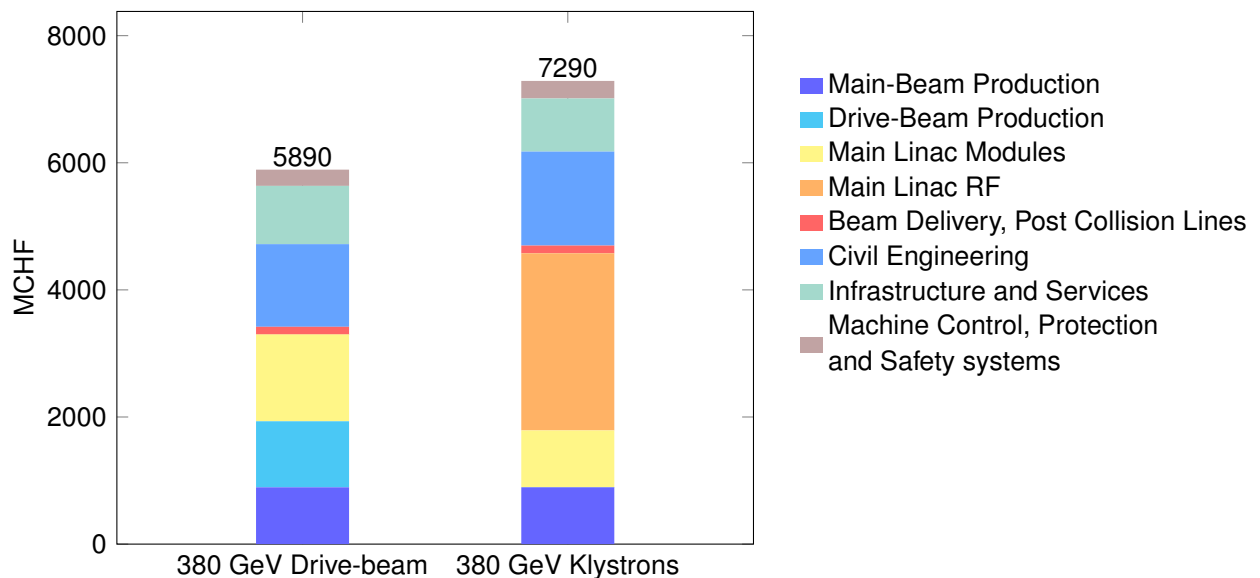


Figure 53: Cost breakdown for the 380 GeV stage of the CLIC accelerator, for the drive-beam baseline option and for the klystron option. (image credit: CLIC)

two options becomes similar. To achieve such a reduction would require a dedicated development programme together with industry for X-band klystrons and associated modulators. There is still room for possible gains through optimising the accelerating structure parameters, klystron design and luminosity performance. The cost of the klystron-based option is more affected by the luminosity specification than the drive-beam option.

The cost composition and values of the 1.5 TeV and 3 TeV stages have also been estimated. The energy upgrade to 1.5 TeV has a cost estimate of ~ 5.1 billion CHF, including the upgrade of the drive-beam RF power needed for the 1.5 TeV stage. In the case of expanding from a klystron-based initial stage this energy upgrade will be 25% more expensive. A further energy upgrade to 3 TeV has a cost estimate of ~ 7.3 billion CHF, including the construction of a second drive-beam complex.

The CLIC technical cost drivers have been identified, together with potential cost mitigation alternatives. These will be addressed in the next phase of the CLIC project as discussed in [Section 7](#). In general, further cost reduction studies will require close collaboration with industry. Beyond technical developments, optimal purchase models need to be defined, optimising the allocation of risks and production responsibilities between industry, CERN and collaboration partners in each case. In particular, the module production and RF units have a potential for cost reduction. For a klystron-based implementation, the cost reductions of the RF system are of crucial importance.

5.3.3 Labour estimates








A first estimate of the explicit labour needed for construction of the CLIC accelerator complex was obtained [4] by assuming a fixed ratio between personnel and material expenditure for projects of similar nature and size. Scaling with respect to the LHC - a CERN-hosted collider project of similar size to CLIC - provides a good estimator. Data from the LHC indicate that some 7000 FTE-years were needed for construction, for a material cost of 3690 MCHF (December 2010), corresponding to about 1.9 FTE-year/MCHF. About 40% of this labour was scientific and engineering personnel, and the remaining 60% worked on technical and project execution tasks.

In terms of complexity, the different CLIC sub-systems resemble the LHC case. Therefore, following the LHC approach outlined above, construction of the 380 GeV stage of the CLIC accelerator complex would require 11500 FTE-years of explicit labour. It is worth noting that this preliminary result is rather similar to the 1.8 FTE-year/MCHF derived for the ILC [155]. Although the RF technology differs between ILC and CLIC, the main elements of the accelerator complex are similar in the two projects.

5.3.4 Value estimate and cost drivers of the CLIC detector

The methodology used for estimating the cost of the CLIC detector [11] is similar to the one used for the accelerator complex, and is based on the detector work breakdown structure [157]. Some differences in the approach, given by the specificities of the detector, are detailed in the CDR [4]. A breakdown of the value estimate for the CLIC detector is given in [Table 9](#). The main cost driver is the cost of the silicon sensors for the 40-layer Electromagnetic Calorimeter (ECAL). For example, a 25% reduction in the cost of silicon per unit of surface would reduce the overall detector cost by more than 10%. Alternative designs for ECAL are feasible, but will reduce the detector performance (e.g. worse energy resolution for photons [11]).

Table 9: Cost estimate of the CLIC detector [157].

System	Cost fraction	Cost[MCHF]
Vertex		13
Silicon Tracker		43
Electromagnetic Calorimeter		180
Hadronic Calorimeter		39
Muon System		16
Coil and Yoke		95
Other		11
0 10% 20% 30% 40% 50%		
Total		397

5.3.5 Operation costs

A preliminary estimate of the CLIC accelerator operation cost, with focus on the most relevant elements, is presented here. The material cost for operation is approximated by taking the cost for spare parts as a percentage of the hardware cost of the maintainable components. These annual replacement costs are estimated at the level of:

- 1% for accelerator hardware parts (e.g. modules).
- 3% for the RF systems, taking the limited lifetime of these parts into account.
- 5% for cooling, ventilation, electronics and electrical infrastructures etc. (includes contract labour and consumables)

These replacement/operation costs represent 116 MCHF per year.

An important ingredient of the operation cost is the CLIC power consumption and the corresponding energy cost, which is discussed in [Section 5.4](#) below. This is difficult to evaluate in CHF units, as energy prices are likely to evolve. The expected energy consumption of the 380 GeV CLIC accelerator, operating at nominal luminosity, corresponds to 2/3 of CERN's current total energy consumption.

Concerning personnel needed for the operation of CLIC, one can assume efforts that are similar to large accelerator facilities operating today. Much experience was gained with operating Free Electron Laser linacs and light-sources with similar technologies. As CLIC is a normal-conducting accelerator operated at room temperature, one can assume that the complexity of the infrastructure, and therefore the maintenance efforts, compare favourably with other facilities. The maintenance programme for equipment in the klystron galleries is demanding, but is not expected to impact strongly on the overall personnel required for operation. The ILC project has made a detailed estimate of the personnel needed to operate ILC, yielding 640 FTE. This number includes scientific/engineering (40%), technical/junior level scientific staff (40%) and administrative staff (20%) for the operation phase [155, 158]. The difference between a 250 GeV and a 500 GeV ILC implementation was estimated to be 25%. In the framework of CERN, these numbers would distribute across scientific/engineering/technical staff, technical service contracts, fellows and administrative staff. The level of CLIC operational support required is expected to be similar to the ILC estimates.

Given the considerations listed above, one can conclude that operating CLIC is well within the resources deployed for operation at CERN today. Operating CLIC concurrently with other programmes at CERN is also technically possible. This includes LHC, as both accelerator complexes are independent. Building CLIC is not destructive with respect to the existing CERN accelerator complex. Electrical grid connections are also independent. The most significant limitation will therefore be the resources, in particular personnel and overall energy consumption.

5.4 Power and energy consumption

The nominal power consumption at the 380 GeV stage has been estimated based on the detailed CLIC work breakdown structure. This yields for the drive-beam option a total of 168 MW for all accelerator systems and services, taking into account network losses for transformation and distribution on site. The breakdown per domain in the CLIC complex (including experimental area and detector) and per technical system is shown in the left part of Figure 54. Most of the power is used in the drive-beam and main-beam injector complexes, comparatively little in the main linacs. Among the technical systems, the RF represents the major consumer. For the klystron-based version the total power consumption is very similar at 164 MW as shown in the right part of Figure 54.

These numbers are significantly reduced compared to earlier estimates due to optimisation of the injectors for 380 GeV, introducing optimised accelerating structures for this energy stage, significantly improving the RF efficiency, and consistently using the expected operational values instead of the full equipment capacity in the estimates. For the 1.5 and 3.0 TeV stages these improvements have not been studied in detail and the power estimates from the CDR are used [4].

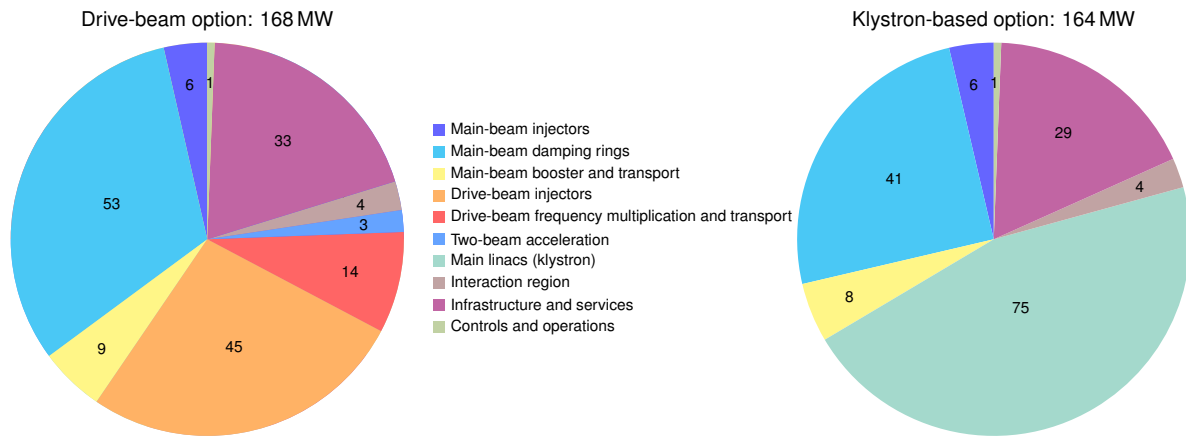


Figure 54: Breakdown of power consumption between different domains of the CLIC accelerator in MW at a centre-of-mass energy of 380 GeV, for the drive-beam option on the left and for the klystron option on the right. The contributions add up to a total of 164 MW and 168 MW in the two cases. (image credit: CLIC)

Table 10: Estimated power consumption of CLIC at the three centre-of-mass energy stages and for different operation modes. The 380 GeV numbers are for the drive-beam option and have been updated as described in Section 5.4, whereas the estimates for the higher energy stages are from [4].

Collision energy [GeV]	Running [MW]	Standby [MW]	Off [MW]
380	168	25	9
1500	364	38	13
3000	589	46	17

Table 10 shows the nominal power consumption in three different operation modes of CLIC, including the "running" mode at the different energy stages, as well as the residual values for two operational modes corresponding to short ("standby") and long ("off") beam interruptions. Intermediate power consumption modes exist, for example when a part of the complex is being tested, or during transitional

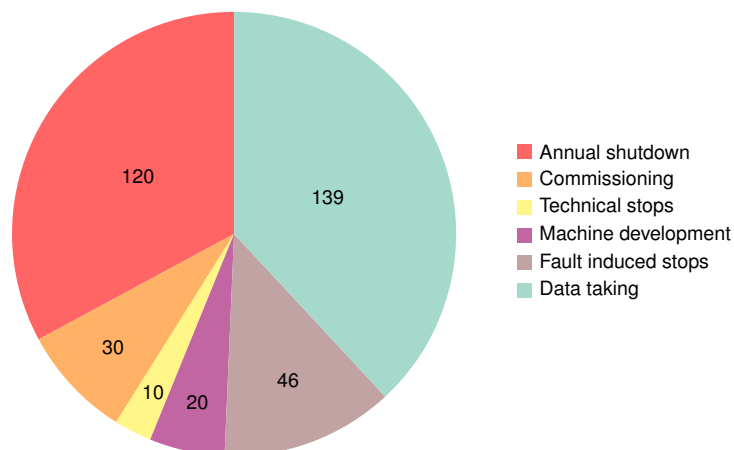


Figure 55: Operation schedule in a "normal" year (days/year). (image credit: CLIC)

states as waiting for beam with RF on. The contribution of these transitional states to the annual energy consumption is dealt with by averaging between "running" and "standby" for certain periods, as described below.

5.4.1 Energy consumption

Estimating the yearly energy consumption from the power numbers requires an operational scenario, which is detailed in [54] and depicted in Figure 55. In any "normal" year, i.e. once CLIC has been fully commissioned, the scenario assumes 120 days of annual shutdown, 30 days for beam-commissioning, and 30 days of scheduled maintenance, including machine development and technical stops (typically 1 day per week, or 2 days every second week). This leaves 185 days of operation for physics, for which 75% availability is assumed, i.e. 46 days of fault-induced stops. This results in 139 days, or 1.2×10^7 seconds, per year for physics data taking.

In terms of energy consumption the accelerator is assumed to be "off" during 120 days and "running" during 139 days. The power consumption during the remaining time, covering commissioning, technical stops, machine development and fault-induced stops is taken into account by estimating a 50/50 split between "running" and "standby". In addition, one has to take reduced operation into account in the first years at each energy stage to allow systematic tuning up of all parts of the accelerator complex. A luminosity ramp-up of three years (10%, 30%, 60%) in the first stage and two years (25%, 75%) in subsequent CLIC stages is considered. For the energy consumption estimate we change the corresponding reduction in "running" time to a 50/50 mixture of the two states mentioned above, resulting in a corresponding energy consumption ramp-up.

The evolution of the resulting electrical energy consumption over the years is illustrated in Figure 56. For comparison, CERN's current energy consumption is approximately 1.2 TWh per year, of which the accelerator complex uses around 90%.

5.4.2 Power reduction studies and future prospects

Since the CDR [2] in 2012 the CLIC collaboration has systematically explored power reduction and technical system optimisation across the complex. As a result the power estimate is reduced by around 35% for the initial stage. The main contributors to the reduced estimate are:

- The accelerating structures were optimised for 380 GeV and corresponding luminosity, impacting among others on RF power needs and the machine length. The optimisation was done for cost but

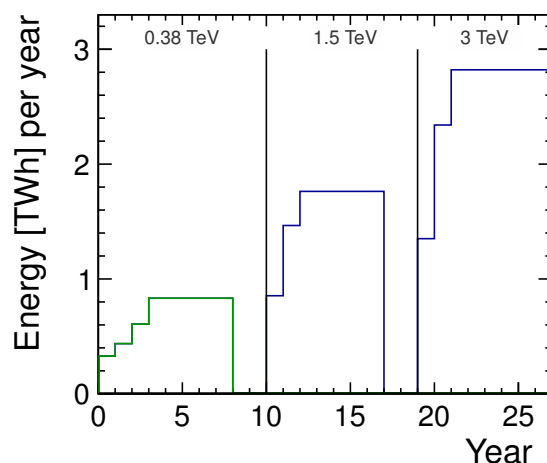


Figure 56: Estimated yearly energy consumption of CLIC. The initial stage estimate is revised in detail (green), while numbers for the higher energy stages are from [4] (blue). (image credit: CLIC)

it was also shown that cost and power are strongly correlated.

- The injector systems and drive-beam facility were optimised to the 380 GeV parameters taking into account R&D on various technical systems, for example reducing the number of drive-beam klystrons to around 60% of earlier designs.
- High efficiency klystron studies have reached a maturity such that 70% efficiency can be taken as the baseline.
- Permanent magnets can partly replace electromagnets.
- Nominal settings of RF systems, magnets and cooling have consistently been used, analysing the power consumption when running at full luminosity. This replaces earlier estimates which, in some cases, were based on maximum equipment capacity.

In summary, the estimate of the power consumption can be considered to be detailed and complete for the initial 380 GeV stage. The estimates for the higher energy stages have not been scrutinised in order to include the saving measures listed above. Also for the initial stage further work can lead to additional savings. This concerns in particular the damping ring RF power, where further studies are needed before a revised baseline can be introduced. The total power consumption of the damping rings (53 MW) is dominated by the RF system (45 MW). In the present design, the power efficiency of the RF system is rather low due to high peak power requirements for compensation of transient beam loading effects. Work is ongoing to improve the design and reduce the peak RF power requirements by introducing an optimum modulation of both phase and amplitude of the input RF signal. This may result in a significant (up to a factor of 2) reduction of the damping ring RF system power consumption, potentially reducing the overall damping ring power consumption to around 30 MW.

6 Future opportunities

A key advantage of a linear collider is the extendibility in energy. CLIC can provide electron-positron collisions with centre-of-mass energies of up to 3 TeV. The usage of novel approaches for an upgrade of CLIC might allow to reach even higher centre-of-mass energies. In the following section, the physics motivation and possible accelerator technologies for such an upgrade are introduced.

6.1 Physics motivation

An increase of the centre-of-mass energy beyond 3 TeV would enhance the physics potential even further beyond the capabilities of the baseline CLIC programme described in Section 2. The aim of such a collider would be direct and indirect searches for phenomena beyond the Standard Model. The discussion that follows focuses on the motivation for a 10 TeV electron-positron collider.

The centre-of-mass energy dependence in the range up to 30 TeV for many important Standard Model processes in electron-positron collisions is shown in Figure 57. Above the kinematic threshold, the cross sections for Higgsstrahlung and two-fermion production (e.g. $e^+e^- \rightarrow t\bar{t}$) scale as $1/s$. A similar energy dependence is visible for W-boson pair production. This is a first indication that the desired integrated luminosities at 10 TeV would exceed those for the baseline CLIC energy stages.

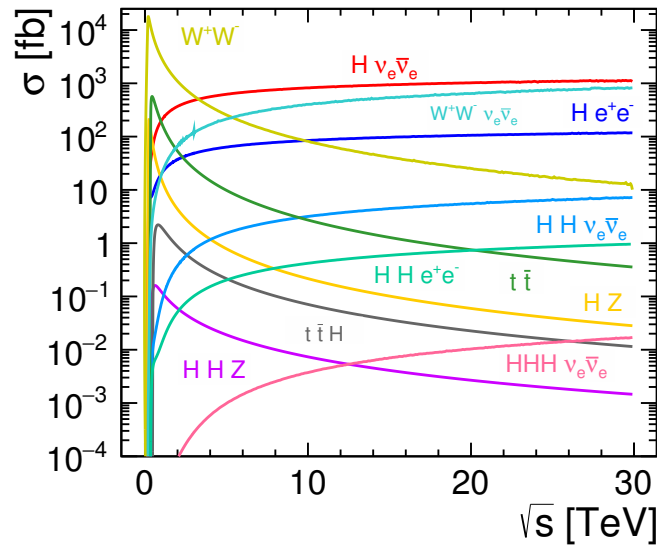


Figure 57: Cross section as a function of centre-of-mass energy for the main Standard Model processes at a very high-energy e^+e^- collider. The values shown correspond to unpolarised beams and include the effect of Initial State Radiation (ISR). (image credit: CLICdp)

On the other hand, the rate of events with final states produced in WW or ZZ boson fusion rises approximately as $\log(s)$. For example, the cross section of the dominant contribution to double-Higgs production, $e^+e^- \rightarrow HH\nu_e\nu_e$, is about a factor 4 larger at 10 TeV compared to 3 TeV. Although the dependence of the cross section on the Higgs self-coupling decreases somewhat with energy, a significant improvement of the knowledge of the Higgs self-coupling is expected for an integrated luminosity of a few ab^{-1} at 10 TeV. Even higher centre-of-mass energies of a few tens of TeV would also give access to triple Higgs production.

The indirect sensitivity to New Physics of Higgs and W^+W^- production is illustrated using Standard Model effective field theory (see also Section 2.4). In Figure 58(a) the sensitivities of the three

baseline energy stages of CLIC are compared to 4 ab^{-1} collected at a $10 \text{ TeV } e^+e^-$ collider. The sensitivities to the scales of four dimension-6 operator coefficients, defined as Λ/\sqrt{c} , are shown. The results are based on the fit described in [159], with the linear dependence on the coefficients now computed more accurately. The projections used as input are largely obtained from benchmark analyses based on full detector simulations [14]. The projections for 3 TeV are extrapolated to 10 TeV assuming that the shape of the beamstrahlung spectrum is the same for both energies. Generally, new physics scales well beyond the centre-of-mass energy of the collider can be probed. The 10 TeV stage enhances the reach for some operators by almost a factor 2 compared with 3 TeV. In particular, the measurement of the Higgsstrahlung cross section at the highest possible energy is important for the reach on $\bar{c}_W - \bar{c}_B$, \bar{c}_{HW} and \bar{c}_{HB} . The reach on \bar{c}_{3W} shown here decreases at higher energy due to helicity suppression of the linear interference term, but will also grow with energy at the quadratic level or if the interference is recovered by suitable differential measurements.

A very high-energy e^+e^- collider also provides unique opportunities for direct searches for new states. In Figure 58(b) the number of generic Higgsino (doublet of massive Dirac fermions with hypercharge 1/2) pair production events is shown as a function of the Higgsino mass for different assumptions on the integrated luminosity. Due to the absence of QCD backgrounds, e^+e^- collisions are especially suitable for the discovery of electroweak states. The number of events produced is independent of the Higgsino mass except very close to the kinematic threshold. Hence a discovery would be possible for masses of almost up to 5 TeV, which exceeds the capabilities of a hadron collider even with a centre-of-mass energy of the order of 100 TeV. A percent-level measurement of the Higgsino pair production cross section would typically be possible with an integrated luminosity of a few ab^{-1} .

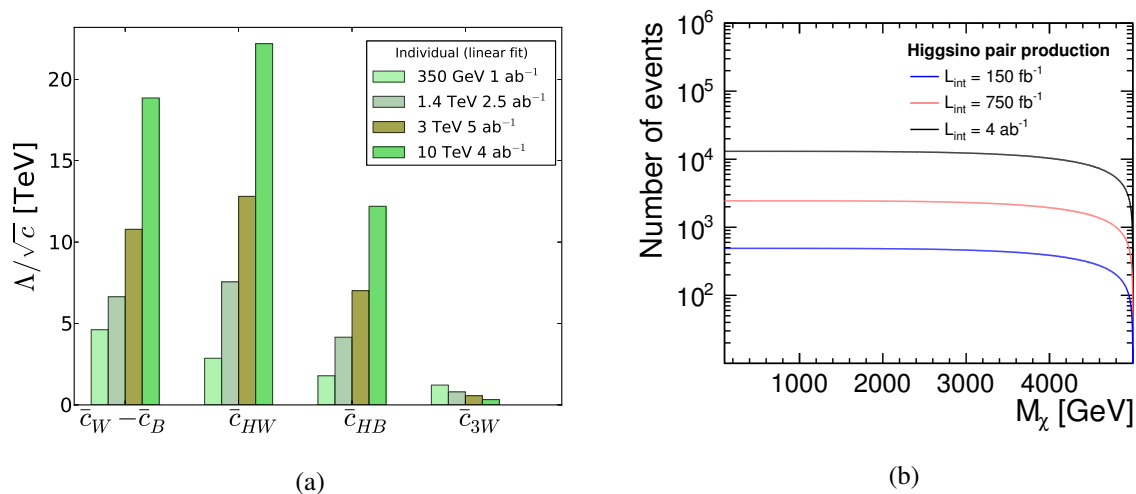


Figure 58: Examples for the New Physics potential of a $10 \text{ TeV } e^+e^-$ collider at $\sqrt{s} = 10 \text{ TeV}$. (a) Sensitivities of Higgs boson and W^+W^- production at 350 GeV, 1.4 TeV, 3 TeV and 10 TeV to the scales of various dimension-6 operator coefficients (based on [159]). (b) Number of Higgsino pair production events as a function of the Higgsino mass for three different assumptions on the integrated luminosity at $\sqrt{s} = 10 \text{ TeV}$ (image credit: CLICdp).

In conclusion, the sensitivity of an e^+e^- collider for new phenomena increases strongly with its centre-of-mass energy. A 10 TeV collider collecting an integrated luminosity of a few ab^{-1} would provide unique physics capabilities. This programme would be complementary to the baseline energy stages of CLIC.

Although the results shown in this section assume unpolarised beams, electron beam polarisation would enhance the capabilities of a 10 TeV collider in a similar way as for the baseline CLIC energy

stages. Left-handed electron beam polarisation would significantly enhance the cross sections for double Higgs and Higgsino production. Many indirect searches profit from precision measurements of polarisation asymmetries.

6.2 Opportunities for extension based on future technologies

CLIC technology is mature and can provide collision energies in the range of up to 3 TeV, at affordable cost at a site close to CERN. In the future, novel technologies may make it possible to extend the CLIC energy range, for example to 10 TeV. In particular, novel acceleration technologies could replace parts of CLIC technology in the main linacs in the future, even if they are currently not yet mature enough for collider applications. The two main relevant technologies are dielectric accelerating structures and acceleration using plasma. Both can either use a laser to produce the accelerating field or an electron beam. Also the use of protons is being investigated to produce high fields in a plasma [160], however no concept exists at this time for an electron-positron collider based on this technology.

These technologies must have high power efficiency and maintain excellent beam quality in order to achieve a luminosity at 10 TeV that is similar to the CLIC performance at 3 TeV. The corresponding studies are only beginning and important work is required before conclusions could be drawn on the feasibility of reaching the luminosity goals. However, the CLIC design work aims to ensure that the CLIC collider is consistent with upgrades using such technologies. Therefore a dedicated CLIC working group was established to ensure this goal. As the technologies are not mature, no detailed design can be made, and only a general compatibility can be ensured.

6.2.1 General concept

The proposed concepts for novel technology colliders consist of two linacs pointing at each other, similar to CLIC except for the technology used in the main accelerator.

The CLIC tunnels, hosting the main linac and BDS of each beam, are laser straight and cross at an angle of 20 mrad [161]. The crossing angle is optimal for collisions at 3 TeV, and is likely to be a good choice for higher energy collisions as well. The configuration avoids bent beam trajectories except what is required for the functionality of the beam delivery system. This important feature maintains the beam quality. Therefore all of the tunnels and corresponding infrastructures can continue to be used. This includes the main linacs, the beam delivery system, the detector hall and the post collision line.

As an example, if after the operation of the 1.5 TeV CLIC stage, the copper structures in the main linacs were replaced by dielectric or plasma-based acceleration with an effective gradient of 1 GV/m, one would be able to reach 10 TeV. The beam delivery system would certainly also need to be upgraded for this energy.

The single bunch parameters used by the novel concepts are similar to those for CLIC, with the exception of the laser-driven dielectric acceleration. Hence, one can expect that the CLIC injectors, which provide 9 GeV low emittance electron and positron beams, can be re-used. However, some modifications might be required to adapt to a time structure and bunch length optimised for the future technologies. The injectors are an important part of the overall cost at 380 GeV.

6.2.2 Dielectric accelerating structures

The dielectric structures are in principle hollow cylinders with a dielectric coating and are studied in different laboratories for RF frequencies ranging from X-band to THz [162].

A collaboration led by Argonne National Laboratory explores beam-driven X-band acceleration, i.e. a frequency very similar to CLIC. It might be possible that the gradient exceeds that of the current

CLIC technology and the structures are cheaper to fabricate. The concept is similar to the CLIC scheme and uses a drive beam to generate the RF power. Argonne and the CLIC collaboration are assessing the ultimate performance of this technology and the options to use it for CLIC energy upgrades.

One can imagine the following scenarios of using this technology in CLIC. If higher gradients can be reached at sufficient RF pulse lengths, CLIC components could be replaced in an existing main linac with higher gradient versions to increase the energy. Even if the technology does not reach higher performance but is cheaper, one can use it to reduce the cost of the energy upgrades. In these scenarios a large part or even all of the CLIC complex can be reused, including the drive beam, and the difference with the use of the current CLIC technology is very small. The luminosities and time structure are expected to be similar to the CLIC values.

If studies show that the RF pulse length would have an optimum significantly different from the current CLIC value, some effort is required to adapt the injectors and the drive-beam complex accordingly, but one can still expect to reuse the largest part of the collider.

Direct laser acceleration in silicon chips has been proposed – the “system on a chip” type technology [163]. The suggested beam parameters differ strongly from those of CLIC, and an assessment of a potential upgrade path is therefore challenging at this point. It might be that mainly the infrastructure could be reused.

6.2.3 Plasma-based acceleration

Beam-driven plasma wakefield accelerators (PWFA) use an electron drive beam to deplete a region of a plasma from electrons in order to generate strong electric fields that accelerate one bunch of the main beam. They have demonstrated very high gradients of more than 50 GV/m over almost a metre [164] and good efficiency for transferring power from the drive beam to the main beam of more than 30% [165]. A reasonable goal for the effective gradient, i.e. including the filling factor, is 1 GV/m [162]. A tentative proposed scheme can be found in [166].

To produce sufficient luminosity, the total beam current in plasma-based colliders must be of the same order of magnitude as in the CLIC case. The same holds for the bunch charge. Differently from CLIC, only single bunches are accelerated within each pulse. Therefore the time between subsequent collisions in the interaction point is much larger than the 0.5 ns in CLIC and rather of the order of 100 μ s. This might require some modifications of the main-beam generation complex but it is likely that a large part could be reused.

One can consider using the CLIC drive-beam complex to generate the high-power drive beams for the plasma acceleration. This might require additional return arcs, the rearrangement of the linac components, and potentially the replacement of the accelerating structures with modified versions. However, the costly RF power system can be reused fully. An example can be found in [167].

Laser-driven plasma wakefield accelerators [168] work in a similar fashion, except that a laser beam replaces the drive beam to generate the fields. So one can still anticipate that a similar fraction of the CLIC complex can be maintained except for the drive-beam complex.

While dielectric-based acceleration can be applied to electrons and positrons equally well, this is not necessarily the case for plasma-based acceleration. When the electron or laser drive beam passes the plasma, the electrons are expelled. The remaining positive ions focus an electron main beam but they defocus a positron main beam. Possible solutions to this problem are being studied, such as hollow plasmas or the acceleration of the positrons at a longitudinal location with a high density of electrons close to the centre. However, the validity of these solutions remains to be demonstrated and the electron and positron linacs might have important differences. An alternative approach that is being studied is to use electron beams in both linacs and convert them to very high energy photons with a laser. Depending on the exact parameter choices, the colliding photon beams would typically carry up to about 80% of the

original beam energy and reach luminosities that are comparable to the positron-electron options. The energy spectrum would be significantly broader. The CLIC interaction region design is compatible with housing a $\gamma\text{-}\gamma$ collider [169]. Another option that was considered is to use a conventional linac for the positrons and plasma acceleration for the electrons. In this case the positron energy might be lower than the electron energy, which is less interesting from a physics point of view. The gain in centre-of-mass energy would be compromised and the large event boost would pose additional demands on the detector.

6.2.4 Luminosity enabling technologies

High luminosity is key for high energy colliders and requires excellent beam quality. Studies of the beam quality are in their very early stages for the novel technologies, with the exception of the beam-driven dielectric acceleration. However, tolerances on alignment and stability of the beam and the components will be very tight in both the transverse and longitudinal planes, considerably exceeding the requirements for CLIC [170]. Whether these can be achieved is one of the main feasibility issues for collider studies based on novel technologies.

For CLIC, significant effort and resources have been put into developing technologies that address the beam quality. These include the demonstration of a system that can stabilise the CLIC final quadrupoles to the sub-nanometre scale [171, 172], the demonstration of phase feedback on the 50 fs level [47], the development of beam based alignment techniques [63, 173], and metrology and static alignment techniques [73]. The development of these new methods and precision tools in the context of CLIC are important steps towards the future use of novel acceleration technologies. In addition, the experience gained by the operation of CLIC will be the foundation for addressing the same issues at the even more challenging level required for novel acceleration technologies.

7 CLIC objectives for the period 2020–2025

7.1 Accelerator complex

The project implementation for CLIC foresees an initial five-year preparation phase prior to a construction start envisaged by 2026. The overall schedule towards first beams by 2035 is shown in Figure 59. This leaves a 2-year margin in addition to the construction and commissioning period estimated in the technology-driven schedule shown in Figure 52.

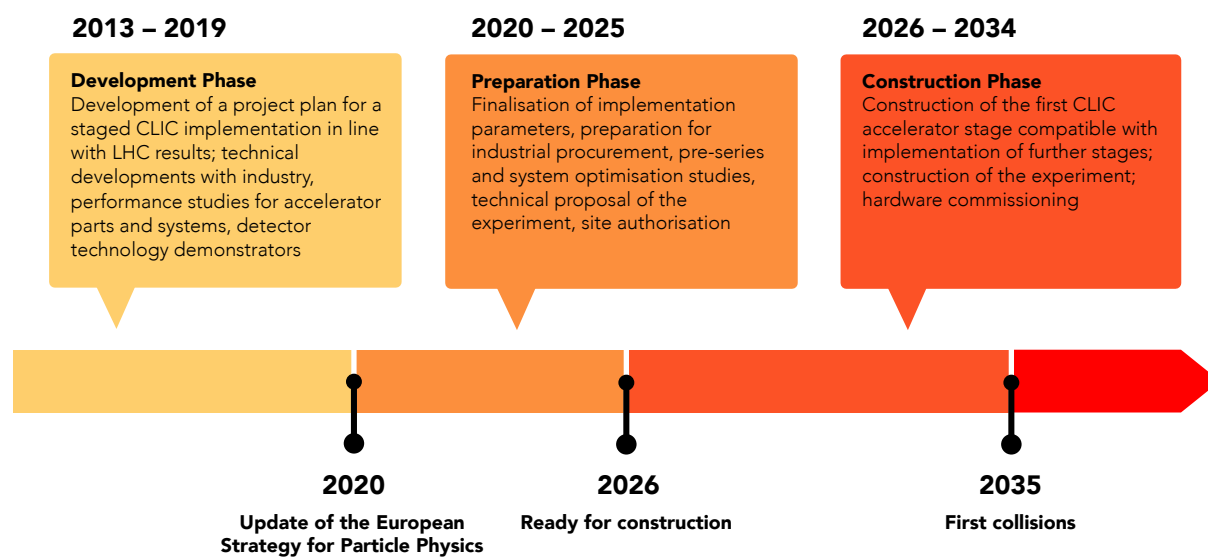


Figure 59: Schematic view of the CLIC implementation schedule, with first collisions in 2035. (image credit: CLIC)

In order to analyse the priorities for the preparation phase, the following project risks and mitigations have been considered:

- **Performance:** The dominant performance risk is related to the luminosity. Luminosity performance is based on technical performance and reliability as well as design robustness and system redundancy. Risk mitigation implies further studies at design and technical level, including on variation of parameters such as temperatures, mechanical instabilities and vibrations, magnetic fields, etc. Most importantly, performance validations in normal-conducting Free Electron Laser (FEL) Linacs and other compact linac systems will provide powerful demonstrations and new benchmarks for reliability, technical parameters, simulation and modelling tools on the timescale of 2020–2025.
- **Technical systems:** The main technical risks are related to RF sources, the X-band components, and overall system integration for the main linac. Reliable, efficient and cost-effective klystrons, modulators and X-band structures are components which are crucial for the machine. Additional thermo-mechanical engineering studies of the main linac tunnel, integrating all components, are important in order to further improve the understanding of the mechanical and thermal stability needed for CLIC. In addition, further system tests (beyond what has been achieved with CTF3) of the high-power drive beam would be most desirable.
- **Implementation:** Principal risks are associated with the industrial production of large numbers of modules and the civil engineering. Work during the preparation phase includes qualifying com-

panies for industrial production and optimising the work distribution and component integration. The module installation and conditioning procedures need to be refined and further verified. Cost control is crucial and is an integral part of these studies. This requires work on optimising the risk sharing models between industry, CERN and collaborative partners for the most critical and costly components. Detailed site-specific design work related to civil engineering and infrastructure needs to be performed.

7.1.1 Accelerator programme overview

To address these issues the forthcoming preparation phase will comprise further design, technical and industrial developments, with a focus on cost, power and risk reduction, in preparation for the Technical Design Report. System verifications in FEL linacs and low emittance rings will be increasingly important. The governance structure and the international collaboration agreements for the construction phase will be prepared during this time.

Civil engineering and infrastructure preparation will become increasingly detailed during the preparation phase. An environmental impact study and corresponding public enquiry will be needed as a prerequisite to authorisations for construction. Experience from the LEP and LHC projects indicates that approximately two years will be needed for such formal steps, as required by the procedures in the CERN host states.

The key elements of the CLIC accelerator activities during the period 2020–2025 are summarised in [Table 11](#).

7.1.2 Programme implementation, technology demonstrators and collaboration

The design studies and technical work for CLIC is broadly shared among the CLIC collaboration partners. The CLIC (accelerator) collaboration currently comprises 53 institutes from 31 countries [1].

The potential for collaborative projects is increasing with the current expansion in the field of Free Electron Laser (FEL) linacs and next-generation light sources. In particular, the increasing use of X-band technology, either as the main RF technology or for parts of the accelerators (deflectors, linearisers), is of high relevance for the next phase of CLIC. Construction, upgrades and operation of FEL linacs and conventional light sources, several of which are located at laboratories of CLIC collaboration partners, provide many opportunities for common design and component developments, and for acquiring crucial system test experience. Furthermore, the fact that there are significant resources invested in such accelerators world-wide, provides excellent opportunities for building up industrial capabilities and networks.

X-band RF systems and structure manufacturing used to be exclusively available in the US and Japan. However, today there are fourteen institutes capable of developing and testing X-band structures. All are working together on optimising the technology. The increasing number of qualified companies for accelerating structure manufacturing, together with the growing industrial availability of RF systems, make it easier for new groups to engage in these technologies. As a consequence, several smaller accelerators using X-band technology are in a proposal or technical preparation phase. In this context it is important to mention the SPARC 1 GeV X-band linac at INFN [174], a possible upgrade of CLARA at Daresbury [175] and the CompactLight [176] FEL study. The CompactLight design study is co-financed by the European Commission. It involves 24 partners preparing technical designs for compact FELs based on X-band linacs at energies ranging from 6 GeV down to small room-size systems for X-ray production through Inverse Compton Scattering (e.g. SmartLight [177]). Furthermore, the implementation of a 3.5 GeV X-band linac (eSPS) has been proposed [178] at CERN. It aims at injecting electrons into the SPS for further acceleration, and suggests implementing the linac during the period 2019–2024.

Table 11: Main CLIC accelerator objectives and activities in the next phase.

Activities	Purpose
Design and parameters	
Beam dynamics studies, parameter optimisation, cost, power, system verifications in linacs and low emittance rings	Luminosity performance and reduction of risk, cost and power
Main linac modules	
Construction of 10 prototype modules in qualified industries, two-beam and klystron versions, optimised design of the modules with their supporting infrastructure in the main linac tunnel	Final technical design, qualification of industrial partners, production models, performance verification
Accelerating structures	
Production of ~ 50 accelerating structures, including structures for the modules above	Industrialisation, manufacturing and cost optimisation, conditioning studies in test-stands
Operating X-band test-stands, high efficiency RF studies	
Operation of X-band RF test-stands at CERN and in collaborating institutes for structure and component optimisation, further development of cost-optimised high efficiency klystrons	Building experience and capacity for X-band components and structure testing, validation and optimisation of these components, cost reduction and increased industrial availability of high efficiency RF units
Other technical components	
Magnets, instrumentation, alignment, stability, vacuum	Luminosity performance, costs and power, industrialisation
Drive-beam studies	
Drive-beam front-end optimisation and system tests to ~ 20 MeV	Verification of the most critical parts of the drive-beam concept, further development of industrial capabilities for L-band RF systems
Civil Engineering, siting, infrastructure	
Detailed site specific technical designs, site preparation, environmental impact study and corresponding procedures in preparation for construction	Preparation for civil engineering works, obtaining all needed permits, preparation of technical documentation, tenders and commercial documents

The growing use of CLIC technology allows for implementing several of the CLIC project activities described in Table 11 in the form of collaborative projects together with the projects and technology partners mentioned above. Nevertheless, the principal ingredient to a successful preparation phase for CLIC, and the ability to team up with such partner projects, is an increase in resources for CLIC at CERN.

7.2 Detector and physics

Until now the CLIC detector and physics studies have essentially covered two phases. Work towards the CDR (2009–2012) focused on understanding the CLIC physics potential, mostly still without input from LHC data, and the experimental conditions at CLIC. Two ILC detector concepts were adapted to CLIC conditions. Physics studies using these detectors confirmed that CLIC delivers high-precision measurements, despite the luminosity spectrum and the presence of significant beam-induced background.

These studies also led to understanding the detailed detector performance requirements, as described in [Section 4](#). During the period 2013–2018 the focus of the studies changed. In addition to ongoing Linear Collider detector technology R&D, well adapted to CLIC in the domain of calorimetry, CLIC-specific detector R&D is being performed in the areas of silicon vertex and tracker R&D, power pulsing and low-mass cooling, as reported in [Section 4.4](#). The R&D currently aims principally for validated "technology demonstrators", rather than full prototypes. Detector simulation studies have led to a single optimised CLIC detector concept together with improved software tools for simulation and event reconstruction (see [Sections 4.3](#) and [4.5](#)). Physics studies have followed the evolution of the physics landscape, resulting in a focus on Higgs studies, top-quark studies and the assessment of the CLIC potential for new physics in a context where LHC has not yet identified any clear BSM signals and where the scope for theoretical interpretations is still very large (see [Section 2](#)).

If CLIC prepares for construction to start by 2026, the extent of the detector activities will need to increase significantly. While, owing to limited resources, technology developments currently focus only on the most challenging detectors, in the next phase all aspects of the experiment need to be addressed. Investments and priorities will be driven by time considerations, according to estimated lead times for the R&D, prototyping, and industrialisation, and taking detector construction schedules into account. For example, general infrastructures, large supporting structures, magnet yoke and magnet coils have to be installed early, followed by the calorimeters, the muon detectors and finally the inner tracking system. Therefore, the vertex and tracking detectors, the readout electronics, the data transmission and computing facilities can still profit from future technology advances, while the design and technologies for the superconducting solenoid coil have to be frozen earlier.

The main areas of activity for the period 2020–2025 will therefore comprise:

- Detector engineering, detector integration and technical coordination (including assembly and maintenance scenarios, services, general infrastructures, safety aspects, industrialisation, schedules, costing, etc.);
- Superconducting solenoid design (including demonstrators of the various technology aspects and subsequent industrialisation);
- Electromagnetic, hadronic and forward calorimeters (design to CLIC specifications, corresponding demonstrators and full prototypes, industrialisation aspects);
- Muon detectors (design to CLIC specifications and corresponding demonstrators);
- Vertex and tracking detectors (technology development, demonstrators, full modules, full design).

These sub-detector projects will include the corresponding on-detector and off-detector electronics developments and data-transmission studies. Physics studies will continue in parallel, while the development and deployment of software tools will remain in pace with the needs of the project phase.

In line with the level of objectives, the CLICdp collaboration (currently 30 institutes from 18 countries [1]) will grow significantly and its structure will evolve accordingly, incorporating the necessary legal and organisational frameworks for agreements on formal commitments and sharing of deliverables.

8 Summary

In this document, the research and development on the Compact Linear Collider is summarised, with emphasis on recent studies and R&D for the CLIC accelerator complex, improvements to the CLIC detector concept, and developments in the domain of the CLIC physics potential. CLIC is foreseen to be built and operated in stages. This report provides details of an updated staging scenario, which is optimised for physics performance, and contains assumptions about commissioning and running time per year which were recently harmonised with those of other future CERN projects. For the first stage with a centre-of-mass energy of $\sqrt{s} = 380\text{ GeV}$ an integrated luminosity of 1 ab^{-1} is foreseen. This is followed by operation at 1.5 TeV with 2.5 ab^{-1} , and by a third stage at 3 TeV with 5 ab^{-1} integrated luminosity. This CLIC physics programme spans over 25–30 years. The updated baseline also specifies $\pm 80\%$ electron polarisation, with the sharing between the two longitudinal polarisation states optimised for the best physics reach at each energy stage.

The construction and operation of CLIC is described, with the two-beam acceleration scheme as baseline scenario. Normal-conducting high-gradient 12 GHz accelerating structures are powered via a high-current drive beam. The accelerating structures will be operated in the range of 70 to 100 MV/m , resulting in a total accelerator length of 11 km for the 380 GeV stage and 50 km for 3 TeV . For the first energy stage, an alternative scenario is presented, with X-band klystrons powering the main-beam accelerating structures. Details of an implementation of CLIC near CERN are described, generally with emphasis on the 380 GeV stage. These include results on civil engineering studies, construction and upgrade schedules, electrical networks, cooling and ventilation, transport and safety aspects.

Beam experiments and hardware tests described in this report demonstrate that the CLIC performance goals can be met. For instance, accelerating gradients of up to 145 MV/m are reached with the two-beam concept at CTF3, and breakdown rates of the accelerating structures well below the limit of $3 \times 10^7\text{ m}^{-1}$ are stably achieved at X-band test platforms. High luminosities can be achieved by using nanometre beam sizes. This requires low-emittance beams as well as novel alignment and stabilisation techniques. There is substantial progress in all of these domains: performances as needed for the CLIC damping rings are achieved by modern synchrotron light sources; special alignment procedures for the main linac are now available; sub-nanometre stabilisation of the final focus quadrupoles is demonstrated. In general, beam physics studies, technical developments and system tests for CLIC resulted in significant progress in recent years. Reductions in cost and energy consumption have been among the main objectives of these developments, resulting in a better energy efficiency of the 380 GeV stage, with power around 170 MW , together with a lower estimated cost, now around 6 billion CHF .

The CLIC detector layout and the technology choices for the different sub-detectors are described in this report. The detector characteristics are driven by the CLIC physics programme and by the experimental conditions at CLIC. CLIC detector simulation studies have led to a new, optimised CLIC detector concept CLICdet, using an improved software suite for event simulation and reconstruction. CLICdet is optimised for particle flow with a light-weight vertex and tracking system, highly-granular calorimeter systems, a 4 T solenoid and a return yoke equipped with detectors for muon identification. CLICdet also has very forward calorimeters for luminosity measurements and forward electron tagging. Due to the beam structure of CLIC with a very low duty cycle below 0.001% , triggerless readout can be applied, and it is possible to operate the sub-detectors with power pulsing and with cooling concepts optimised for very small material budgets.

Detector R&D activities have validated technology demonstrators for vertex and tracking detectors as well as for the foreseen calorimeter concepts. The calorimeter R&D for CLIC is pursued within the CALICE and FCAL collaborations. Synergies in detector R&D with other projects are exploited, such as with the HL-LHC detector upgrades. The validation of the detector technology includes laboratory measurements and test beam experiments. In addition to tests targeting detector performance parameters,

such as the energy or position resolution, the powering and cooling concepts were validated. Concepts of ultra-light mechanical support structures and assembly procedures have been established and studied.

The physics potential of CLIC is assessed through full detector simulation studies of benchmark physics processes, using the CLIC detector including beam-induced backgrounds. In parallel, dedicated phenomenological studies using parameterised detector performance are being pursued. Results from both full and fast simulation studies are reported. It is shown that the initial stage of CLIC at 380 GeV gives access to precision measurements of the Standard Model Higgs boson and the top quark. To this end the first stage also foresees a top-quark pair-production threshold scan around 350 GeV. The second stage at 1.5 TeV opens more Higgs channels including $t\bar{t}H$, double-Higgs production, and rare decays, and allows direct sensitivity to many BSM models. The third stage at 3 TeV gives the best sensitivity to new physics and double-Higgs production through Higgs self-coupling.

CLIC accelerator technology has reached a mature state and is increasingly being put to use in accelerator projects around the globe. A detector design concept exists, and technology demonstrators for the sub-detectors have been built. A work-plan for the preparation phase towards building CLIC is outlined in this report. The CLIC accelerator and detector can be ready for a construction start around 2026. First collisions at the 380 GeV energy stage would then take place towards 2035. CLIC provides excellent sensitivity to Beyond-Standard-Model physics effects, through direct searches and via a broad set of precision Standard Model physics measurements that reach well beyond the projections for HL-LHC. In summary, CLIC represents a compelling opportunity for the post-LHC era.

Acknowledgements

This work benefited from services provided by the ILC Virtual Organisation, supported by the national resource providers of the EGI Federation. This research was done using resources provided by the Open Science Grid, which is supported by the National Science Foundation and the U.S. Department of Energy's Office of Science. This work was supported by the European Union's Horizon 2020 Research and Innovation programme under Grant Agreement No. 654168 (AIDA-2020); the European Union's Horizon 2020 Research and Innovation programme under Grant Agreement No. 777431 (CompactLight); the European Union's Horizon 2020 Marie Skłodowska-Curie Research and Innovation Staff Exchange programme under Grant Agreement No. 645479 (E-JADE); the National Commission for Scientific and Technological Research (CONICYT), Chile; the DFG cluster of excellence "Origin and Structure of the Universe", Germany; the Federal Ministry of Education and Research (BMBF), Germany under Grant Agreement No. 05H18VKRD1; the Israel Science Foundation (ISF); the I-CORE Program, Israel; the Israel Academy of Sciences; the Programma per Giovani Ricercatori "Rita Levi Montalcini" of the Ministero dell'Istruzione, dell'Università e della Ricerca (MIUR), Italy; the Research Council of Norway; the National Science Centre, Poland, HARMONIA project under contract UMO-2015/18/M/ST2/00518 and OPUS project under contract UMO-2017/25/B/ST2/00496; the Polish Ministry of Science and Higher Education under contract No. 3501/H2020/2016/2 and 3812/H2020/2017/2; the Ministry of Education, Science and Technological Development of the Republic of Serbia under contract No. OI171012; the Spanish Ministry of Economy, Industry and Competitiveness under projects MINEICO/FEDER-UE, FPA2015-65652-C4-3-R, FPA2015-71292-C2-1-P and FPA2015-71956-REDT; the Generalitat Valenciana under grant PROMETEO/2018/060, Spain; the IFIC, IFCA, IFT and CIEMAT grants under the Centro de Excelencia Severo Ochoa and Maria de Maeztu programs, SEV-2014-0398, MDM-2017-0765, SEV-2016-059, MDM-2015-0509, Spain; the Swedish Research Council; the Swiss National Science Foundation FLARE and FORCE grants 147463, 141146, 135012, 131428, 125272 and 126838; the Scientific and Technological Research Council of Turkey (TUBITAK) under grant number 118F333; the UK Science and Technology Facilities Council (STFC), United Kingdom; and the U.S. Department of Energy, Office of Science under contract DE-AC02-06CH11357.

References

- [1] *Compact Linear Collider (CLIC)*, last accessed 14 December 2018, URL: https://web.archive.org/web/*/http://clic.cern/.
- [2] M. Aicheler et al., eds., *A Multi-TeV Linear Collider Based on CLIC Technology: CLIC Conceptual Design Report*, CERN-2012-007, 2012, DOI: 10.5170/CERN-2012-007.
- [3] L. Linssen et al., eds., *CLIC Conceptual Design Report: Physics and Detectors at CLIC*, CERN-2012-003, 2012, DOI: 10.5170/CERN-2012-003.
- [4] P. Lebrun et al., eds., *CLIC Conceptual Design Report: The CLIC Programme: Towards a Staged e^+e^- Linear Collider Exploring the Terascale*, CERN-2012-005, 2012, DOI: 10.5170/CERN-2012-005.
- [5] P. N. Burrows et al., eds., *Updated baseline for a staged Compact Linear Collider*, CERN-2016-004, 2016, DOI: 10.5170/CERN-2016-004.
- [6] G. Geschonke, A. Ghigo, *CTF3 Design Report*, CERN-PS-2002-008-RF, CTF-3-NOTE-2002-047, LNF-2002-008-IR, 2002, URL: <https://cds.cern.ch/record/559331>.
- [7] S. Kuroda, ATF2 Collaboration, *ATF2 for Final Focus Test Beam for Future Linear Colliders*, Nucl. Part. Phys. Proc. **273-275** (2016) 225, DOI: 10.1016/j.nuclphysbps.2015.09.030.
- [8] T. Okugi, *Achievement of small beam size at ATF2 beamline*, Proceedings of LINAC 2016, East Lansing, MI, USA, 2016, MO3A02, DOI: 10.18429/JACoW-LINAC2016-MO3A02.
- [9] *FACET Facility for Advanced Accelerator Experimental Tests*, last accessed 14 December 2018, URL: https://web.archive.org/web/*/http://portal.slac.stanford.edu/sites/ard_public/facet/Pages/default.aspx.
- [10] *FERMI Free Electron laser Radiation for Multidisciplinary Investigations*, last accessed 14 December 2018, URL: https://web.archive.org/web/*/https://www.elettra.trieste.it/lightsources/fermi.html.
- [11] N. Alipour Tehrani et al., *CLICdet: The post-CDR CLIC detector model*, CLICdp-Note-2017-001, 2017, URL: <https://cds.cern.ch/record/2254048>.
- [12] D. Arominski et al., *A detector for CLIC: main parameters and performance*, CLICdp-Note-2018-005, 2018, URL: <http://cds.cern.ch/record/2649437>.
- [13] D. Dannheim et al., eds., *Detector Technologies for CLIC*, CERN, 2018, URL: <https://edms.cern.ch/document/2053288/>.
- [14] H. Abramowicz et al., CLICdp Collaboration, *Higgs physics at the CLIC electron-positron linear collider*, Eur. Phys. J. **C77** (2017) 475, DOI: 10.1140/epjc/s10052-017-4968-5.
- [15] H. Abramowicz et al., CLICdp Collaboration, *Top-Quark Physics at the CLIC Electron-Positron Linear Collider* (2018), arXiv: 1807.02441 [hep-ex].
- [16] J. de Blas et al., eds., *The CLIC Potential for New Physics*, CERN-2018-009-M, 2018, DOI: 10.23731/CYRM-2018-003.

- [17] P. Mora de Freitas, H. Videau, *Detector simulation with MOKKA / GEANT4: Present and future*, Proceedings of LCWS 2002, Seogwipo, Jeju Island, Korea, 2002, p. 623, DOI: [10.5281/zenodo.1744997](https://doi.org/10.5281/zenodo.1744997).
- [18] N. Graf, J. McCormick, *Simulator For The Linear Collider (SLIC): A Tool For ILC Detector Simulations*, AIP Conf. Proc. **867** (2006) 503, DOI: [10.1063/1.2396991](https://doi.org/10.1063/1.2396991).
- [19] F. Gaede, *Marlin and LCCD – Software tools for the ILC*, Nucl. Instrum. Meth. **A559** (2006) 177, DOI: [10.1016/j.nima.2005.11.138](https://doi.org/10.1016/j.nima.2005.11.138).
- [20] N. A. Graf, *org.lcsim: Event Reconstruction in Java*, J. Phys. Conf. Ser. **331** (2011) 032012, DOI: [10.1088/1742-6596/331/3/032012](https://doi.org/10.1088/1742-6596/331/3/032012).
- [21] M. A. Thomson, *Particle flow calorimetry and the PandoraPFA algorithm*, Nucl. Instrum. Meth. **A611** (2009) 25, DOI: [10.1016/j.nima.2009.09.009](https://doi.org/10.1016/j.nima.2009.09.009).
- [22] J. S. Marshall, M. A. Thomson, *The Pandora Particle Flow Algorithm*, Proceedings of CHEF 2013, Paris, France, 2013, p. 305, arXiv: [1308.4537](https://arxiv.org/abs/1308.4537) [physics.ins-det].
- [23] J. Marshall, A. Münnich, M. Thomson, *Performance of particle flow calorimetry at CLIC*, Nucl. Instrum. Meth. **A700** (2013) 153, DOI: [10.1016/j.nima.2012.10.038](https://doi.org/10.1016/j.nima.2012.10.038).
- [24] J. Marshall, M. Thomson, *The Pandora software development kit for pattern recognition*, Eur.Phys.J. **C75** (2015) 439, DOI: [10.1140/epjc/s10052-015-3659-3](https://doi.org/10.1140/epjc/s10052-015-3659-3).
- [25] T. Suehara, T. Tanabe, *LCFIPlus: A framework for jet analysis in linear collider studies*, Nucl. Instrum. Meth. **A808** (2016) 109, DOI: [10.1016/j.nima.2015.11.054](https://doi.org/10.1016/j.nima.2015.11.054).
- [26] J. de Favereau et al., DELPHES 3 Collaboration, *DELPHES 3, A modular framework for fast simulation of a generic collider experiment*, JHEP **02** (2014) 057, DOI: [10.1007/JHEP02\(2014\)057](https://doi.org/10.1007/JHEP02(2014)057).
- [27] U. Schnoor, P. Roloff, *A Delphes card for the CLIC detector*, CLICdp-Note-2018-007, 2018, URL: <http://cds.cern.ch/record/2649439>.
- [28] P. G. Roloff, A. Robson, *Updated CLIC luminosity staging baseline and Higgs coupling prospects*, CLICdp-Note-2018-002, 2018, URL: <https://cds.cern.ch/record/2645352>.
- [29] M. Thomson, *Model-independent measurement of the $e^+e^- \rightarrow HZ$ cross section at a future e^+e^- linear collider using hadronic Z decays*, Eur. Phys. J. **C76** (2016) 72, DOI: [10.1140/epjc/s10052-016-3911-5](https://doi.org/10.1140/epjc/s10052-016-3911-5).
- [30] The CMS Collaboration, *Sensitivity projections for Higgs boson properties measurements at the HL-LHC*, CMS PAS FTR-18-011, 2018, URL: <https://cds.cern.ch/record/2647699>.
- [31] P. Roloff et al., *Double Higgs boson production and Higgs self-coupling extraction at CLIC*, CLICdp-Note-2018-006, 2019, arXiv: [1901.05897](https://arxiv.org/abs/1901.05897) [hep-ex].
- [32] D. E. Kaplan et al., *Top Tagging: A Method for Identifying Boosted Hadronically Decaying Top Quarks*, Phys. Rev. Lett. **101** (2008) 142001, DOI: [10.1103/PhysRevLett.101.142001](https://doi.org/10.1103/PhysRevLett.101.142001).
- [33] D. Atwood, A. Soni, *Analysis for magnetic moment and electric dipole moment form-factors of the top quark via $e^+e^- \rightarrow t\bar{t}$* , Phys. Rev. **D45** (1992) 2405, DOI: [10.1103/PhysRevD.45.2405](https://doi.org/10.1103/PhysRevD.45.2405).

- [34] B. Grzadkowski, Z. Hioki, *Optimal-observable analysis of the angular and energy distributions for top-quark decay products at polarized linear colliders*, Nucl. Phys. **B585** (2000), [Erratum: Nucl. Phys. **B894**, 585(2015)] 3, DOI: [10.1016/S0550-3213\(00\)00385-0](https://doi.org/10.1016/S0550-3213(00)00385-0).
- [35] P. Janot, *Top-quark electroweak couplings at the FCC-ee*, JHEP **04** (2015) 182, DOI: [10.1007/JHEP04\(2015\)182](https://doi.org/10.1007/JHEP04(2015)182).
- [36] P. H. Kiem et al., *Probing New Physics using top quark polarization in the $e^+e^- \rightarrow t\bar{t}$ process at future Linear Colliders*, 2015, arXiv: [1503.04247](https://arxiv.org/abs/1503.04247) [hep-ph].
- [37] R. M. Godbole et al., *Model-independent analysis of Higgs spin and CP properties in the process $e^+e^- \rightarrow t\bar{t}\Phi$* , Eur. Phys. J. **C71** (2011) 1681, DOI: [10.1140/epjc/s10052-011-1681-7](https://doi.org/10.1140/epjc/s10052-011-1681-7).
- [38] G. Durieux, O. Matsedonskyi, *The top-quark window on compositeness at future lepton colliders*, JHEP **01** (2019) 072, DOI: [10.1007/JHEP01\(2019\)072](https://doi.org/10.1007/JHEP01(2019)072).
- [39] E. Accomando et al., *Physics at the CLIC Multi-TeV Linear Collider*, Proceedings of Hadron 2005, Rio de Janeiro, Brazil, 2004, arXiv: [hep-ph/0412251](https://arxiv.org/abs/hep-ph/0412251) [hep-ph].
- [40] S. Gori et al., *Higgs Physics at the HL-LHC and HE-LHC*, CERN-LPCC-2018-04, 2018, URL: <https://cds.cern.ch/record/2650162>.
- [41] D. Buttazzo et al., *Fusing Vectors into Scalars at High Energy Lepton Colliders*, JHEP **11** (2018) 144, DOI: [10.1007/JHEP11\(2018\)144](https://doi.org/10.1007/JHEP11(2018)144).
- [42] C. Frugiuele et al., *Relaxion and light (pseudo)scalars at the HL-LHC and lepton colliders*, JHEP **10** (2018) 151, DOI: [10.1007/JHEP10\(2018\)151](https://doi.org/10.1007/JHEP10(2018)151).
- [43] L. Di Luzio, R. Grober, G. Panico, *Probing new electroweak states via precision measurements at the LHC and future colliders* (2018), arXiv: [1810.10993](https://arxiv.org/abs/1810.10993) [hep-ph].
- [44] J. M. No, M. Spannowsky, *Signs of heavy Higgs bosons at CLIC: An e^+e^- road to the Electroweak Phase Transition* (2018), arXiv: [1807.04284](https://arxiv.org/abs/1807.04284) [hep-ph].
- [45] D. Schulte, R. Tomas, *Dynamic Effects in the New CLIC Main Linac*, Proceedings of PAC 2009, Vancouver, BC, Canada, 2009, p. 3811, URL: <http://accelconf.web.cern.ch/accelconf/PAC2009/papers/th6pfp046.pdf>.
- [46] C. Gohil, P. N. Burrows, D. Schulte, *Integrated Simulation of Dynamic Effects for the 380 GeV CLIC Design*, CLIC-Note-1138, 2018, URL: <https://edms.cern.ch/document/2053401/>.
- [47] J. Roberts et al., *Stabilization of the arrival time of a relativistic electron beam to the 50 fs level*, Phys. Rev. Accel. Beams **21** (2018) 011001, DOI: [10.1103/PhysRevAccelBeams.21.011001](https://doi.org/10.1103/PhysRevAccelBeams.21.011001).
- [48] Y. Han et al., *Beam-Based Alignment for the Rebaselining of CLIC RTML* (2017) TUPIK099. 4 p, URL: <https://cds.cern.ch/record/2289634>.
- [49] N. Blaskovic Kraljevic, D. Schulte, *Beam-based beamline element alignment for the main linac of the 380 GeV stage of CLIC*, CLIC-Note-1140, 2018, URL: <https://edms.cern.ch/document/2053412/>.
- [50] J. Ogren, *Tuning of the CLIC 380 GeV Final-Focus System with Static Imperfections*, CLIC-Note-1141, 2018, URL: <https://edms.cern.ch/document/2053415/>.

-
- [51] V. M. Juravlev et al., *Investigations of power and spatial correlation characteristics of seismic vibrations in the CERN LEP tunnel for linear collider studies*, tech. rep. CERN-SL-93-53. CLIC-Note-217, CERN, 1993, URL: <https://cds.cern.ch/record/258752>.
- [52] B. Bolzon, *Etude des vibrations et de la stabilisation à l'échelle sous-nanométrique des doublets finaux d'un collisionneur linéaire*, LAPP-T-2007-05, PhD thesis, Université de Savoie, France, 2007, URL: <http://cds.cern.ch/record/1100434>.
- [53] B. Heilig, C. Beggan, J. Lichtenberger, *Natural sources of geomagnetic field variations*, CERN-ACC-2018-0033, CLIC-Note-1083, 2018, URL: <http://cds.cern.ch/record/2643499>.
- [54] F. Bordry et al., *Machine Parameters and Projected Luminosity Performance of Proposed Future Colliders at CERN* (2018), arXiv: 1810.13022 [physics.acc-ph].
- [55] *SLC design handbook. Stanford Linear Collider: design report*, SLAC, Stanford, CA, 1984, URL: <http://cds.cern.ch/record/105035>.
- [56] N. Phinney, *SLC Final Performance and Lessons*, eConf **C00082** (2000) MO102, arXiv: physics/0010008 [physics.acc-ph].
- [57] R. W. Assmann et al., *Accelerator physics highlights in the 1997/98 SLC run*, Conf. Proc. **C9803233** (1998) 474, URL: <https://accelconf.web.cern.ch/accelconf/a98/APAC98/5D034.PDF>.
- [58] M. Aiba et al., *Ultra low vertical emittance at SLS through systematic and random optimization*, Nucl. Instrum. Meth. **A694** (2012) 133, DOI: 10.1016/j.nima.2012.08.012.
- [59] R. Dowd, Y.-R. Tan, K. Wootton, *Vertical Emittance at the Quantum Limit*, Proceedings of IPAC 2014, Dresden, Germany, 2014, TUPRO035, DOI: 10.18429/JACoW-IPAC2014-TUPRO035.
- [60] K. P. Wootton, M. J. Boland, R. P. Rassool, *Measurement of ultralow vertical emittance using a calibrated vertical undulator*, Phys. Rev. ST Accel. Beams **17** (11 2014) 112802, DOI: 10.1103/PhysRevSTAB.17.112802.
- [61] V. Balakin et al., *Focusing of Submicron Beams for TeV-Scale e^+e^- Linear Colliders*, Phys. Rev. Lett. **74** (1995) 2479, DOI: 10.1103/PhysRevLett.74.2479.
- [62] P. C. V. Thrane, *Probing LINEAR Collider Final Focus Systems in SuperKEKB*, CERN-ACC-2017-0052, CLIC-Note-1077, 2017, URL: <https://cds.cern.ch/record/2276026>.
- [63] A. Latina et al., *Experimental demonstration of a global dispersion-free steering correction at the new linac test facility at SLAC*, Phys. Rev. ST Accel. Beams **17** (2014) 042803, DOI: 10.1103/PhysRevSTAB.17.042803.
- [64] A. Latina et al., *Toolbox for Applying Beam-Based Alignment to Linacs*, Proceedings of LINAC 2014, Geneva, Switzerland, THPP034, 2014, URL: <https://cds.cern.ch/record/2062614>.
- [65] H. Zha et al., *Beam-based measurements of long-range transverse wakefields in the Compact Linear Collider main-linac accelerating structure*, Phys. Rev. Accel. Beams **19** (1 2016) 011001, DOI: 10.1103/PhysRevAccelBeams.19.011001.

-
- [66] M. Aicheler et al., eds., *The Compact Linear Collider (CLIC) – Project Implementation Plan*, CERN-2018-010-M, 2018, DOI: [10.23731/CYRM-2018-004](https://doi.org/10.23731/CYRM-2018-004).
- [67] J. Marija et al., *Optimal Power System and Grid Interface Design Considerations for the CLICs Klystron Modulators* (2015) 83, URL: <https://cds.cern.ch/record/1981920>.
- [68] Sprehn, Daryl and others, *A 12 GHz 50 MW klystron for support of accelerator research* (2010) THPEB065, URL: <https://accelconf.web.cern.ch/accelconf/IPAC10/papers/thpeb065.pdf>.
- [69] N. Catalan-Lasheras et al., *Experience Operating an X-band High-Power Test Stand at CERN* (2014), URL: <https://cds.cern.ch/record/1742951>.
- [70] A. Y. Baikov, C. Marrelli, I. Syratchev, *Toward High-Power Klystrons With RF Power Conversion Efficiency on the Order of 90%* (2015), DOI: [10.1109/TED.2015.2464096](https://doi.org/10.1109/TED.2015.2464096).
- [71] N. Catalan Lasheras et al., *High Power Conditioning of X-Band RF Components* (2018) WEPMF074, URL: <https://cds.cern.ch/record/2646747>.
- [72] H. Mainaud Durand, J. Pfingstner, V. Rude, *Micrometric Propagation of Error Using Overlapping Stretched Wires for the CLIC Pre-Alignment* (2017) TUPIK098, URL: <https://cds.cern.ch/record/2289681>.
- [73] *PACMAN Particle Accelerator Components' Metrology and Alignment to the Nanometre scale*, last accessed 14 December 2018, URL: https://web.archive.org/web/*/https://pacman.web.cern.ch.
- [74] D. Caiazza et al., *New solution for the high accuracy alignment of accelerator components*, Phys. Rev. Accel. Beams **20** (2017) 083501, URL: <https://cds.cern.ch/record/2280545>.
- [75] H. Mainaud Durand et al., *The New CLIC Main Linac Installation and Alignment Strategy*, Proceedings of IPAC 2018, Vancouver, BC, Canada, 2018, WEPAF066, DOI: [10.18429/JACoW-IPAC2018-WEPAF066](https://doi.org/10.18429/JACoW-IPAC2018-WEPAF066).
- [76] P. Novotny et al., *What is the best displacement transducer for a seismic sensor?*, Proceedings of INERTIAL 2017, Kauai, Hawaii, USA, 2017, p. 121, DOI: [10.1109/ISS.2017.7935672](https://doi.org/10.1109/ISS.2017.7935672).
- [77] C. Collette et al., *Review: Inertial Sensors for Low-Frequency Seismic Vibration Measurement*, 2012, DOI: [10.1785/0120110223](https://doi.org/10.1785/0120110223).
- [78] S. Hellegouarch et al., *Linear encoder based low frequency inertial sensor*, International Journal of Optomechatronics **10** (2016) 120, DOI: [10.1080/15599612.2016.1217109](https://doi.org/10.1080/15599612.2016.1217109).
- [79] G. Balik et al., *Vibration Control Using a Dedicated Inertial Sensor. Vibration Control Using a Dedicated Inertial Sensor*, IEEE Sensors J. **18** (2018) 428, URL: <https://cds.cern.ch/record/2301234>.
- [80] F. J. Cullinan et al., *Long bunch trains measured using a prototype cavity beam position monitor for the Compact Linear Collider*, Phys. Rev. Spec. Top. Accel. Beams **18** (2015) 112802, URL: <https://cds.cern.ch/record/2135975>.
- [81] A. Dabrowski et al., *Non-destructive Single Shot Bunch Length Measurements for the CLIC Test Facility 3* (2007), URL: <https://cds.cern.ch/record/1058816>.
- [82] G. Berden et al., *Benchmarking of electro-optic monitors for femtosecond electron bunches*, Phys. Rev. Lett. **99** (2007) 164801, DOI: [10.1103/PhysRevLett.99.164801](https://doi.org/10.1103/PhysRevLett.99.164801).

- [83] S. P. Jamison et al.,
Upconversion of a relativistic Coulomb field terahertz pulse to the near infrared,
Appl. Phys. Lett. **96** (2010), DOI: [10.1063/1.3449132](https://doi.org/10.1063/1.3449132).
- [84] P. Karataev et al.,
First Observation of the Point Spread Function of Optical Transition Radiation,
Phys. Rev. Lett. **107** (17 2011) 174801, DOI: [10.1103/PhysRevLett.107.174801](https://doi.org/10.1103/PhysRevLett.107.174801).
- [85] M. Kastriotou et al., *A Versatile Beam Loss Monitoring System for CLIC* (2016) MOPMR024,
URL: <https://cds.cern.ch/record/2207310>.
- [86] E. N. del Busto et al.,
Position resolution of optical fibre-based beam loss monitors using long electron pulses,
Proceedings of IBIC 2015, Melbourne, Australia, WEBLA03, 2015, URL: <http://accelconf.web.cern.ch/accelconf/ibic2015/papers/webla03.pdf>.
- [87] M. Kastriotou et al., *BLM crosstalk studies on the CLIC two-beam module*,
Proceedings of IBIC 2015, Melbourne, Australia, MOPB045, 2015, URL: <http://accelconf.web.cern.ch/accelconf/ibic2015/papers/mopb045.pdf>.
- [88] C. Garion, *Simulations and Vacuum Tests of a CLIC Accelerating Structure* (2011),
URL: <https://cds.cern.ch/record/1407933>.
- [89] C. Garion, A. Lacroix, H. Rambeau,
Development of a new RF finger concept for vacuum beam line interconnections,
Proceedings of IPAC 2012, New Orleans, Louisiana, USA, WEPPD017, 2012, URL: <https://accelconf.web.cern.ch/accelconf/IPAC2012/papers/weppd017.pdf>.
- [90] L. L. Amadora), *Development of copper electroformed vacuum chambers with integrated non-evaporable getter thin film coatings*,
Journal of Vacuum Science & Technology A **36** (2018) 021601, URL: [10.1116/1.4999539](https://doi.org/10.1116/1.4999539).
- [91] F. Niccoli et al., *Beam-pipe coupling in particle accelerators by shape memory alloy rings*,
Mater. Design **114** (2017) 603, DOI: [10.1016/j.matdes.2016.11.101](https://doi.org/10.1016/j.matdes.2016.11.101).
- [92] F. Niccoli et al., *Shape-memory alloy rings as tight couplers between ultrahigh-vacuum pipes: Design and experimental assessment*, J. Vac. Sci. Tech. **A35** (2017) 031601,
DOI: [10.1116/1.4978044](https://doi.org/10.1116/1.4978044).
- [93] B. Shepherd, J. Clarke, N. Collomb,
Permanent magnet quadrupoles for the CLIC Drive Beam decelerator,
CERN-OPEN-2012-018, CLIC-Note-940, 2012,
URL: <https://cds.cern.ch/record/1461571>.
- [94] B. Shepherd,
Radiation damage to permanent magnet materials: A survey of experimental results,
CERN-ACC-2018-0029, CLIC-Note-1079, 2018,
URL: <https://cds.cern.ch/record/2642418>.
- [95] M. A. D. Martinez et al., *Longitudinally Variable Field Dipole Design Using Permanent Magnets For CLIC Damping Rings*,
IEEE Transactions on Applied Superconductivity **28** (2018) 1,
DOI: [10.1109/TASC.2018.2795551](https://doi.org/10.1109/TASC.2018.2795551).
- [96] A. Bernhard et al., *A CLIC Damping Wiggler Prototype at ANKA: Commissioning and Preparations for a Beam Dynamics Experimental Program* (2016) WEPMW002,
URL: <https://cds.cern.ch/record/2207403>.

- [97] C. Belver-Aguilar et al., *Stripline design for the extraction kicker of Compact Linear Collider damping rings*, Phys. Rev. ST Accel. Beams **17** (2014) 071003, DOI: [10.1103/PhysRevSTAB.17.071003](https://doi.org/10.1103/PhysRevSTAB.17.071003).
- [98] C. Belver-Aguilar, M. J. Barnes, *Review of stripline beam impedance: application to the extraction kicker for the CLIC damping rings*, Proceedings of IPAC 2017, Copenhagen, Denmark, vol. 874, 1, 2017, p. 012074, DOI: [10.1088/1742-6596/874/1/012074](https://doi.org/10.1088/1742-6596/874/1/012074).
- [99] M. Pont et al., *The Stripline Kicker Prototype for the CLIC Damping Rings at ALBA: Installation, Commissioning and Beam Characterisation*, Proceedings of IPAC 2018, Vancouver, BC, Canada, 2018, THPMF013, DOI: [10.18429/JACoW-IPAC2018-THPMF013](https://doi.org/10.18429/JACoW-IPAC2018-THPMF013).
- [100] J. Holma, M. Barnes, A. Ferrero Colomo, *Demonstration of Feasibility of the CLIC Damping Ring Extraction Kicker Modulators*, Proceedings of IPAC 2018, Vancouver, BC, Canada, 2018, WEPMF077, DOI: [10.18429/JACoW-IPAC2018-WEPMF077](https://doi.org/10.18429/JACoW-IPAC2018-WEPMF077).
- [101] D. Constable et al., *High Efficiency Klystrons Using the COM Bunching Technique*, Proceedings of IPAC 2017, Copenhagen, Denmark, 2017, MOOCA1, DOI: [10.18429/JACoW-IPAC2017-MOOCA1](https://doi.org/10.18429/JACoW-IPAC2017-MOOCA1).
- [102] P. Chen, *Beamstrahlung and the QED, QCD backgrounds in linear colliders*, Proceedings of PHOTON-PHOTON 1992, San Diego, California, 1992, p. 0418, URL: <https://inspirehep.net/record/338709/files/slac-pub-5914.pdf>.
- [103] E. Brondolin, A. Sailer, *Optimization of timing selections at 380 GeV CLIC*, CLICdp-Note-2018-003, 2018, URL: <https://cds.cern.ch/record/2645355>.
- [104] S. A. E. Langeslag et al., *Characterization of a Large Size Co-Extruded Al-Ni Stabilized Nb-Ti Superconducting Cable for Future Detector Magnets*, IEEE Trans. Appl. Supercond. **23** (2013) 4500504, DOI: [10.1109/TASC.2012.2236597](https://doi.org/10.1109/TASC.2012.2236597).
- [105] I. Shilon et al., *The Influence of the Al Stabilizer Layer Thickness on the Normal Zone Propagation Velocity in High Current Superconductors*, Phys. Procedia **67** (2015) 896, DOI: [10.1016/j.phpro.2015.06.151](https://doi.org/10.1016/j.phpro.2015.06.151).
- [106] M. Villarejo Bermudez, F. Duarte Ramos, H. Gerwig, *Mechanical integration studies for the CLIC vertex and inner tracking detectors*, CLICdp-Note-2015-002, 2015, URL: <https://cds.cern.ch/record/1982810>.
- [107] F. Duarte Ramos, W. Klempt, F.-X. Nuiiry, *Experimental tests on the air cooling of the CLIC vertex detector*, CLICdp-Note-2016-002, 2016, URL: <https://cds.cern.ch/record/2138963>.
- [108] A. M. Nürnberg, D. Dannheim, *Requirements for the CLIC tracker readout*, CLICdp-Note-2017-002, 2017, URL: <https://cds.cern.ch/record/2261066>.
- [109] S. Spannagel et al., *Allpix²: A modular simulation framework for silicon detectors*, Nucl. Instrum. Meth. **A901** (2018) 164, DOI: [10.1016/j.nima.2018.06.020](https://doi.org/10.1016/j.nima.2018.06.020).
- [110] N. Alipour Tehrani et al., *Test beam analysis of ultra-thin hybrid pixel detector assemblies with Timepix readout ASICs*, CLICdp-Note-2016-001, 2016, URL: <https://cds.cern.ch/record/2133128>.

-
- [111] N. Alipour Tehrani, *Test-beam measurements and simulation studies of thin pixel sensors for the CLIC vertex detector*, Diss. ETH No. 24216, CERN-THESIS-2016-311, PhD thesis, ETH Zurich, Switzerland, 2017, URL: <https://cds.cern.ch/record/2270788>.
- [112] N. Alipour Tehrani et al., *Performance evaluation of thin active-edge planar sensors for the CLIC vertex detector*, CLICdp-Pub-2018-005, 2018, URL: <https://cds.cern.ch/record/2649494>.
- [113] F. M. Pitters et al., *Time and Energy Calibration of Timepix3 Assemblies with Thin Silicon Sensors*, CLICdp-Note-2018-008, 2018, URL: <https://cds.cern.ch/record/2649493>.
- [114] S. Spannagel, *Silicon technologies for the CLIC vertex detector*, JINST **12** (2017) C06006, DOI: [10.1088/1748-0221/12/06/C06006](https://doi.org/10.1088/1748-0221/12/06/C06006).
- [115] S. Spannagel, *Technologies for future vertex and tracking detectors at CLIC*, Nucl. Instrum. Meth. (2018), DOI: [10.1016/j.nima.2018.08.103](https://doi.org/10.1016/j.nima.2018.08.103).
- [116] N. Alipour Tehrani et al., *Capacitively coupled hybrid pixel assemblies for the CLIC vertex detector*, Nucl. Instrum. Meth. **A823** (2016) 1, DOI: [10.1016/j.nima.2016.03.072](https://doi.org/10.1016/j.nima.2016.03.072).
- [117] M. D. Buckland, *Simulation and evaluation of HV-CMOS pixel sensors for the CLIC vertex detector*, CERN-THESIS-2018-114, PhD thesis, University of Liverpool, UK, 2018, URL: <https://cds.cern.ch/record/2633983>.
- [118] M. Vicente Barreto Pinto, *Finite-element simulations of coupling capacitances in capacitively coupled pixel detectors*, CLICdp-Note-2017-003, 2017, URL: <https://cds.cern.ch/record/2267848>.
- [119] M. D. Buckland et al., *Tracking performance and simulation of capacitively coupled pixel detectors for the CLIC vertex detector*, CLICdp-Pub-2018-006, 2018, URL: <https://cds.cern.ch/record/2649495>.
- [120] I. Kremastiotis et al., *Design and standalone characterisation of a capacitively coupled HV-CMOS sensor chip for the CLIC vertex detector*, JINST **12** (2017) P09012, DOI: [10.1088/1748-0221/12/09/P09012](https://doi.org/10.1088/1748-0221/12/09/P09012).
- [121] I. Kremastiotis, *Characterisation of capacitively coupled HV/HR-CMOS sensor chips for the CLIC vertex detector*, Proceedings of PSD 2011, Milton Keynes, UK, vol. 12, 12, 2017, p. C12030, DOI: [10.1088/1748-0221/12/12/C12030](https://doi.org/10.1088/1748-0221/12/12/C12030).
- [122] R. M. Munker, *Test beam and simulation studies on High Resistivity CMOS pixel sensors*, CERN-THESIS-2018-202, PhD thesis, University of Bonn, Germany, 2018, URL: <https://cds.cern.ch/record/2644054>.
- [123] M. Munker et al., *Comparison of small collection electrode CMOS pixel sensors with partial and full lateral depletion of the high-resistivity epitaxial layer*, CLICdp-Pub-2018-004, 2018, URL: <https://cds.cern.ch/record/2646292>.
- [124] I. Peric et al., *A high-voltage pixel sensor for the ATLAS upgrade*, Nucl. Instrum. Meth. (2018), DOI: [10.1016/j.nima.2018.06.060](https://doi.org/10.1016/j.nima.2018.06.060).
- [125] R. Bugiel et al., *Test-beam results of a SOI pixel detector prototype*, Nucl. Instrum. Meth. Phys. Res. **A901** (2018) 173, DOI: [10.1016/j.nima.2018.06.017](https://doi.org/10.1016/j.nima.2018.06.017).

-
- [126] I. Kremastiotis, R. Ballabriga, N. Egidios, *Design of a monolithic HR-CMOS sensor chip for the CLIC silicon tracker*, CLICdp-Conf-2018-008, 2018, URL: <https://cds.cern.ch/record/2643766>.
- [127] A. Velyka, H. Jansen, *Enhanced Lateral Drift Sensors: Concept and Development*, Proceedings of TIPP 2017, Beijing, China, 2018, p. 380, DOI: 10.1007/978-981-13-1316-5_71.
- [128] T. Tick, M. Campbell, *TSV processing of Medipix3 wafers by CEA-LETI: A progress report*, Proceedings of TWEPP 2011, Vienna, Austria, vol. 6, 2011, p. C11018, DOI: 10.1088/1748-0221/6/11/C11018.
- [129] M. Campbell et al., *Towards a new generation of pixel detector readout chips*, JINST **11** (2016) C01007, DOI: 10.1088/1748-0221/11/01/C01007.
- [130] G. Blanchot, D. Dannheim, C. Fuentes, *Power-pulsing schemes for vertex detectors at CLIC*, JINST **9** (2014) C01005, DOI: 10.1088/1748-0221/9/01/C01005.
- [131] G. Blanchot, C. A. Fuentes Rojas, *Power pulsing scheme for analog and digital electronics of the vertex detectors at CLIC*, CLICdp-Note-2015-004, 2015, URL: <https://cds.cern.ch/record/2062429>.
- [132] S. Green, *Calorimetry at a Future Linear Collider*, CERN-THESIS-2017-237, PhD thesis, University of Cambridge, UK, 2017, URL: <http://cds.cern.ch/record/2293158>.
- [133] J. Repond et al., *Design and electronics commissioning of the physics prototype of a Si-W electromagnetic calorimeter for the International Linear Collider*, JINST **3** (2008) P08001, DOI: 10.1088/1748-0221/3/08/P08001.
- [134] C. Adloff et al., *Construction and commissioning of the CALICE analog hadron calorimeter prototype*, JINST **5** (2010) P05004, DOI: 10.1088/1748-0221/5/05/P05004.
- [135] F. Sefkow et al., *Experimental tests of particle flow calorimetry*, Rev. Mod. Phys. **88** (2016) 015003, DOI: 10.1103/RevModPhys.88.015003.
- [136] C. Adloff et al., CALICE Collaboration, *Response of the CALICE Si-W electromagnetic calorimeter physics prototype to electrons*, Nucl. Instrum. Meth. **A608** (2009) 372, DOI: 10.1016/j.nima.2009.07.026.
- [137] C. Adloff et al., *Hadronic energy resolution of a highly granular scintillator-steel hadron calorimeter using software compensation techniques*, JINST **7** (2012) P09017, DOI: 10.1088/1748-0221/7/09/P09017.
- [138] F. Sefkow, F. Simon, *A highly granular SiPM-on-tile calorimeter prototype*, Proceedings for CALOR 2018, Eugene, Oregon, USA, 2018, arXiv: 1808.09281 [physics.ins-det].
- [139] H. Abramowicz et al., *Performance of fully instrumented detector planes of the forward calorimeter of a Linear Collider detector*, JINST **10** (2015) P05009, DOI: 10.1088/1748-0221/10/05/P05009.
- [140] H. Abramowicz et al., *Measurement of shower development and its Molière radius with a four-plane LumiCal test set-up*, Eur. Phys. J. C **78** (2018) 135, DOI: 10.1140/epjc/s10052-018-5611-9.
- [141] M. Raymond et al., *The APV25 0.25 /spl mu/m CMOS readout chip for the CMS tracker*, Proceedings for IEEE NSS 2000 (Cat. No.00CH37149), vol. 2, 2000, DOI: 10.1109/NSSMIC.2000.949881.

- [142] M. J. French et al., *Design and results from the APV25, a deep sub-micron CMOS front-end chip for the CMS tracker*, Proceedings of HSTD 2000, Hiroshima, Japan, vol. A466, 2001, p. 359, DOI: [10.1016/S0168-9002\(01\)00589-7](https://doi.org/10.1016/S0168-9002(01)00589-7).
- [143] V. Ghenescu,
Molière radius measurement using a compact prototype of LumiCal in a test set-up, Proceedings of ICHEP 2018, Seoul, Korea, 2018, arXiv: [1811.11432](https://arxiv.org/abs/1811.11432) [physics.ins-det].
- [144] M. Frank et al.,
DDG4 A Simulation Framework based on the DD4hep Detector Description Toolkit, Proceedings of CHEP 2015, Okinawa, Japan, vol. 664, 7, 2015, p. 072017, DOI: [10.1088/1742-6596/664/7/072017](https://doi.org/10.1088/1742-6596/664/7/072017).
- [145] S. Agostinelli et al., Geant4 Collaboration, *Geant4 – A Simulation Toolkit*, Nucl. Instrum. Meth. **A506** (2003) 250, DOI: [10.1016/S0168-9002\(03\)01368-8](https://doi.org/10.1016/S0168-9002(03)01368-8).
- [146] J. Allison et al., *Geant4 developments and applications*, IEEE T. Nucl. Sci. **53** (2006) 270, DOI: [10.1109/TNS.2006.869826](https://doi.org/10.1109/TNS.2006.869826).
- [147] J. Allison et al., *Recent developments in Geant4*, Nucl. Instrum. Meth. **A835** (2016) 186, DOI: [10.1016/j.nima.2016.06.125](https://doi.org/10.1016/j.nima.2016.06.125).
- [148] A. Sailer et al., *DD4Hep Based Event Reconstruction*, J. Phys. Conf. Ser. **898** (2017) 042017, DOI: [10.1088/1742-6596/898/4/042017](https://doi.org/10.1088/1742-6596/898/4/042017).
- [149] P. Schade, A. Lucaci-Timoce, *Description of the signal and background event mixing as implemented in the Marlin processor OverlayTiming*, LCD-Note-2011-006, 2011, URL: <http://cds.cern.ch/record/1443537>.
- [150] E. Leogrande, *Conformal tracking for the CLIC detector*, CLICdp-Conf-2018-004, 2018, URL: <https://cds.cern.ch/record/2630512>.
- [151] C. Grefe et al., *ILCDIRAC, a DIRAC extension for the Linear Collider community*, J. Phys. Conf. Ser. **513** (2013), CLICdp-Conf-2013-003 032077, DOI: [10.1088/1742-6596/513/3/032077](https://doi.org/10.1088/1742-6596/513/3/032077).
- [152] H. Tran et al., *Software compensation in particle flow reconstruction*, Eur. Phys. J. **C77** (2017) 698, DOI: [10.1140/epjc/s10052-017-5298-3](https://doi.org/10.1140/epjc/s10052-017-5298-3).
- [153] M. Boronat et al., *Jet reconstruction at high-energy electron-positron colliders*, Eur. Phys. J. **C78** (2018) 144, DOI: [10.1140/epjc/s10052-018-5594-6](https://doi.org/10.1140/epjc/s10052-018-5594-6).
- [154] N. Phinney, N. Toge, N. J. Walker, eds., *ILC Reference Design Report Volume 3 - Accelerator*, 2007, arXiv: [0712.2361](https://arxiv.org/abs/0712.2361) [physics.acc-ph].
- [155] C. Adolphsen et al., *The International Linear Collider Technical Design Report - Volume 3.II: Accelerator Baseline Design*, 2013, arXiv: [1306.6328](https://arxiv.org/abs/1306.6328) [physics.acc-ph].
- [156] P. Lebrun, P. Garbincius, *Assessing Risk in Costing High-energy Accelerators: from Existing Projects to the Future Linear Collider*, Proceedings of IPAC 2010, Kyoto, Japan, CLIC-Note-825, 2011, URL: <https://cds.cern.ch/record/1341567>.
- [157] D. Dannheim et al., *Cost estimate for CLICdet*, LCD-Note-2018-005, 2018, URL: <https://edms.cern.ch/document/2027873/>.
- [158] L. Evans, S. Michizono, *The International Linear Collider Machine Staging Report 2017* (2017), arXiv: [1711.00568](https://arxiv.org/abs/1711.00568) [physics.acc-ph].
- [159] J. Ellis et al., *Dimension-6 operator analysis of the CLIC sensitivity to new physics*, JHEP **05** (2017) 096, DOI: [10.1007/JHEP05\(2017\)096](https://doi.org/10.1007/JHEP05(2017)096).

-
- [160] *AWAKE Advanced Wakefield Experiment*, last accessed 14 December 2018,
URL: https://web.archive.org/web/*/https://awake.web.cern.ch/.
- [161] D. Schulte, F. Zimmermann, *The crossing angle in CLIC*,
Proceedings of PAC 2001, Chicago, USA, vol. C0106181, 2001, p. 148,
DOI: [10.1109/PAC.2001.987455](https://doi.org/10.1109/PAC.2001.987455).
- [162] B. Cros, P. Muggli, eds., *Towards a Proposal for an Advanced Linear Collider; Report on the Advanced and Novel Accelerators for High Energy Physics Roadmap Workshop*, 2017,
URL: <https://cds.cern.ch/record/2298632>.
- [163] R. J. England et al., *Dielectric laser accelerators*, *Reviews of Modern Physics* **86** (2014) 1337,
DOI: [10.1103/RevModPhys.86.1337](https://doi.org/10.1103/RevModPhys.86.1337).
- [164] I. Blumenfeld et al.,
Energy doubling of 42 GeV electrons in a metre-scale plasma wakefield accelerator,
Nature **445** (2007) 741, DOI: [10.1038/nature05538](https://doi.org/10.1038/nature05538).
- [165] M. Litos et al.,
High-efficiency acceleration of an electron beam in a plasma wakefield accelerator,
Nature **515** (2014) 92, DOI: [10.1038/nature13882](https://doi.org/10.1038/nature13882).
- [166] E. Adli et al.,
A Beam Driven Plasma-Wakefield Linear Collider: From Higgs Factory to Multi-TeV, 2013,
arXiv: [1308.1145](https://arxiv.org/abs/1308.1145) [[physics.acc-ph](https://arxiv.org/archive/physics)].
- [167] D. Schulte, *Requirements for future linear colliders*, 2017,
URL: <https://indico.cern.ch/event/607729/>.
- [168] W. P. Leemans et al., *Multi-GeV Electron Beams from Capillary-Discharge-Guided Subpetawatt Laser Pulses in the Self-Trapping Regime*, *Phys. Rev. Lett.* **113** (24 2014) 245002,
DOI: [10.1103/PhysRevLett.113.245002](https://doi.org/10.1103/PhysRevLett.113.245002).
- [169] V. I. Telnov, *Crossing angle at the photon collider*,
Proceedings of LCWS 2005, Stanford, California, USA, vol. C050318, 2005, p. 1113,
arXiv: [physics/0507134](https://arxiv.org/abs/physics/0507134) [[physics](https://arxiv.org/archive/physics)].
- [170] D. Schulte, *Application of Advanced Accelerator Concepts for Colliders*,
Rev. Accel. Sci. Tech. **09** (2016) 209, DOI: [10.1142/s1793626816300103](https://doi.org/10.1142/s1793626816300103).
- [171] S. Janssens et al., *Stabilisation and precision pointing quadrupole magnets in the Compact Linear Collider (CLIC)*, CERN-THESIS-2015-004,
PhD thesis, University of Amsterdam, The Netherlands, 2015,
URL: <https://cds.cern.ch/record/1985255>.
- [172] G. Balik et al., *Vibration Control Using a Dedicated Inertial Sensor*,
IEEE Sensors Journal **18** (2018) 428, DOI: [10.1109/JSEN.2017.2768127](https://doi.org/10.1109/JSEN.2017.2768127).
- [173] J. Pfungstner, E. Adli, D. Schulte,
On-line dispersion estimation and correction scheme for the Compact Linear Collider,
Phys. Rev. Accel. Beams **20** (2017) 011006,
DOI: [10.1103/PhysRevAccelBeams.20.011006](https://doi.org/10.1103/PhysRevAccelBeams.20.011006).
- [174] M. Diomede et al., *RF Design of the X-band Linac for the EuPRAXIA@SPARC_LAB Project*,
Proceedings of IPAC 2018, Vancouver, BC, Canada, 2018, p. 4422,
DOI: [10.18429/JACoW-IPAC2018-THPMK058](https://doi.org/10.18429/JACoW-IPAC2018-THPMK058).

- [175] P. Williams et al.,
Developments in the CLARA FEL Test Facility Accelerator Design and Simulations,
Proceedings of FEL 2014, Basel, Switzerland, TUP091, 2014, p. 589, URL: <http://accelconf.web.cern.ch/AccelConf/FEL2014/papers/tup091.pdf>.
- [176] *CompactLight project*, last accessed 14 December 2018,
URL: https://web.archive.org/web/*/http://www.compactlight.eu/.
- [177] *Smart*Light: a Dutch table-top synchrotron light source*, last accessed 14 December 2018,
URL: <https://www.knaw.nl/shared/resources/adviezen/EervolKNAWAgendaSmartLight.pdf>.
- [178] T. Akesson et al., *Dark Sector Physics with a Primary Electron Beam Facility at CERN*,
CERN-SPSC-2018-023, SPSC-EOI-018, 2018,
URL: <http://cds.cern.ch/record/2640784>.